Measurement of proton-proton bremsstrahlung at 389MeV

Keisuke Yasuda

A dissertation submitted in partial fulfillment of

the requirements for the degree of

Doctor of Science

Department of Physics

Kyoto University

April, 1999

Abstract

Differential cross sections and analyzing powers for the proton-proton bremsstrahlung have been measured at 389 MeV incident energy. A two-arm magnetic spectrometer and a liquid hydrogen target have made it possible to measure the proton-proton bremsstrahlung with small background. The two outgoing protons were detected both at scattering angles of 26.0°. The present data are the first results in the kinematical region where the Δ contribution is expected to be significant. The error in the absolute normalization for the cross section is about 6%. The cross section data of *pp* elastic scattering obtained with the same apparatus agree well with a phase shift calculation, *SAID*.

At around $\theta_\gamma = 70°$ where the contribution from the Δ current is predicted to be large, the present cross section data are larger than the theoretical predictions including the Δ current contribution. The present data are consistent with the theoretical calculations at the backward photon emission angle where the effect of the Δ current is predicted to be small. In the analyzing power data, there are differences between the data and the theoretical calculations at around $\theta_\gamma = 70°$ where there are discrepancies between the cross section data and the theoretical predictions. The discrepancies can not be explained by the reaction mechanisms which have been taken into account so far.

Contents

List of Tables

List of Figures

Chapter 1

Introduction

Proton-proton bremsstrahlung ($pp\gamma$) is one of the most fundamental inelastic NN scattering reactions. In this process only two particles in the final state are strongly interacting and a photon comes from the well understood electromagnetic process. Therefore we can study the hadronic process with less ambiguity than other inelastic NN scatterings, for example, the pion production, which includes three strongly interacting particles in the final state. Moreover, the $pp\gamma$ process has the advantage that the leading-order dipole radiation is suppressed because both protons have the same charge. This leading-order term can be calculated by the classical electromagnetic theory and it is not interesting for our point of view. Due to this suppression, higher-order radiation, which includes information about the hadronic processes, plays an important role in the $pp\gamma$ process. On the other hand, in the proton-neutron bremsstrahlung ($pn\gamma$) process the leading-order dipole radiation dominates. Details for the classical calculations of the $pp\gamma$ and $pn\gamma$ are presented in Appendix C.

The $pp\gamma$ process has been investigated to study the off-shell behavior of the NN interaction. Nucleons violating Eq. (1.1) are called off-shell, whereas nucleons satisfying Eq. (1.1) are on-shell,

$$E^2 = M^2 + p^2 \tag{1.1}$$

where E and p are the energy and momentum of the nucleon and M is the nucleon mass. Most of modern potential model calculations for the NN interaction succeeded to reproduce the experimental data of the NN elastic scattering even if the fundamental processes taken into account in the each model were not same [1, 2, 3, 4], because the parameters used in these models were determined by fitting the NN elas-

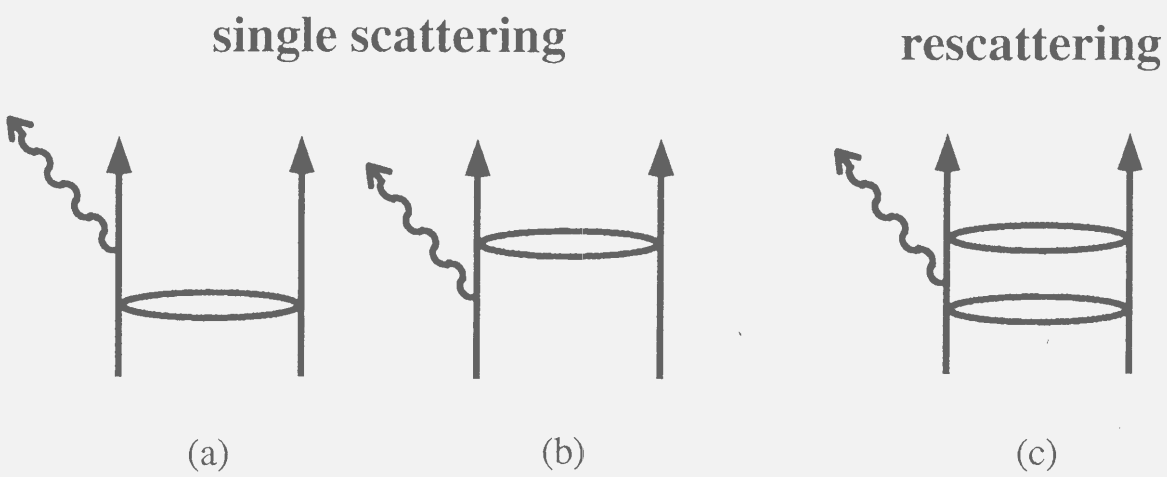

Figure 1.1: The diagrams for the $pp\gamma$ reaction corresponding to the single scattering ((a) and (b)) and the rescattering ((c)).

tic scattering data. Measuring the off-shell behavior of the NN interaction is one of the methods to discriminate between the potential models.

As an experimental aspect, the cross section of the $pp\gamma$ reaction is small (a few μb/sr/sr/rad) and there are large background sources such as the pp elastic scattering, the proton-nucleus inelastic scattering, and the $pp\pi^0$ reaction. In the energy region above the π^0 production threshold, the $pp\pi^0$ reaction cause the large background. In the experiments which have been performed so far, most of the measurements were performed at the incident energy below or around the π^0 production threshold in order to reduce the background due to the $pp\pi^0$ reaction.

In 1970's, several measurements for the $pp\gamma$ reaction were performed. The cross section data were taken mostly in the low energy region ($T_p \leq 200$ MeV) [5, 6, 7, 8, 9, 10, 11]. The data were compared with the theoretical calculations with and without the off-shell effect. In these calculations, only single scattering diagram (Fig. 1.1(a),(b)) are included. The data are well reproduced with a soft photon approximation (SPA) calculation which includes only the on-shell nucleonic current. The data at $T_p = 200$MeV are shown in Fig. 1.2.

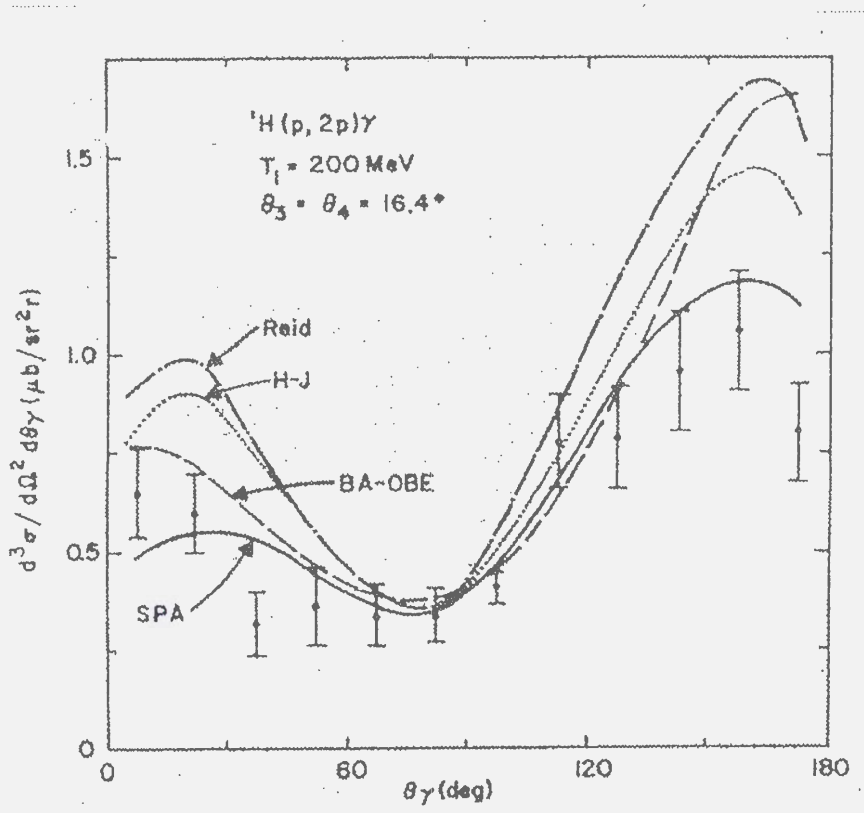

Figure 1.2: The $pp\gamma$ cross section data at $T_p = 200$MeV [11]. The lines are the results of the calculations with the soft-photon approximation (solid), Hamada-Johnston potential (dotted), one-boson-exchange potential (dashed), and Reid soft core potential (dash-dotted).

In the early 1990's, the TRIUMF group measured the $pp\gamma$ reaction at the incident energy of $T_p = 280$ MeV [12], which is slightly below the π^0 production threshold (287 MeV). The cross sections and analyzing powers were measured systematically in a wide range of kinematical conditions. The data were compared with the potential model calculations with Paris and Bonn potentials and the SPA calculation. It was claimed that a sizable contribution of the off-shell effect has been observed in the analyzing powers (Fig. 1.3). In the cross section data, however, there is large discrepancy between the data and theoretical calculations, and an arbitrary normalization factor of 2/3 was applied to the data. This normalization factor was determined by fitting the data to the theoretical calculations and the reason why the normalization factor was needed could not be found. The potential model calculations used for the analysis of the TRIUMF data can not reproduce the cross section data even though it agrees with the analyzing power data, and we can not, therefore, conclude that the off-shell effect was observed by the TRIUMF data. As discussed later, this large discrepancy turned out due to lack of the rescattering diagrams in the theoretical calculation.

As a result, the interest in the $pp\gamma$ process was renewed and several experiments were performed around the pion production threshold energy region at IUCF ($T_p =$ 294 MeV) [13], COSY ($T_p = 293$ MeV) [14], TSL ($T_p = 287, 310$ MeV) [15, 16], and KVI ($T_p = 190$ MeV) [18]. The data of the IUCF measurement were a by-product of the $pp \to pp\pi^0$ ($pp\pi^0$) experiment close to threshold [17]. The detector setup was tuned for the $pp\pi^0$ experiment and the kinematical region was extremely limited. It is therefore difficult to compare the IUCF data with the TRIUMF data or the theoretical calculations. In the measurements at COSY and TSL, the cross sections were measured at almost the same kinematical region as the TRIUMF measurement. The TSL data agreed with the TRIUMF data without the normalization factor 2/3. In the KVI measurement, the cross sections and analyzing powers were measured at relatively low incident energy.

In order to explain the discrepancy, precise theoretical investigation of the $pp\gamma$ process have been made. Herrmann *et al.* and Brown *et al.* investigated the contribution of the rescattering of the two protons (Fig. 1.1). They showed that the contribution of the rescattering enhances the cross section especially at the forward

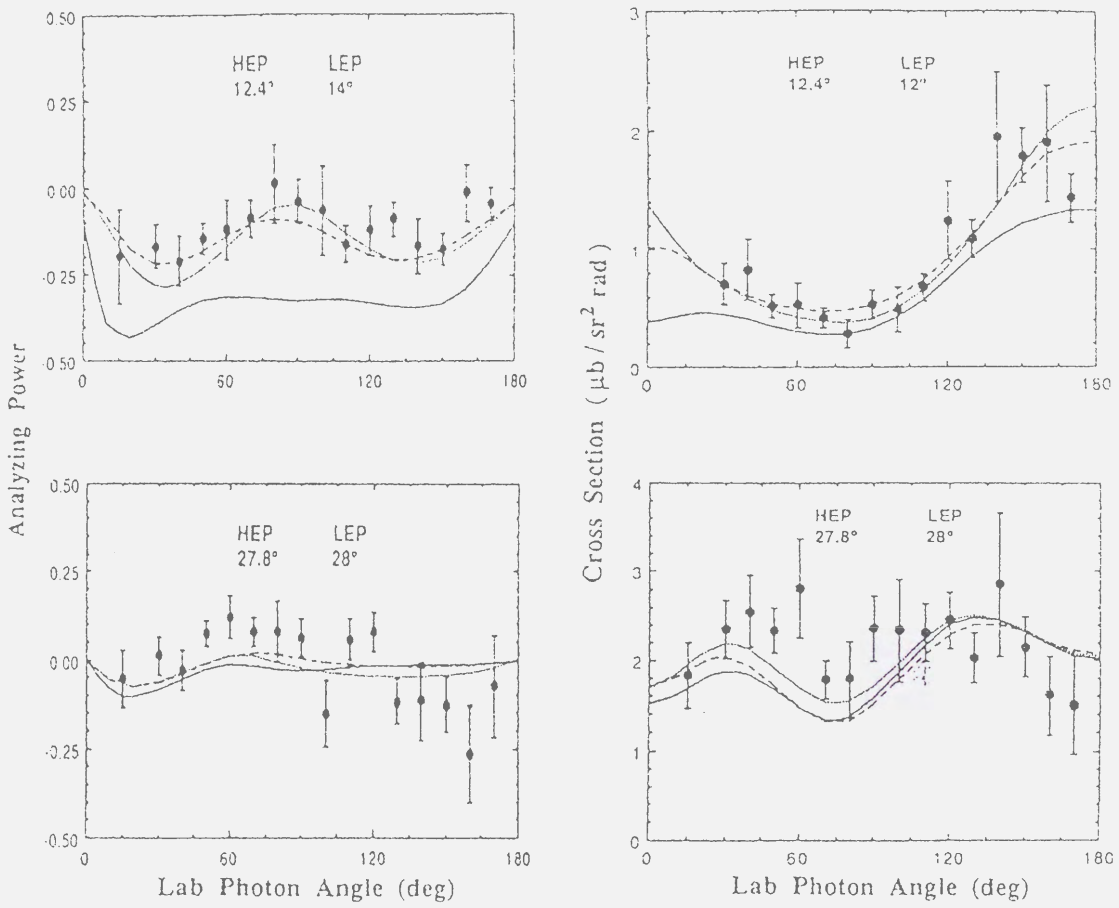

Figure 1.3: The results of the TRIUMF measurement. The values of the HEP and LEP show the proton angles. The cross section data include the normalization factor 2/3. The lines are the results of the calculations with the soft-photon approximation (solid), Paris potential (dotted), and Bonn potential (dashed).

proton angle [25, 26]. The discrepancy between the data and their calculations became rather small with the rescattering diagram. In the theoretical calculation based on a potential model, the emission of the photon is accounted by including a non-relativistic reduction of the nucleon-nucleon-photon vertex. In such a reduction, the leading-order term, which arises from the large component of the Dirac spinors, is taken into account. Herrmann and Nakayama calculated the effect of so-called "relativistic corrections", which come from the small component of the Dirac spinors, and showed that the inclusion of the corrections tends to suppress the cross section [25].

In the intermediate energy region, in addition to the nucleonic current the influence of more elaborate mechanisms including the mesonic and non-nucleonic (Δ, $\bar{N}$) degrees of freedom play an important role. A number of theorists calculated the cross sections and the spin observables of the $pp\gamma$ reaction including the $\omega\pi\gamma$ and $\rho\pi\gamma$ decay graphs, negative energy states (pair currents) and the Δ currents [19, 20, 21, 22, 23, 24]. The diagrams of these mechanisms are shown in Fig. 1.4. Some of these calculations predict that the Δ current contribution may enhance the cross section even at around 400 MeV incident proton energy, which is far below the Δ resonance region [20, 22, 24]. The contribution of the Δ current to the differential cross section is predicted to be large at the proton angles $\theta_1 = \theta_2 \sim 20°$ and $\theta_\gamma \sim 70°$ and enhances the cross sections about 100% [20, 22, 24]. The main contribution from the meson exchange currents is due to the $\omega\pi\gamma$ graph. Its effect in the cross section is predicted to be typically $8 - 20\%$ of that of the Δ current at $T_p = 280$ MeV and the same order at $T_p = 400$ MeV [24]. The influence of the negative energy states is predicted to be small due to a large cancellation among the single scattering and rescattering [21, 23]. The effect is found at the higher photon energy (small proton angles), and enhances the cross section about 20% at $T_p = 280$ MeV. In Fig. 1.5, the theoretical calculations including the effect of the Δ current are presented with the TRIUMF data ($T_p = 280$ MeV) [20]. The calculations reproduced the experimental data without the normalization factor, 2/3.

In the framework of the SPA calculation, only the single scattering diagrams of the nucleonic current are included. It is difficult to determine the off-shell effect by comparison between the potential model calculation and the SPA calculation. Recently, Fearing showed that the off-shell effect is not measurable in the π^+-π^0 bremsstrahlung

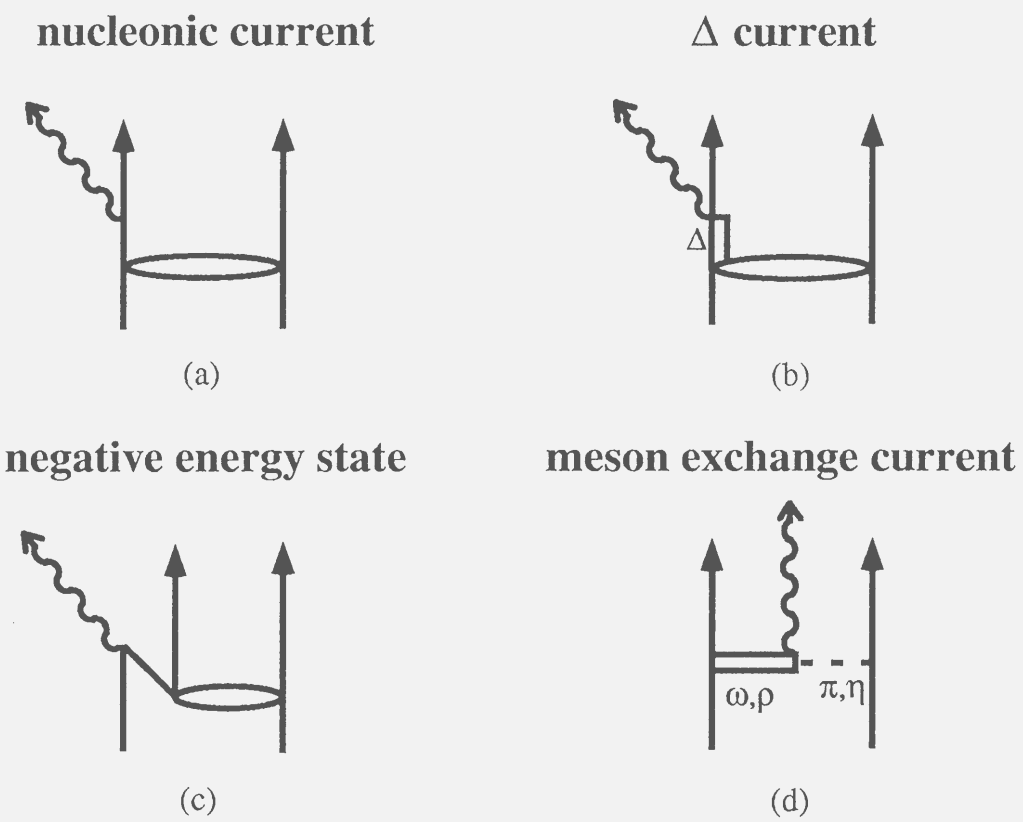

Figure 1.4: The diagrams for the $pp\gamma$ reaction: the nucleonic current (a), the Δ current (b), the negative energy state (c), and the meson exchange current (d).

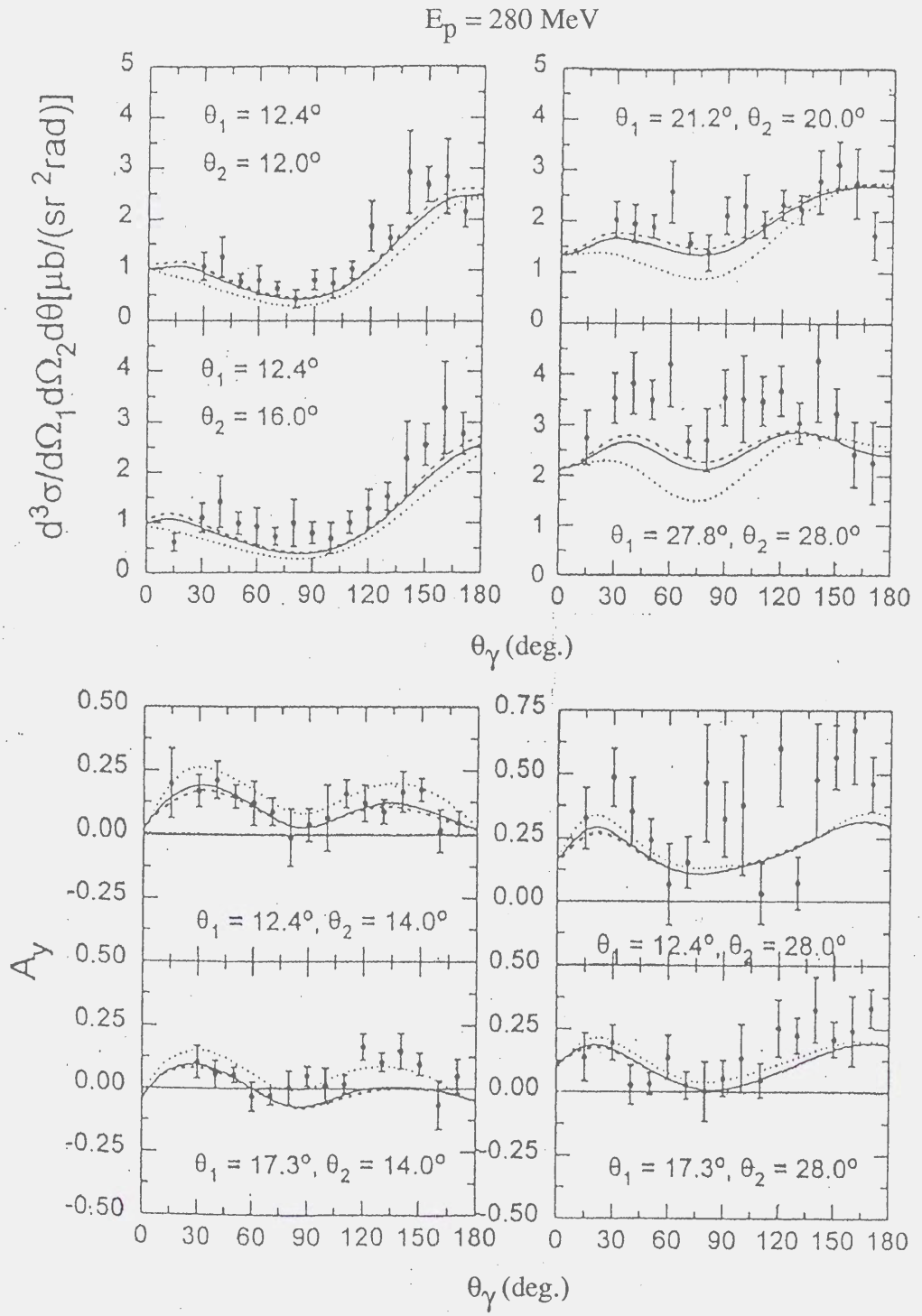

Figure 1.5: The theoretical calculations for the $pp\gamma$ reaction with the TRIUMF data. The solid and dashed lines are the results including the nucleonic and Δ currents, and the dotted lines are including only nucleonic current. This is taken from Ref. [20].

case [28]. Although he insisted that the off-shell amplitudes are unmeasurable in $NN\gamma$, there is a contrary claim that the contribution from the off-shell amplitude can be measured in the radiation from the magnetic current, which is not taken into account in the π^+-π^0 bremsstrahlung case [29, 30]. In any case, the information that can be obtained in determining the off-shell effect is less clear than previously thought.

The theoretical predictions of the cross sections and analyzing powers calculated by Nakayama at the incident energy of 392 MeV are shown in Fig. 1.6. The solid lines show the results of the calculation including the Δ current and the dashed line show the results without the Δ current [31, 20]. The proton angles are both 26.0 degree in the laboratory system. These calculations predict that the Δ current enhances the cross sections about 100% at $\theta_\gamma \sim 70°$ in this kinematical condition. The effects of the meson exchange currents and the negative energy states are predicted to be smaller than that of the Δ currents.

In order to confirm the existence of the Δ contribution to the $pp\gamma$ process, the experiments above the π^0 production threshold are desired. In the TRIUMF, IUCF and COSY experiments, incident energies were not high enough to investigate the effect of the Δ current. In the TRIUMF and IUCF experiments, they aimed mainly at the off-shell effects of the NN interaction and measured both protons at small angle. Therefore their setups were not suitable for investigating the Δ current contribution to the $pp\gamma$ process. In the energy region above the π^0 meson production threshold (and in the nucleon resonance region), a pioneering measurement has been performed at $T_p = 730$ MeV with the LBL 184-inch cyclotron [32]. In the LBL experiment, only the $pp\gamma$ events with relatively low photon energy were measured in order to eliminate the $pp\pi^0$ events, and the kinematical region where the Δ effect is significant was not covered.

In this thesis, the experimental study for the $pp\gamma$ reaction at $T_p = 389$ MeV is presented. The experiment was performed at the Research Center for Nuclear Physics (RCNP), Osaka University using a polarized proton beam. The measurement was performed at the kinematical condition where the contribution of the Δ current is expected to be large. A liquid hydrogen target was used in order to reduce the background from the nuclei except for hydrogen in the target. A two-arm magnetic spectrometer system was used to detect the outgoing two protons. The momentum

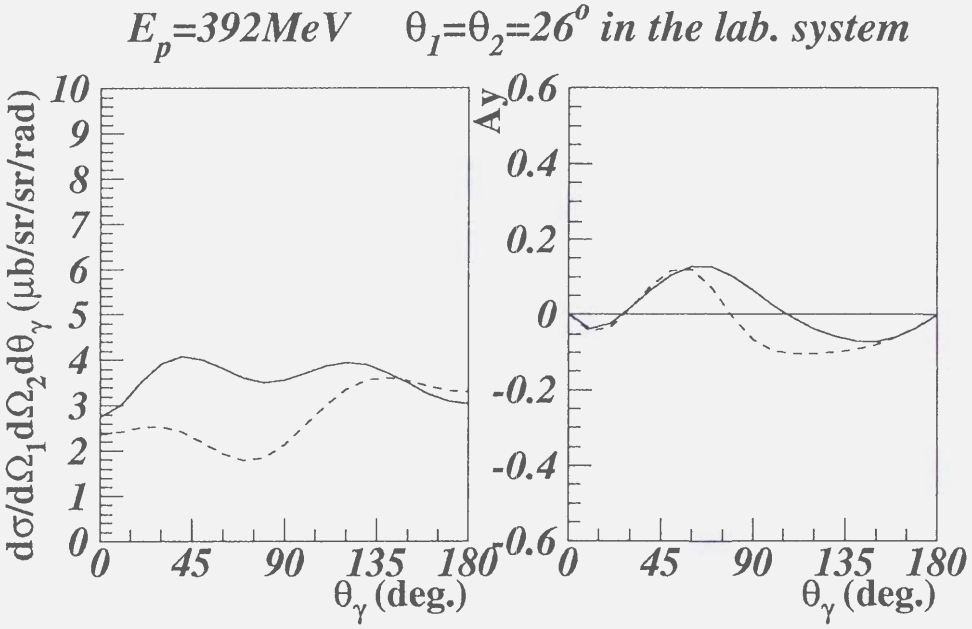

Figure 1.6: The theoretical calculation of the cross section (left) and analyzing power (right). The solid lines show the result of the calculations including the Δ current and dashed lines are the results without Δ current.

resolution of the spectrometer system is good enough to discriminate between the $pp\gamma$ events and $pp\pi^0$ events.

The experimental apparatus is described in Chapter 2. Chapter 3 presents the procedure of the data analysis. The experimental results are presented in Chapter 4 and their physical interpretations are discussed in Chapter 5. A summary is given in Chapter 6.

Chapter 2

Experiment

2.1 Overview

The experiment was performed at the Research Center for Nuclear Physics (RCNP), Osaka University. Figure 2.1 shows an overview of the RCNP facility. A polarized proton beam from the ion source was injected into the AVF cyclotron and accelerated up to 64.2 MeV. The proton beam was accelerated up to 392 MeV by the RING cyclotron. It was extracted to the West Experimental Hall and incident on a liquid hydrogen target. The two outgoing protons were detected with a two-arm spectrometer system. The four-momentum of the third outgoing particle is calculated with measured momentum vectors of two protons. The invariant mass of the particle is calculated from the four momentum. Luminosity was measured with a luminosity monitor, which counted the elastically scattered protons from the liquid hydrogen target.

In the following sections, details of the experiment are described.

2.2 Polarimeter

The beam polarization and beam intensity were measured with two sets of beam line polarimeters (BLP's). These are placed in the beam line of the WN course ; One is placed at straight beam line to the scattering chamber (called "WN") and the other is placed between the RING cyclotron and the West Experimental Hall (called "Cave") as shown in Fig. 2.1. Both polarimeters consist of 4 sets of pair plastic scintillators,

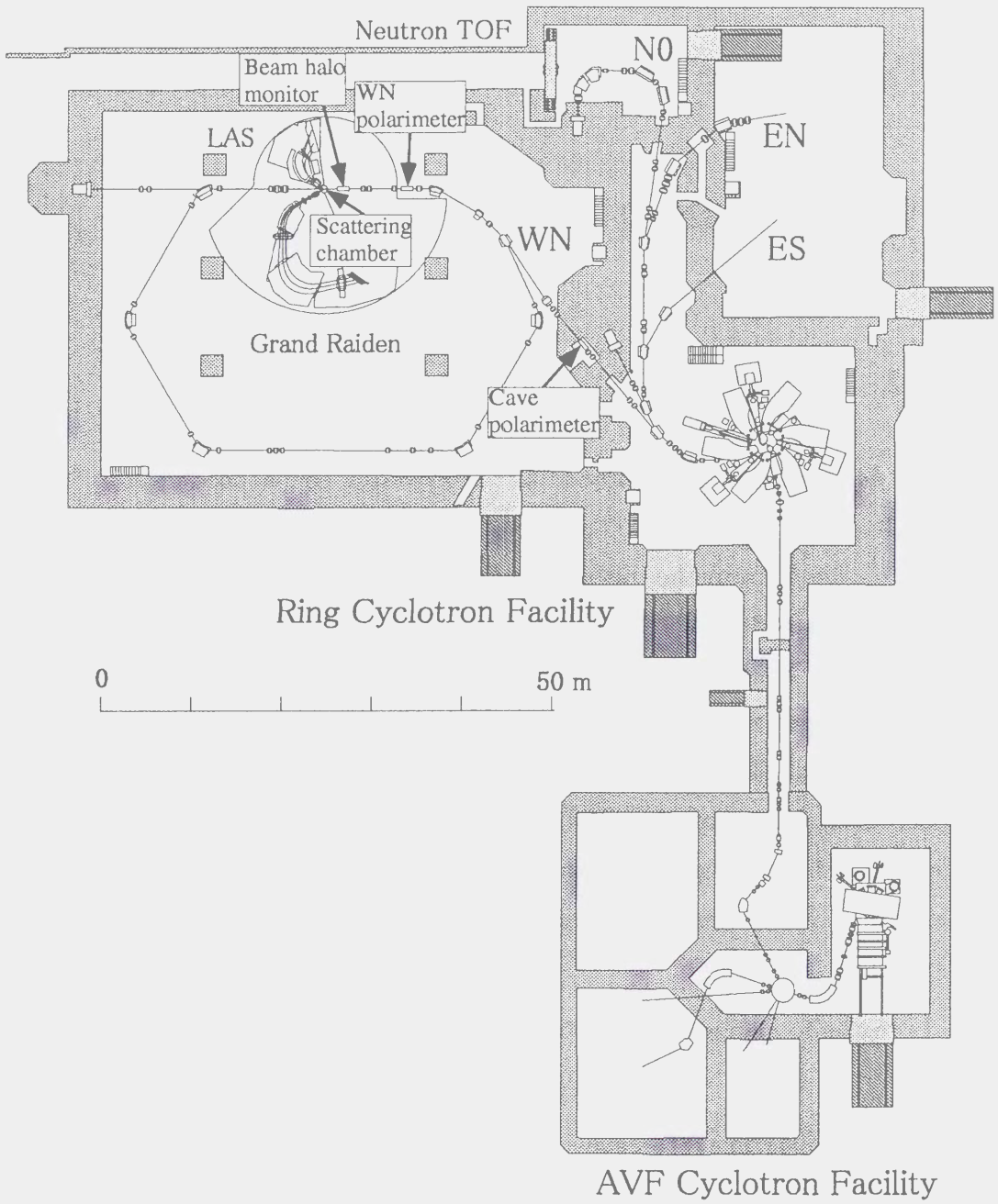

Figure 2.1: Overview of the RCNP facility

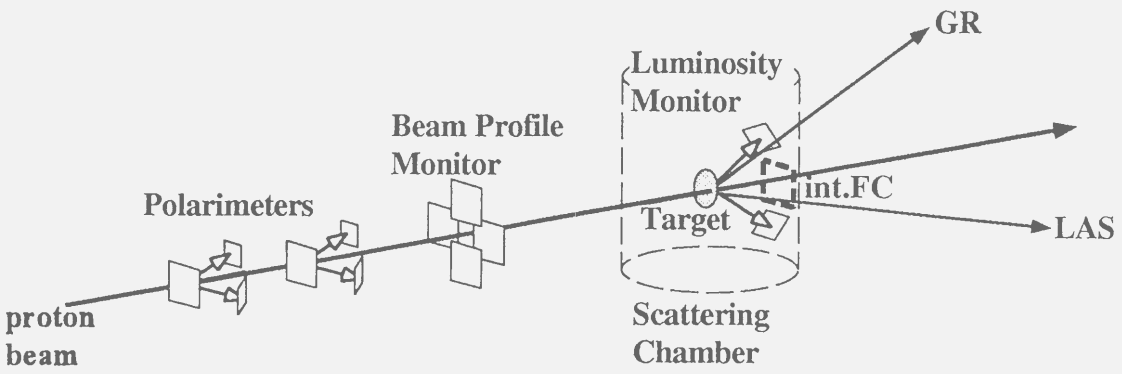

Figure 2.2: Schematic view of the beam line.

which was set at $\theta_1 = 17.0°$ and $\theta_2 = 69.7°$, to detect the scattered protons to the left, right, up and down side respectively. Four pairs of plastic scintillators measures the scattered and recoil protons from the *pp* elastic scattering from a target foil.

The "WN" polarimeter was used for the measurement of the beam polarization with a CH_2 target of 30 μm thickness because the effective analyzing power of CH_2 is known ($A_y = 0.45 \pm 0.01$ at $E_p = 392$ MeV, $\theta_1 = 17°$) [35]. The beam polarization was deduced from the left-right asymmetry of the proton-proton elastic scattering events.

The "Cave" polarimeter was used for the measurement of the beam intensity. An aramide foil was used for the target because hydrogen molecules in the aramide foil are hard to vaporize and therefore it is expected that the target thickness is almost constant during the experiment. Thickness of the aramide foil is 4 μm. The absolute value of the beam intensity was calibrated with the Faraday cup set in the scattering chamber. The Faraday cup causes large background and it was used only for the calibration. The calibration run was performed several times during the experiment.

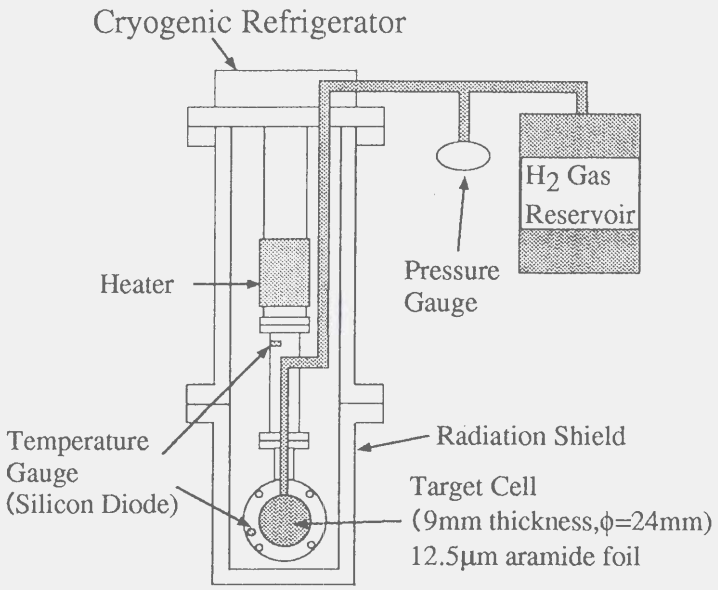

Figure 2.3: Liquid hydrogen target system.

2.3 Liquid hydrogen target

Reduction of huge background events from proton-nucleus inelastic scattering events is indispensable to observe the $pp\gamma$ process. Therefore, we used a liquid hydrogen target system (Fig. 2.3) developed by the Kyushu university group [36], to reduce the backgrounds. The diameter of the target was 24 mm. The target thickness was about 9 mm and the container windows were made of 12.5 μm thick aramide foils. A cryogenic refrigerator (Daikin V204SC6L) liquefied the target hydrogen from the room temperature. The target cell was connected to the hydrogen gas reservoir of 5 litters in volume and the hydrogen gas system was isolated from the outside. The gas pressure in this system was 1.7 atm for the gas target case and 1.0 atm for the liquid target case.

The amount of materials other than hydrogen could be significantly reduced by using the liquid hydrogen target. However, background caused by the proton inelastic scattering from the aramide foils was not negligibly small. Therefore, the contribution

of the target foils had to be subtracted from the measured events. The contribution of the target foils was measured by a "empty target" run, which was performed with a hydrogen gas target. Due to the low temperature of the liquid hydrogen target, the residual gas in the scattering chamber was frozen on the target foils and this also caused background. In order to estimate the contribution from the frozen gas correctly, the temperature at the "empty target" run must be kept in low temperature between 22 and 27 K, where nitrogen and oxygen molecules are still frozen. Solidification of the hydrogen must be avoided for safety. The temperature of the liquid target must be controlled in narrow temperature range between 14 and 20 K. The cryogenic refrigerator runs with its full power. The temperature of the target cell is controlled by changing the heater power. The heater was set at about 7 W for the liquid target, and at about 9 W for the "empty target". Figure 2.4 shows the target temperature and the heater power during the experiment. The temperature was stable within 0.4K, and the requirement mentioned above was satisfied [38].

The temperature of the target cell is measured with two Si diode sensors (Scientific Instruments, Inc. Si410A). The gas pressure at the reservoir is also measured with a pressure transducer (Satra 280E). The signals from the sensors are measured with digital multimeters (Hewlett Packard 34401A) sit near the target system. The data are acquired through GP-IB by a PC (Macintosh 8500/120). The heater power is fed by a programmable power supply (Hewlett Packard 6633B), which is controlled through GP-IB. Data acquisition and control is done remotely by LabView, which is the software from National Instruments [37]. The LabView is a graphical programming development environment for data acquisition and control, data analysis, and data presentation. The measured data are recorded on the computer for the off-line analysis [38, 39].

In addition to the remote control system, an emergency alert system is developed in hard-wired logic for safety. If the temperature exceeded the operational range, the system is stopped. Any error of the refrigerator, the heater or the computer also stops the operation.

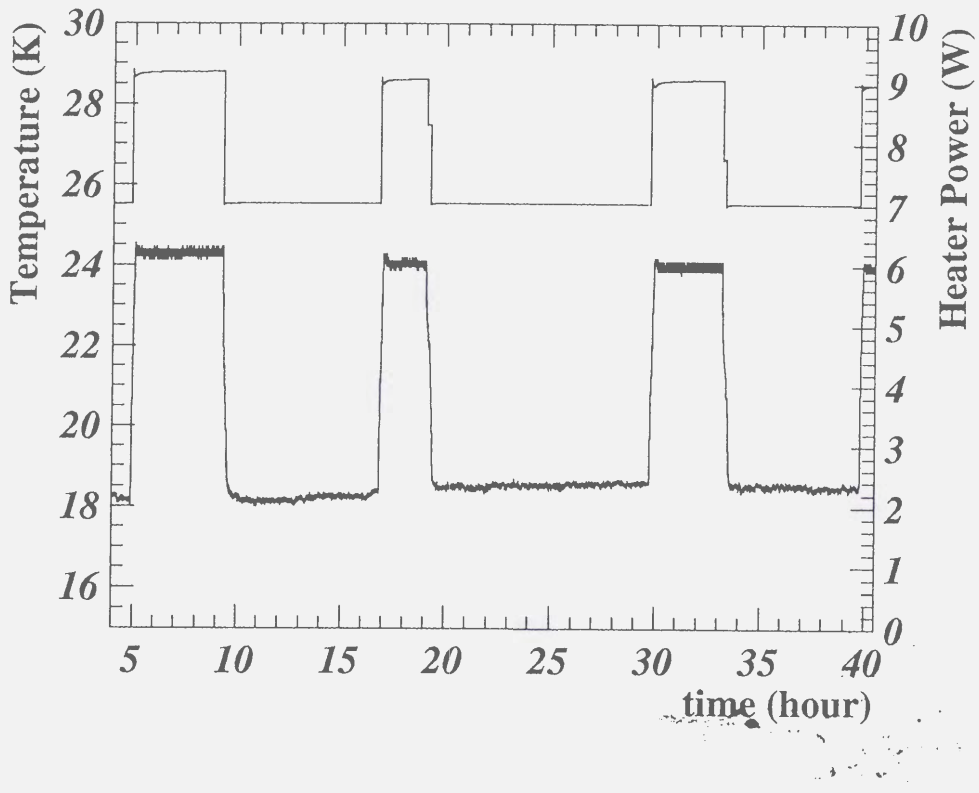

Figure 2.4: The target temperature and the heater power. The lower line indicates the target temperature and the upper one indicates the heater power. The data were taken at every 5 seconds.

Radius of the central orbit	300 cm
Total bending angle	162°
Maximum $B\rho$	5.4 Tm
Momentum bite	±2.5%
Solid angle	5.6 msr
Maximum momentum resolution	37076
Flight path for the central ray	20.0 m
Focal plane tilting angle	45.0°

Table 2.1: Designed parameters of the GR.

2.4 Beam halo monitor

In order to reduce the background caused by the beam halo, a beam halo monitor system which consisted of four plastic scintillators was set at about 105 cm upstream from the target (Fig. 2.1,2.2). The beam was tuned to minimize the counting rate of these plastic scintillators. The scintillators were set at 9 mm from the beam line, which is narrower than the target diameter (24 mm). A counting rate of each scintillator was less than 5 kcps at the beam current of 15 nA.

2.5 Spectrometer system

The two outgoing protons were detected with a two-arm spectrometer system, Grand Raiden (GR) and Large Acceptance Spectrometer (LAS). A schematic view of the two-arm spectrometer system is shown in Fig. 2.5.

2.5.1 High energy resolution spectrometer, Grand Raiden

The GR was designed and constructed for the purpose of high energy resolution measurements [40]. The designed value of momentum resolution, $p/\Delta p$, is about 37000, and magnetic rigidity is 5.4 Tm. These features allow us to carry out nuclear spectroscopy with high precision in the wide momentum range. Designed parameters of the GR are listed in Table 2.1.

The GR consists of three dipole magnets (D1,D2,and DSR), two quadrupole magnets (Q1,Q2), a sextupole magnet (SX) and a multipole magnet (MP) with a focal

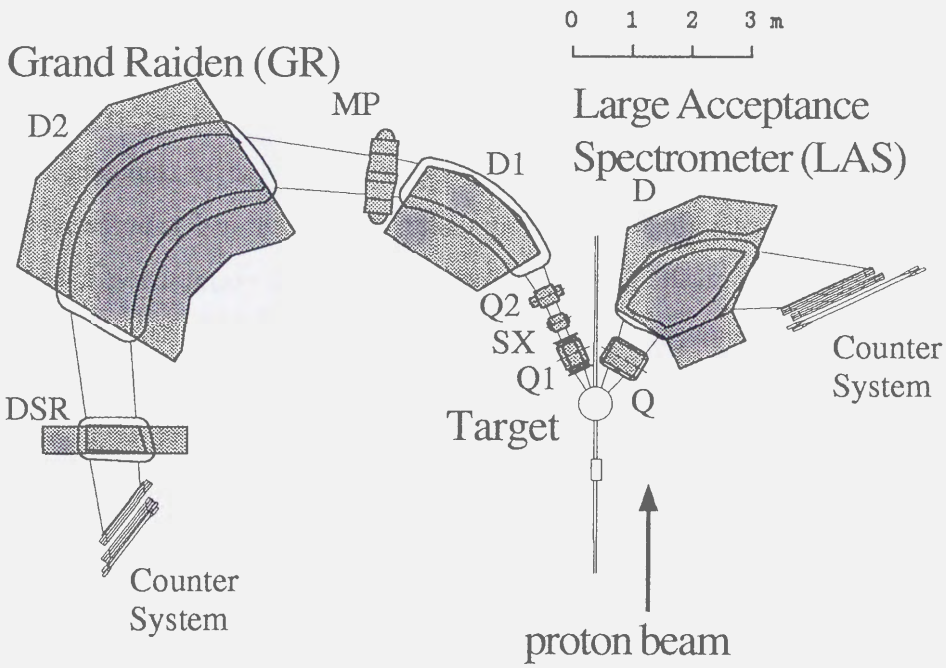

Figure 2.5: A schematic view of the two-arm spectrometer system, Grand Raiden (GR) and Large Acceptance Spectrometer (LAS).

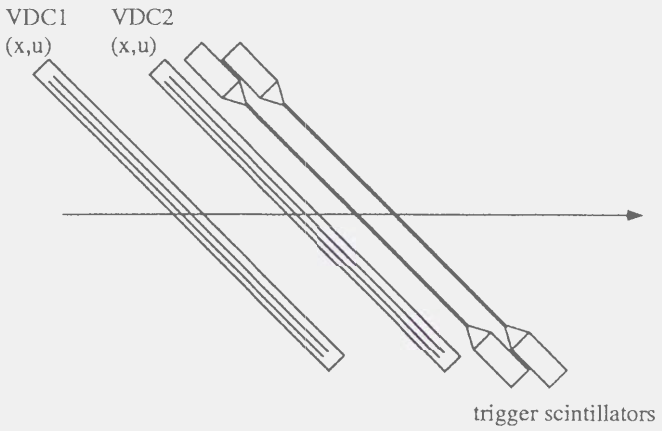

Figure 2.6: Focal plane detectors of Grand Raiden (GR)

plane counter system consisting of two sets of multi-wire drift chambers (GR–VDC1, GR–VDC2) and two trigger scintillators (Fig. 2.6). In the present measurement, the MP and DSR were not used. The magnetic fields of the dipole magnets (D1,D2) were measured by the NMR method during the experiment.

Specifications of the drift chambers are listed in Table 2.2. Each drift chamber consists of two sets of anode wire planes, sandwiched between two cathode planes. Figure 2.7 shows schematic view of one set of the anode and cathode planes. The cathode plane is made of a sheet of carbon-aramide foil. The anode plane consists of sense wires and potential wires. The potential wires serve to make a uniform electric fields between the cathode plane and the anode plane. The sense wires are made of gold-plated tungsten with a diameter of 20 μm. The potential wires are made of gold-plated copper-beryllium with a diameter of 50 μm. A chamber-gas consisting of argon (71%), isobutane (29%) was used. In addition, isopropyl-alcohol of saturated vapor at 2°C was mixed in the chamber gas. The maximum drift time is about 200 nsec and the typical position resolution is 300 μm [41].

The scintillation counters are placed just behind the GR–VDC2. There are two scintillation counters, GR–Front and GR–Rear. Each scintillation counter consists of a plastic scintillator with two photomultiplier tubes (PMT's) on both sides. Specifications of these scintillation counters are listed in Table 2.3. Signals from these counters are used to generate an event trigger signal (Section 2.8).

Area	1190 mm^W × 120 mm^H	
Drift space	10 mm	
Cathode Voltage	−5.6 kV	
Potential-wire Voltage	−300 V	
Sense-wire Voltage	0 V	
	x-plane	u-plane
Number of sense wire	192	208
Sense wire spacing	6 mm	4 mm
Tilt angle	0.0°	48.19°

Table 2.2: Specifications of GR drift chambers

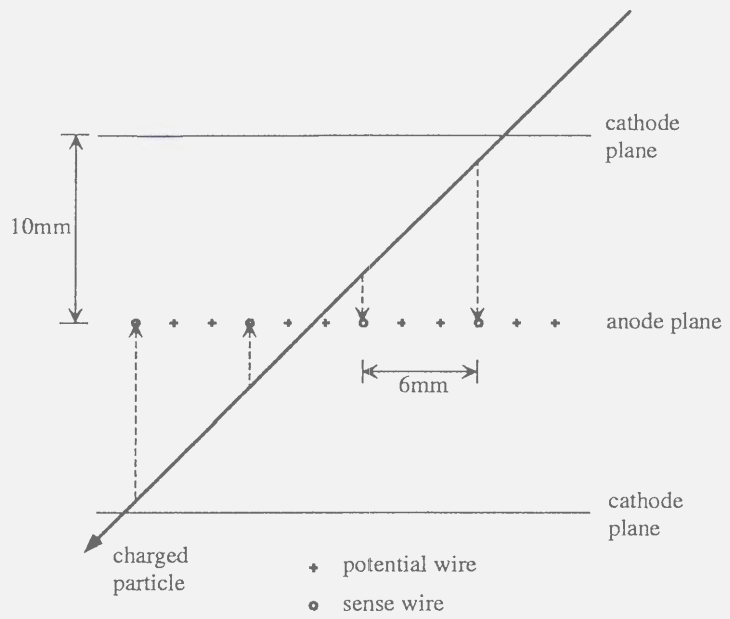

Figure 2.7: Schematic figure of one set of anode and cathode planes of the x–plane of the GR–VDC's

Area (cm)	1200 mm^W × 120 mm^H
Thickness	10 mm
PMT	H1161-50 (Hamamatsu) × 4

Table 2.3: Specifications of the scintillation counters of the GR

Radius of the central orbit	175 cm
Total bending angle	70°
Maximum $B\rho$	3.2 Tm
Momentum bite	±15.0%
Solid angle	~ 20 msr
Maximum momentum resolution	~ 0.02% FWHM
Flight path for the central ray	6.2 m
Focal plane tilting angle	~ 57°

Table 2.4: Designed parameters of the LAS.

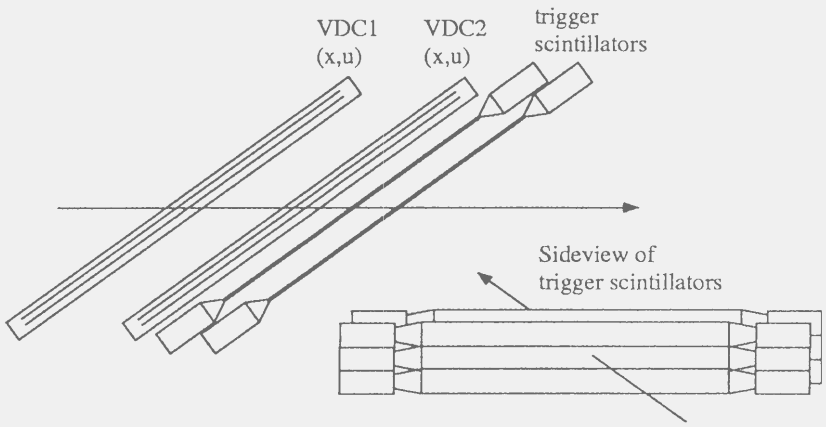

Figure 2.8: Focal plane detectors of the LAS

2.5.2 Large Acceptance Spectrometer

The LAS has relatively wide momentum and angular range [42]. It is a spectrometer complementary to the GR. The designed value of a momentum bite is about ±15% and a solid angle is about 20 msr. Designed parameters of the LAS are listed in Table 2.4.

The LAS consists of one dipole magnets (D) and one quadrupole magnet (Q) with a focal plane counter system consisting of two sets of multi-wire drift chambers (LAS–VDC1, LAS–VDC2) and trigger scintillation counters (Fig. 2.8). The magnetic field of the dipole magnet (D) was measured by the NMR method during the experiment.

The drift chambers, LAS–VDC1, LAS–VDC2, were the same type as the GR–VDC's. Specifications of the LAS–VDC's are listed in Table 2.5.

Area	1700 mm^W × 350 mm^H	
Anode-Cathode gap	10 mm	
Cathode Voltage	−5.3 kV	
Potential-wire Voltage	−300 V	
Sense-wire Voltage	0 V	
	x-plane	u-plane
Number of sense wire	272	256
Sense wire spacing	6 mm	6 mm
Tilt angle	0.0°	31.0°

Table 2.5: Specifications of LAS drift chambers

Area (cm)	2000 mm^W × 150 mm^H
Thickness	6 mm
PMT	H1949 (Hamamatsu) × 12

Table 2.6: Specifications of the scintillation counters of the LAS

The scintillation counters were placed just behind the LAS–VDC2. There are two scintillation counter systems, LAS–Front and LAS–Rear. Since the focal plane of the LAS is broad in vertical direction, three scintillation counters are set vertically in each system (Fig. 2.8). Each scintillation counter consisted of a plastic scintillator with two photomultiplier tubes (PMT's) on both sides. Specifications of these scintillation counters are listed in Table 2.6. Signals from these counters were used to generate an event trigger signal (Section 2.8).

2.5.3 Extra slits for the $pp\gamma$ experiment

The phase space of the $pp\gamma$ three-body system has large angular dependence at non-coplanar geometries. In order to avoid such large angular dependence, coplanar geometries are desirable [19]. Moreover, most of the theoretical calculations are performed at coplanar geometries. In order to select the coplanar $pp\gamma$ events, slits were placed in front of the magnets of the both spectrometers and limited the out-of-plane angles to ±30 mrad. Thickness of the slits were determined as they stop the protons from the pp elastic scattering.

	small	large
Area (cm)	5 mm^W × 5 mm^H	20 mm^W × 30 mm^H
Thickness	5 mm	5 mm
PMT	H3164B (Hamamatsu)	H3164B (Hamamatsu)

Table 2.7: Specifications of the Luminosity monitor

2.6 Luminosity monitor

The luminosity was measured by observing the pp elastic scattering on the liquid hydrogen target. These protons were detected with a luminosity monitor (LM), which consisted of two plastic scintillation counters and set in the scattering chamber. A schematic view of the LM is shown in Fig. 2.9. In order to eliminate the effect of the beam polarization, the LM was set at 90° in the center of mass system (42.2° in the laboratory system) vertically. A distance from the target to each scintillator was 33.8 cm. Two protons from the liquid hydrogen target were detected with the scintillation counters by the coincidence method. The acceptance of the LM for the pp elastic scattering was defined by the small scintillator and about 0.25 msr. The specifications of the LM are listed in Table 2.7.

2.7 Experimental procedure

In the present measurement, the angular distribution of the photon was measured as two out-going protons were scattered at fixed angles. The protons were detected with the spectrometers and the four-momentum of the third out-going particle was calculated from the momenta of the protons. Figure 2.10 shows 2-dimensional plot of the momenta of the out-going protons from the $pp\gamma$ reaction. The scattering angles are both 26°. The photon emission angles are also shown in the figure. It shows that the angular distribution is measured by changing the measurement region of the momenta of the out-going protons.

The $pp\gamma$ events can not be covered by one magnetic field setting due to the limited momentum acceptances of the GR and LAS, so that we have chosen 14 settings of the two-arm spectrometer in order to measure the angular distribution of the photon emission between 0° and 180°. Figure 2.11 shows the $pp\gamma$ phase space corresponding

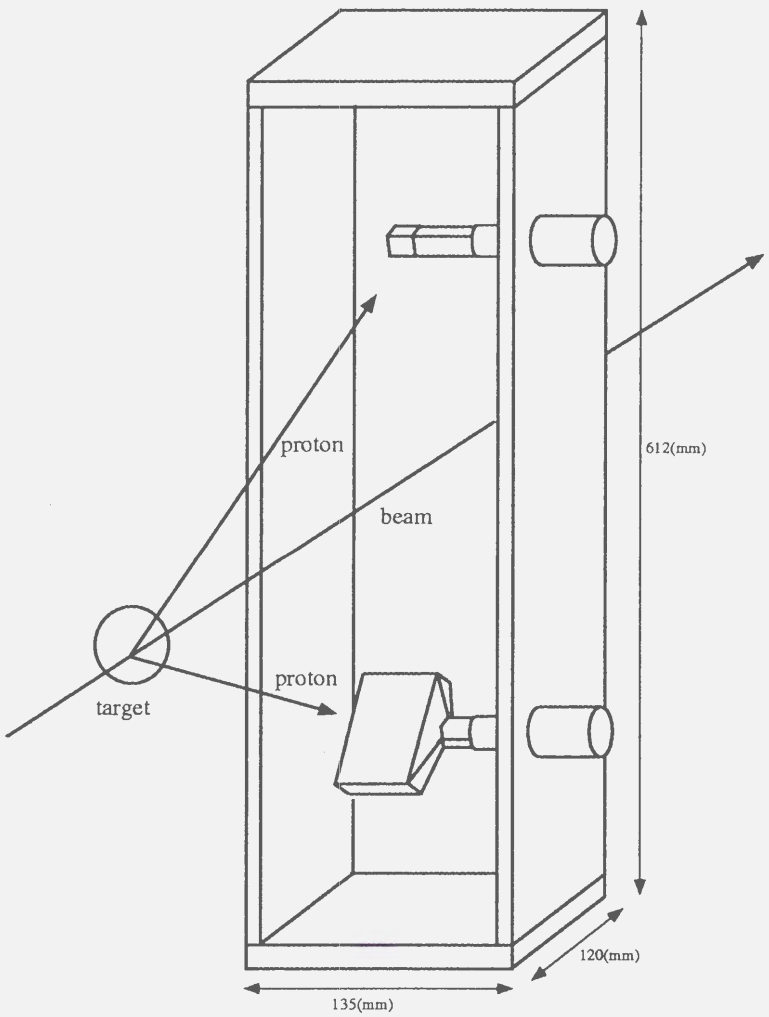

Figure 2.9: A schematic view of the Luminosity monitor. It was set in the scattering chamber.

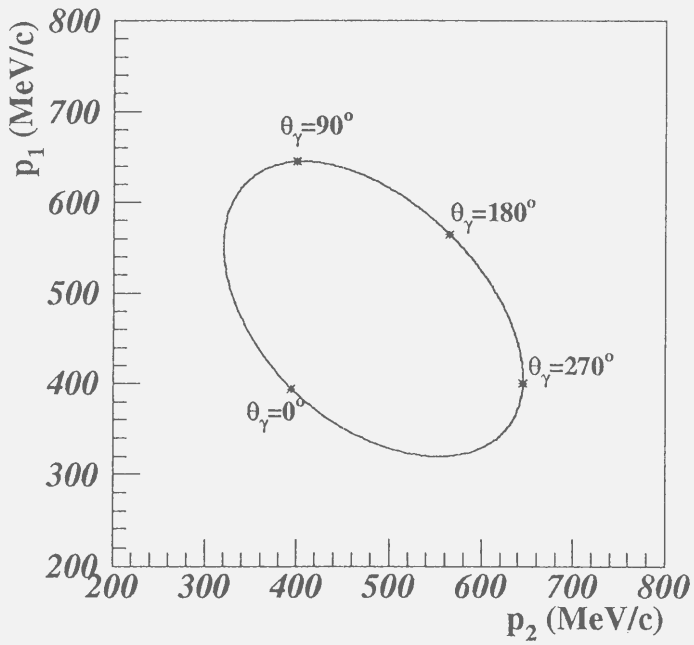

Figure 2.10: The Two-dimensional plot of the momenta of the protons from the $pp\gamma$ reaction. The incident energy is 389.3 MeV and the scattering angles of the two protons are both 26°.

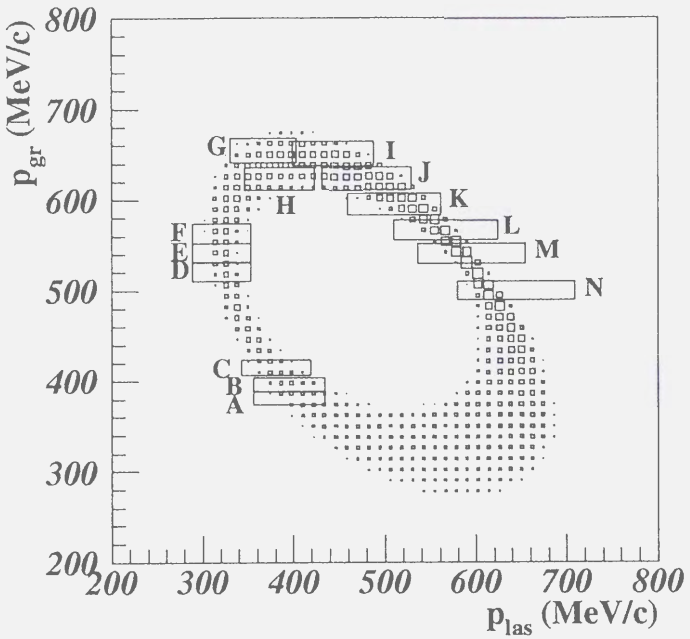

Figure 2.11: The $pp\gamma$ phase space as a function of the momenta of the two protons at our experimental setting. The boxes in this figure are the momentum acceptances for each magnetic field setting. This is obtained with a phase space calculation.

to the momenta of the two protons, with the geometrical acceptances of the two-arm spectrometer taken into account. The boxes $A - N$ in this figure correspond to the 14 magnetic field settings. The relations between the magnetic field settings and the photon emission angles are summarized in Table 2.8.

The "empty target" runs were performed at each magnet field setting before or after the liquid hydrogen target run in order to reduce the uncertainty of the background estimation.

In addition to these data, the data of $p+p$ and $p+^{12}$C elastic scattering from CH_2 target were taken. The data of $p+^{12}$C elastic and inelastic scattering from the target container foils (12.5 μm aramide) were also taken. These data were used for various

Magnetic field setting	θ_γ (degree)	p_{GR} (MeV/c)	p_{LAS} (MeV/c)
A	$-10 \sim 10$	381.0	395.4
B	$-10 \sim 10$	395.4	395.4
C	$-10 \sim 10$	415.0	380.4
D	$20 \sim 40$	521.0	321.0
E	$20 \sim 40$	541.0	321.0
F	$20 \sim 60$	563.0	321.0
G	$40 \sim 80$	623.0	382.0
H	$60 \sim 100$	654.6	367.0
I	$80 \sim 140$	651.0	443.6
J	$100 \sim 180$	624.0	480.0
K	$120 \sim 200$	595.2	510.0
L	$140 \sim 220$	566.8	566.8
M	$160 \sim 220$	540.0	595.2
N	$180 \sim 260$	499.5	644.0

Table 2.8: Photon emission angles for each magnetic field setting. The settings $F-N$ cover a wide range of the photon emission angles. Momentum setting for the central ray for each magnetic field setting are also indicated.

calibrations such as the beam energy, the solid angle of the spectrometers and the luminosity monitor and so on.

2.8 Trigger and data acquisition

Three kinds of triggers for the data acquisition were prepared: (i) GR single-arm trigger (**GR**), (ii) LAS single-arm trigger (**LAS**), and (iii) two-arm trigger (**GR** · **LAS**). Those trigger signals were exclusively generated. The trigger diagram is shown in Fig. 2.12. The **GR** and **LAS** consisted of the coincidence of the signals from the Front and Rear scintillation counter(s). In the magnetic settings corresponding to $\theta_\gamma = 30°$ ($D-F$ in Fig. 2.11 and Table 2.8), the **LAS'** was used instead of the **LAS**, because the proton momentum was not high enough to punch through the Front scintillators. The triggers of (i) and (ii) were prescaled in order to reduce the dead time of the data acquisition system.

The signals from the detectors are digitized with ADC and TDC modules in the CAMAC crates. LeCroy FERA/FERET systems are used for the scintillation

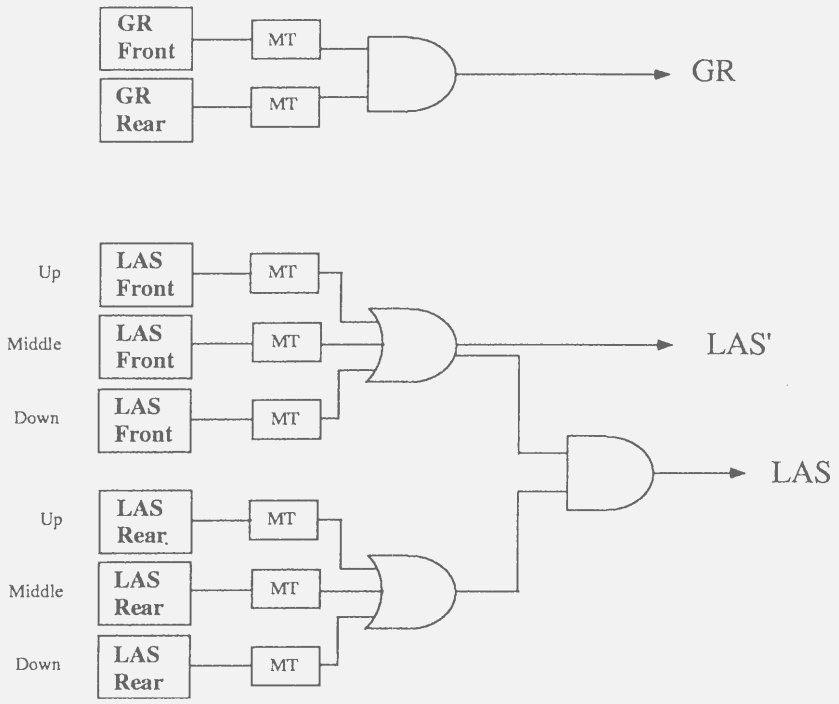

Figure 2.12: Trigger diagram. MT represents a mean timer module.

counters and LeCroy 3377 drift chamber TDC's are used for the VDC's. Data from the modules are transferred to memory modules in the VME crate and stored. A pair of the buffer memory modules is assigned to each counter system. When data in one of the buffer modules exceed their maximum size, all the buffers are switched to their partner buffers simultaneously. The data are transferred to a SUN Sparc 20 work station through a fiber-optic ring [43]. The work station transfers the data to a Digital Unix Alpha Server 4100 computer by TCP/IP connections on FDDI. The server stores the data on a hard disk. Online event analysis is also performed on it.

The data–acquisition efficiency was 90–99% depending on the counting rate.

Chapter 3

Data Analysis

3.1 Overview

In this chapter, procedures to deduce the differential cross sections and analyzing powers from the raw data are described. The procedure of the offline analysis for the $pp\gamma$ event was performed as follows.

1. Event selection for the **GR** · **LAS** trigger.
2. Analysis of the VDC's.
3. Event identification with true timing and accidental coincidence from the time difference spectrum between the timing of the GR's trigger scintillators and that of the LAS's.
4. Event selection with kinematical conditions.
5. Event selection within a missing mass gate.
6. Background subtraction.

The beam energy was important to obtain kinematical variables of the missing particle. The absolute value of the beam energy was deduced from the measurement of the proton-nucleus elastic and inelastic scattering (Sec. 3.5). The beam polarization was obtained by the measurement of the pp elastic scattering from a CH_2 target with the "WN" BLP (Sec. 3.2). The integrated beam current was measured with the

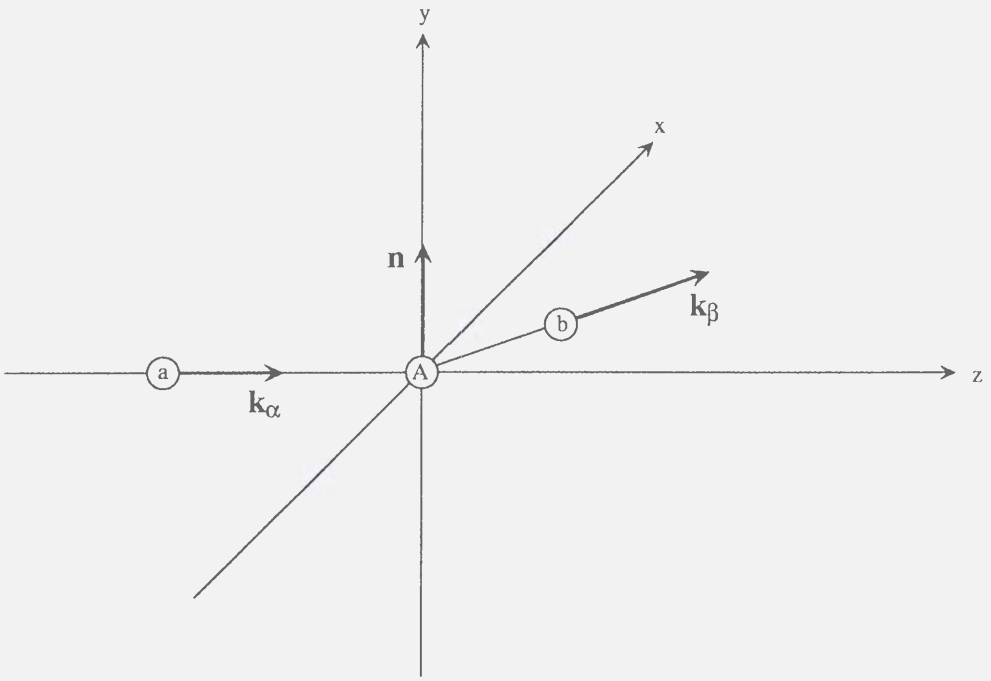

Figure 3.1: Definition of the polarization vector.

"Cave" BLP (Sec. 3.3). The luminosity was measured with the luminosity monitor (LM), which detected the *pp* elastic scattering events from the liquid hydrogen target (Sec. 3.4). The accuracy of the absolute normalization was checked by measuring the *pp* elastic scattering and comparing with a result of a phase shift calculation, *SAID* [47].

3.2 Beam polarization

At first, the direction of the beam polarization, $\vec{n}$, is defined as,

$$\vec{n} = \frac{\vec{k_\alpha} \times \vec{k_\beta}}{|\vec{k_\alpha} \times \vec{k_\beta}|}, \tag{3.1}$$

where $\vec{k_\alpha}$ and $\vec{k_\beta}$ are the momentum vectors of the incident and scattered particles respectively.

The beam polarization was measured with the "WN" polarimeter. It detected the *pp* elastic scattering events from the CH_2 target. The beam polarization was deduced

from the left-right asymmetry. Numbers of the scattered protons are expressed as

$$N_L^{\uparrow} = \sigma_0 N_t C^{\uparrow} \Omega_L (1 + A_y p^{\uparrow}), \tag{3.2}$$

$$N_L^{\downarrow} = \sigma_0 N_t C^{\downarrow} \Omega_L (1 + A_y p^{\downarrow}), \tag{3.3}$$

$$N_R^{\uparrow} = \sigma_0 N_t C^{\uparrow} \Omega_R (1 - A_y p^{\uparrow}), \tag{3.4}$$

$$N_R^{\downarrow} = \sigma_0 N_t C^{\downarrow} \Omega_R (1 - A_y p^{\downarrow}), \tag{3.5}$$

where σ_0 is the unpolarized cross section, and N_t is number of the target nuclei. Integrated beam currents are denoted as $C^{\uparrow}$ and $C^{\downarrow}$ for the spin-up and spin-down mode, respectively. The integrated beam currents are proportional to the counts of the "WN" BLP, and the sum of the "WN" BLP counts is used for the integrated beam currents. The solid angles for the left and right sides are denoted as Ω_L and Ω_R, respectively. The ratio of the solid angle is calculated as

$$\frac{\Omega_R}{\Omega_L} = \frac{-C^{\uparrow} N_R^{\downarrow} + C^{\downarrow} N_R^{\uparrow}}{C^{\uparrow} N_L^{\downarrow} - C^{\downarrow} N_L^{\uparrow}}. \tag{3.6}$$

In the measurement with the "WN" BLP, the CH_2 target is used and background events due to $^{12}C(p,2p)$ reaction exist. These background events reduce the analyzing power at the "WN" BLP. The reduced analyzing power is $A_y = 0.45 \pm 0.01$ at proton incident energy of 392 MeV and $\theta = 17.0°$, which was measured in another experiment at the RCNP [35]. The beam polarization is calculated as

$$p^{\uparrow} = \frac{1}{A_y} \frac{-N_R^{\uparrow} + N_L^{\uparrow}(\Omega_R/\Omega_L)}{N_R^{\uparrow} + N_L^{\uparrow}(\Omega_R/\Omega_L)}, \tag{3.7}$$

$$p^{\downarrow} = \frac{1}{A_y} \frac{-N_R^{\downarrow} + N_L^{\downarrow}(\Omega_R/\Omega_L)}{N_R^{\downarrow} + N_L^{\downarrow}(\Omega_R/\Omega_L)} \tag{3.8}$$

for the spin-up and the spin-down mode, respectively. In this notation, $p^{\uparrow}$ and $p^{\downarrow}$ are defined as $p^{\uparrow} \geq 0$ and $p^{\downarrow} \leq 0$. The beam polarization was typically 70%.

3.3 Beam current

The integrated beam current was measured with the "Cave"-BLP. In order to eliminate the effect of the beam polarization, the numbers of the four counters were

summed up. The integrated beam current was evaluated from the "Cave"-BLP counts with the following expression,

$$C = C_{cave}(N_L + N_R + N_U + N_D)\,, \tag{3.9}$$

where C is the integrated beam current, N_L, N_R, N_U, and N_D are the numbers of events detected with the left, right, up, and down counters of the "Cave"-BLP respectively, and C_{cave} is the normalization constant. In order to obtain C_{cave}, we performed calibration runs which measured the integrate beam current with the Faraday cup in the scattering chamber. These runs were performed several times and we checked the change of the C_{cave} during the experiment due to the change of the thickness of the aramide target. Figure 3.2 shows the C_{cave} deduced by the Eq. (3.9) with the calibration runs. In order to check the effect of the beam polarization, C_{cave} was deduced in the case of the spin up mode and down mode respectively, and we denote these values as $C^{\uparrow}_{cave}$ and $C^{\downarrow}_{cave}$ respectively. The ratio of the $C^{\uparrow}_{cave}$ and $C^{\downarrow}_{cave}$ was 0.996 ± 0.012, which is consistent with 1. This shows that C_{cave} is independent of the beam polarization and we do not take into account the beam polarization as the estimation of the integrated beam current. The charge of the proton beam collected with the Faraday cup is digitized by a current integrator. The current integrator used in the present experiment was calibrated with the measurement of the charge from a current source [48]. The value of the C_{cave} is

$$C_{cave} = (2.019 \pm 0.048) \times 10^9 \text{ (protons/count)}\,, \tag{3.10}$$

where the error of the calibration factor of the current integrator and the fluctuation of the C_{cave} at each calibration run are included.

3.4 Luminosity

The luminosity was measured with the luminosity monitor (LM) which counted pp elastic scattering events from the liquid hydrogen target. The background from the target container foils was estimated with the "empty target" run and subtracted.

In order to calibrate the LM, the luminosity was evaluated from the following expression,

$$\mathcal{L} = C N_{LH_2} \tag{3.11}$$

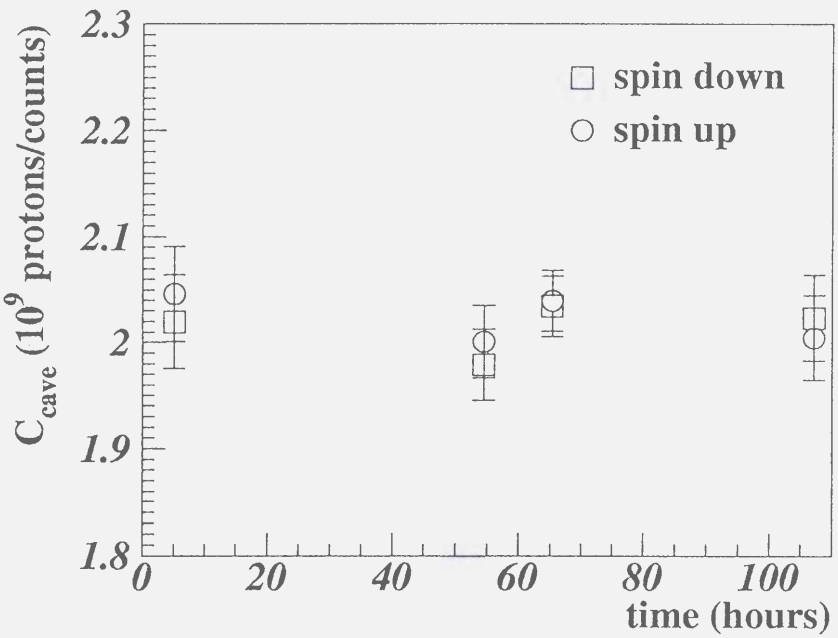

Figure 3.2: Time dependence of the ratio between the integrated beam current and number of counts measured with the "Cave" polarimeter.

where C is the beam current measured with the "Cave"-BLP and N_{LH_2} is the target thickness. The thickness of the liquid hydrogen target was deduced by measuring the pp elastic scattering from both the CH_2 target and the liquid hydrogen target with the GR. The thickness of the CH_2 target is 2.37 ± 0.05 mg/cm^2, which was obtained by measuring its weight. The deduced value of the thickness of the liquid hydrogen target is $(3.80 \pm 0.10 \pm 0.08) \times 10^{22}$cm^{-2}, which corresponds to about 9 mm thickness. The former error is a statistical one, and the latter is the systematic one due to the uncertainty of the thickness of the CH_2 target. The number of counts detected with the LM is proportional to the luminosity,

$$\mathcal{L} = C_{lum} N_{LM} , \tag{3.12}$$

and the proportional constant C_{lum} was determined using a following expression,

$$C_{lum} = \frac{C N_{LH_2}}{N_{LM}} . \tag{3.13}$$

The background events from the target container foils were estimated with the "empty target" run, which was performed with the gas target at the temperature of about 24K in this case. The density of the hydrogen gas at 24K is 2.6% of that of the liquid hydrogen. This means that 2.6% of the pp elastic scattering events were subtracted in the background subtraction. We corrected N_{LM} and deduced C_{lum} using Eq. (3.13). The value of C_{lum} is $(3.82 \pm 0.17) \times 10^{29}$ cm^{-2}, where the error includes the statistical and systematic ones. The errors for the C_{lum} are summarized in Table. 3.1.

The pp elastic scattering cross section is obtained from the C_{lum} with the following expression as

$$\frac{d\sigma}{d\Omega} = \frac{1}{\Delta\Omega_{LM} C_{lum}}, \tag{3.14}$$

	error (%)	comment
C_{cave}	2.4	
N_{LH_2}	3.4	
N_{CV}	1.5	statistical error
N_{LM}	0.1	statistical error
total	4.4	

Table 3.1: Errors for the C_{lum}.

where $\Delta\Omega_{LM}$ is the solid angle of the LM, which is determined by the small scintillator. The value of the $\Delta\Omega_{LM}$ is 0.246 ± 0.024 msr. The accuracy of the LM was checked by comparing the measured cross section with the result of the *SAID*. The measured cross section was 10.65 ± 1.12 mb/sr, where the statistical and systematic errors are included. This is consistent with the result of the *SAID* program (10.90 mb/sr) [47] within the errors.

In order to study the stability of the LM, the ratio of the N_{LM} and the integrate beam current C was checked run by run. Series of runs that the target temperature was constant within 0.1K are selected in order to avoid the effect of the change of the hydrogen density. The results of one series are shown in Fig. 3.3. The runs were taken within 10 hours in this series. The ratios between the number of events detected with the LM and the "Cave"-BLP were constant within 0.6% during the experiment.

3.5 Beam energy

The beam energy was evaluated from the proton momentum of the proton nucleus scattering from the CH_2 target and the target container foil (12.5 μm aramide). The proton momentum was measured with the GR. The measurements were performed at two scattering angles, $\theta_{GR} = 26.0°$ and $\theta_{GR} = 33.2°$. We performed the gas target run for the measurement with the target container foils, which is called the aramide target run in this section. The energy loss in the target was less than 15 keV and not taken into account in this analysis. Figure 3.4 shows a momentum spectrum of the protons from the CH_2 target at $\theta_{GR} = 33.2°$ (a) and the aramide target at $\theta_{GR} = 26.0°$ (b) measured with the GR. The horizontal angular acceptance was limited to ± 5 mrad by a software cut. Two peaks corresponding to the ground state and the 2^+(4.44MeV) were used for the evaluation of the beam energy in the measurement with the CH_2 target and the aramide target at $\theta_{GR} = 33.2°$. In the case of the aramide target at $\theta_{GR} = 26°$, two peaks corresponding to the ^{12}C ground state and ^{16}O ground state were used, because the peaks corresponding to the 2^+(4.44 MeV) of ^{12}C and 3^-(6.13 MeV) of ^{16}O were overlapped and it was difficult to separate these two peaks. The beam energy was calculated independently with the two states. The differences of the beam energy obtained with the two states were less than 80 keV. The measurements

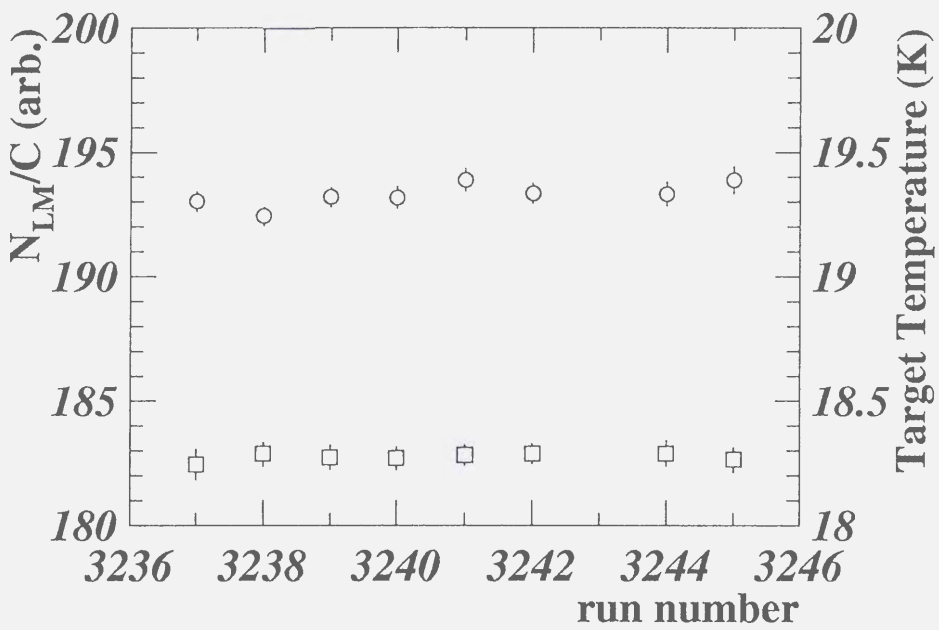

Figure 3.3: Stability of the LM during the measurement. The horizontal axis shows the run number, the left vertical axis shows the ratio between the number of events detected with the LM and the "Cave" BLP (open circle), and the right vertical axis indicates the target temperature (open square). The target temperature was recorded at every 10 seconds, and a mean was taken at each run. The errors indicate the fluctuation of the temperature. These runs were taken within 10 hours.

were performed several times during the experiment. There was 1.5 MeV change in the beam energy during the experiment. The average value was 388.6 ± 1.0 MeV.

3.6 Momentum analysis

The momentum vector of the scattered particle was obtained from the VDC's data for both spectrometers. Since the angle between the anode plane and the particle trajectory is 45° for the GR and 36° for the LAS, several sense wires along a single particle trajectory put out signals. In the present analysis, more than two hit wires were required for each VDC. A straight track at the focal plane of the spectrometer was deduced using a least-square method. In finding the track, all combinations of left/right ambiguity were examined and the track which gave the least χ^2-value was chosen. For multi-hit events, all possible combinations were examined and the position at each VDC was calculated for each track. If there was only one track whose position was within the window size of the VDC's, it was chosen for the further analysis.

As an efficiency of the VDC's, the detection efficiency of the plane and the reduction of the multi track events were taken into account. The detection efficiency of each VDC was more than 99%, and the track-finding efficiencies were about 98% for the GR and $95 - 98\%$ for the LAS.

The momentum and horizontal angle of the detected proton were determined from the track using a transport matrix. The vertical angle for the GR was not obtained with the transport matrix. In the case of the LAS, the vertical angle was calculated with the transport matrix. The resolution of the vertical angle was, however, poor, and as same as the acceptance of the vertical angle (± 30 mrad). Therefore the information of the vertical angle is not used in the present analysis. The matrix for the GR was calculated from the designed values and modified using data of $^{12}C(p,p)$ and $^{12}C(p,p')$ scattering with the CH_2 target. The matrix for the LAS was obtained by a Monte Carlo calculation [42]. The horizontal angle was modified using a measurement of the pp elastic scattering with the CH_2 target.

The accuracy of the scattered angle was checked with the measurement of the pp elastic scattering with the CH_2 target at 26.0 degree. A root mean square is evaluated

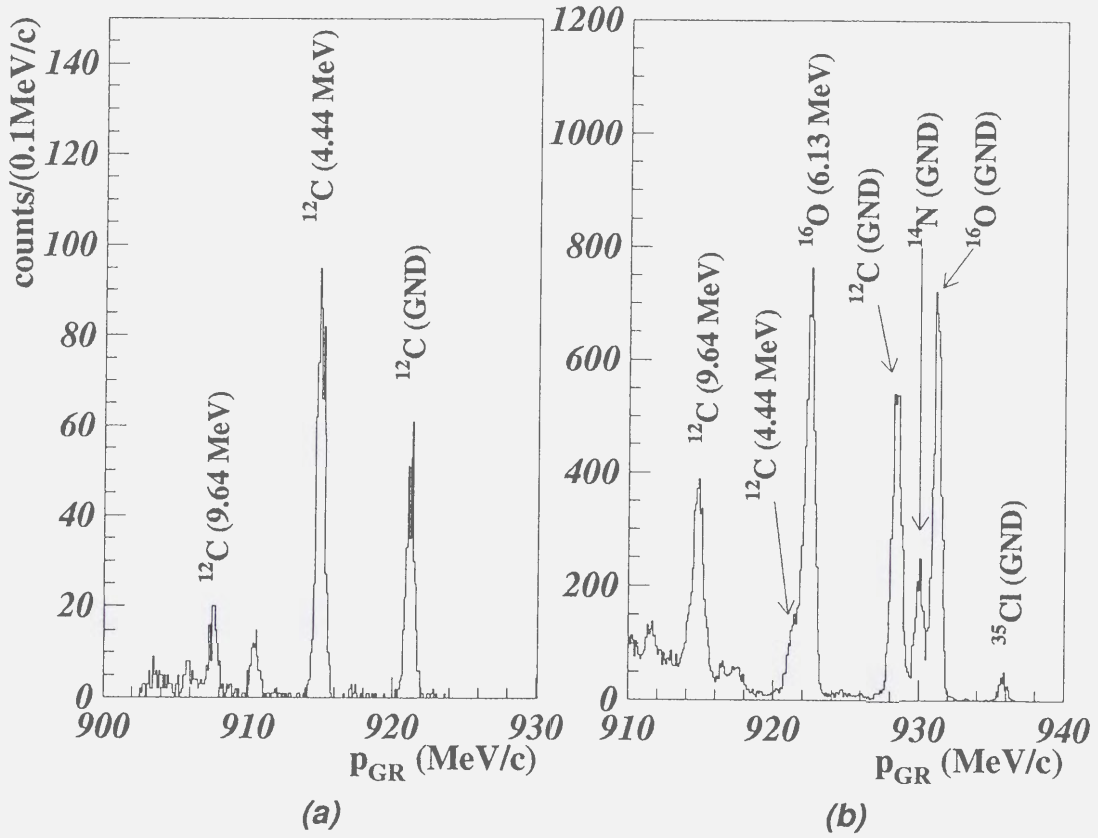

Figure 3.4: Momentum spectrum of the scattered proton from the CH_2 target at $\theta_{GR} = 33.2°$ (a) and from the aramide target at $\theta_{GR} = 26.0°$ (b). They were obtained with the GR. The acceptance of the horizontal angle was limited to ± 5 mrad by a software cut.

with an angular difference spectrum between the data and kinematical calculations. The values of the root mean square are 0.73 mrad for the GR and 1.4 mrad for the LAS, respectively. These are used for the evaluation of the systematic errors of the solid angles.

The momentum resolutions were obtained with the measurement of the p-^{12}C elastic scattering with the CH_2 target at $\theta = 26°$. The momentum resolutions, $\Delta p/p$ of the GR and LAS are 0.045% and 0.060% (FWHM) respectively for the 928 MeV/c proton. The effect of the beam energy spread is included in those values.

The acceptances of the momentum and horizontal angle were limited by a software cut. The momentum acceptances are ±2% for the GR and ±10% for the LAS. The horizontal angular acceptances for the GR and LAS are ±15 mrad and ±60 mrad, respectively.

3.7 Event reconstruction

The four-momentum of the third out-going particle was calculated with the momenta of the two outgoing protons using a following expression;

$$p_3^\mu = p_{beam}^\mu + p_{target}^\mu - p_{GR}^\mu - p_{LAS}^\mu. \tag{3.15}$$

Due to a poor resolution of the vertical angles measured with the spectrometers, the values of vertical angles were set to be 0 for the further analysis. (All events were assumed to be coplanar.)

A squared invariant mass of the third out-going particle or a squared missing mass for the $pp \rightarrow ppX$ reaction is calculated from the expression

$$M_X^2 = E_3^2 - \vec{p}_3^{\,2}. \tag{3.16}$$

The missing mass spectra were used for the analysis. Details are expressed in Sec. 3.10.

3.8 Timing between the GR and LAS

In a coincidence measurement, two independently scattered protons may enter the spectrometer in an accidental coincidence in addition to the true coincidence event.

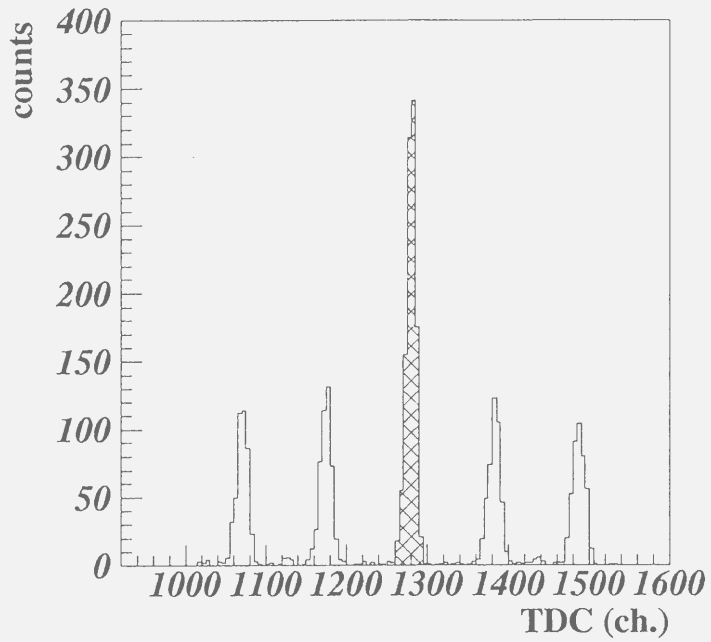

Figure 3.5: The time difference between the signals from the GR and LAS. This was obtained from the measurement of the magnetic field setting I. The hatched area shows the "true" gate.

We estimated the number of these events from coincidences coming from different beam bunches. Figure 3.5 shows a spectrum of time difference between the signals from the trigger counters of the GR and LAS. The largest peak includes both true and accidental coincidence events, whereas the other 4 peaks include only accidental coincidence events. In the present analysis, two gates were applied; one is the "true" gate corresponding to the largest peak (hatched area in Fig 3.5), the other is the "accidental" gate (unfilled area in Fig 3.5). The background events due to the accidental coincidence were estimated from the events included in the "accidental" gate. The sources of the accidental coincidence event are discussed in Sec. 3.9.

3.9 Background

At an incident energy of 389 MeV, there are large possible sources of background. Using the two-arm spectrometer and the liquid hydrogen target, we suppressed these backgrounds and obtained the $pp\gamma$ events with good signal-to-noise ratio [44]. In this section, possible background sources are discussed.

3.9.1 $pp \to pp\pi^0$ reaction

The $pp \to pp\pi^0$ reaction has a rather large cross section of 48μb at 389 MeV [45]. It is about 10 times larger than the $pp\gamma$ cross section. Figure 3.6 shows the phase space of the $pp\gamma$ and $pp\pi^0$ reactions corresponding to the momenta of the two protons, with the geometrical acceptance of the two-arm spectrometer. In this figure, the phase space of the $pp \to pn\pi^+$ reaction corresponding to the momenta of the proton and π^+ is also shown and discussed later. The boxes show the momentum acceptances of the two-arm spectrometer system. The distribution of the $pp\pi^0$ events is out of the acceptances and two protons from the $pp\pi^0$ process are not detected with the magnetic field settings for the $pp\gamma$ measurement.

3.9.2 $pp \to pn\pi^+$ reaction

The $pp \to pn\pi^+$ reaction ($pn\pi^+$) has an about 7 times larger cross section than that of the $pp \to pp\pi^0$ reaction. There are two charged particles in the final state and the $pn\pi^+$ events can cause the background. In Fig. 3.6, the $p\pi^+n$ and π^+pn phase spaces are shown in addition to the phase space of the $pp\gamma$ and $pp\pi^0$. The proton is assumed to be detected by the GR and the π^+ by the LAS in the $p\pi^+n$, and the π^+ is detected by the GR and the proton by the LAS in the π^+pn. The momentum of the π^+ is different from that of the proton from the $pp\gamma$ reaction and the π^+ is not detected by the spectrometer system at our magnetic field settings.

3.9.3 Proton-nucleus inelastic scattering

The protons scattered inelastically by the nuclei in the target container foils are distributed to a wide momentum range. A part of the protons whose momentum is

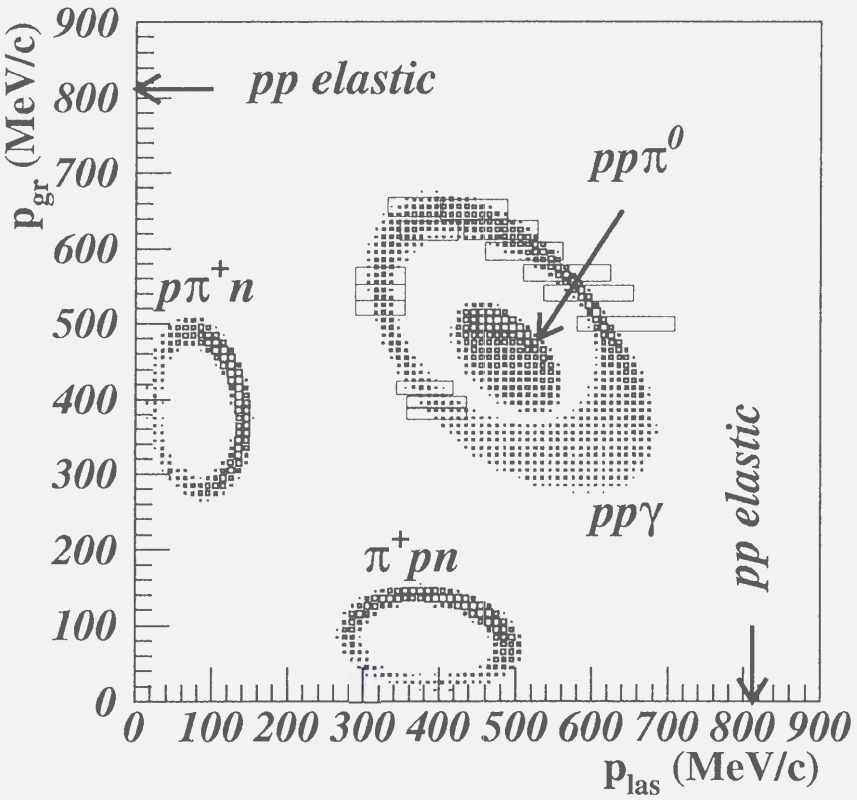

Figure 3.6: The $pp\gamma$ and $pp\pi^0$ phase space as a function of the momenta of the two protons, and the $pn\pi^+$ phase space as a function of the momenta of the proton and π^+ at our experimental setting. The boxes in this figure are the momentum acceptances for each magnetic field setting. These are obtained with a phase space calculation.

θ_1 (deg.)	p_1 (MeV/c)	θ_2 (deg.)	p_2 (MeV/c)
26.0	811.8	59.5	413.0

Table 3.2: Kinematical variables of the pp elastic scattering at $T_p = 389.3$ MeV.

within the acceptance of the spectrometer causes trigger. Two independently scattered protons may enter the spectrometer in an accidental coincidence in addition to the true coincidence event. We estimated the number of these events from coincidences coming from different beam bunches as discussed in Sec. 3.8.

3.9.4 (p,2pX) reaction from nuclei

The A(p,2pX) events from nuclei of the target container foils contributed to the background. The magnitude of this contribution was estimated from the "empty target" runs (Sec. 2.3). The yield of the "empty target" run was normalized to the liquid hydrogen target run using the "Cave" BLP counts.

3.9.5 pp elastic scattering

Protons from the pp elastic scattering from the target hydrogen also cause large backgrounds. The momenta and angles of the protons one of which is scattered to 26.0 degree (the present setting) are listed in Table 3.2. The momentum of the proton scattered to 26.0 degree is far from the momentum acceptances for the $pp\gamma$ measurement (Fig. 3.6). The angle of the other proton is much different from the 26.0 degree, and the proton is not detected by the present spectrometer setting. A part of the protons which is scattered from the wall and loses energy in the spectrometer hits the trigger scintillators. It causes the accidental coincidence event.

3.9.6 Double scattering in the liquid hydrogen target

If the pp elastic scattering take place twice in the liquid hydrogen target, there are four outgoing protons. Two of them may be measured with the true timing, and it causes a background event. The yield of those events was estimated using a Monte Carlo simulation and 3 order smaller than that of the $pp\gamma$ events.

There are possibilities of detecting two protons both at 26 degree when the pp elastic scattering takes place after the $pp \to pp\pi^0$ reaction and the $np \to pn$ reaction takes place after the $pp \to pn\pi^+$ reaction. We studied these reactions with a Monte Carlo simulation. The events from these reactions are not detected in the present magnetic field settings.

3.10 Missing mass analysis

Figure 3.7 shows the missing mass spectrum of two magnetic field settings. In the upper figures, the results of the liquid hydrogen target run with the true gate (solid), with the accidental gate (dashed), and of the "empty target" run (dotted) are shown. In the lower figures, the yields of the accidental coincidence and the "empty target" run were subtracted from those of the liquid hydrogen target run. The peaks around 0 MeV^2 correspond to the $pp\gamma$ events.

The missing mass spectra of the all magnetic field settings are shown in Fig. 3.8 and Fig. 3.9. The dashed lines are the result of a Monte Carlo simulation, which is normalized to the data. In this simulation, the $pp\gamma$ events are generated with the phase space distribution, and the effects of the energy straggling and multiple scattering in the liquid hydrogen target and the momentum and angular resolutions of the spectrometer are taken into account. In general, missing mass spectra are well accounted by the simulation. There is a small difference between the peak position of the data and the simulation in some settings. This is possibly due to the uncertainty of the measured proton momentum and of the beam energy. The peak position of the simulation was shifted to fit the data. The width of the gate was defined with the simulation so as to include more than 98.5% of the $pp\gamma$ events.

Uncertainties due to the gate width were derived from varying the width of the missing mass gate of $\pm 20\%$. The change of the simulated $pp\gamma$ events is within 0.4% when there is a $\pm 20\%$ change in the width of the missing mass gate. The uncertainty for each magnetic field setting is $2 - 17\%$, and it is smaller than the statistical error. It was taken into account in the evaluation of the cross section and analyzing power.

In order to confirm that the background events were estimated correctly, the events were counted in the region where the $pp\gamma$ events were not distributed. The missing

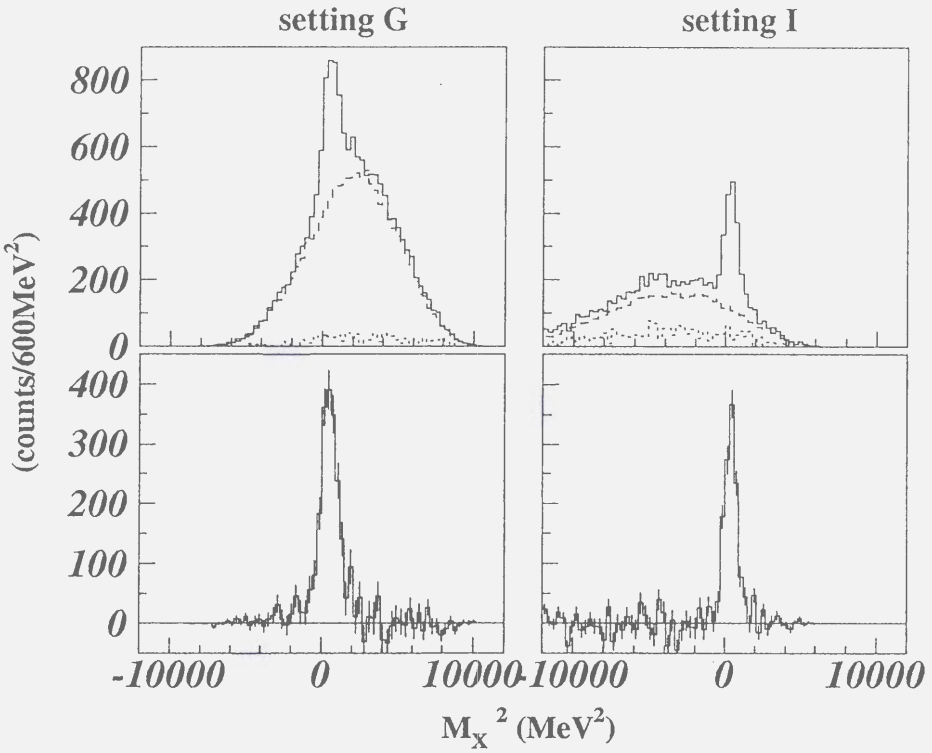

Figure 3.7: The squared missing mass ($M_X{}^2$) spectra reconstructed from the two observed proton momenta. The results of the G and I magnetic field settings are shown. Upper figures : Solid lines are taken from the liquid hydrogen target runs and dashed lines correspond to the accidental coincidence events. Dotted lines are the contributions from the *A(p,2p)* quasi elastic events from nuclei of the target foils, which are taken from the "empty target" runs. Lower figures : After subtraction the accidental coincidence events and the background events.

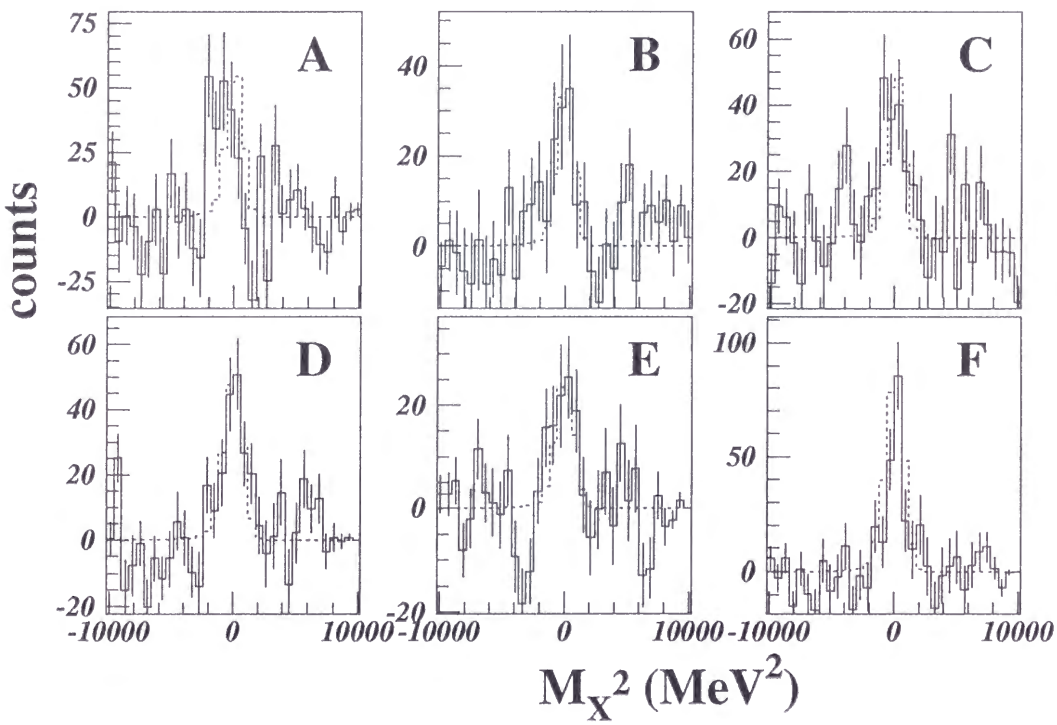

Figure 3.8: The squared missing mass ($M_X{}^2$) spectra reconstructed from the two observed proton momenta. The background events due to the accidental coincidence and (p,2p) reaction from the nuclei of the target container foils are subtracted. The dotted lines are the results of Monte Carlo simulations.

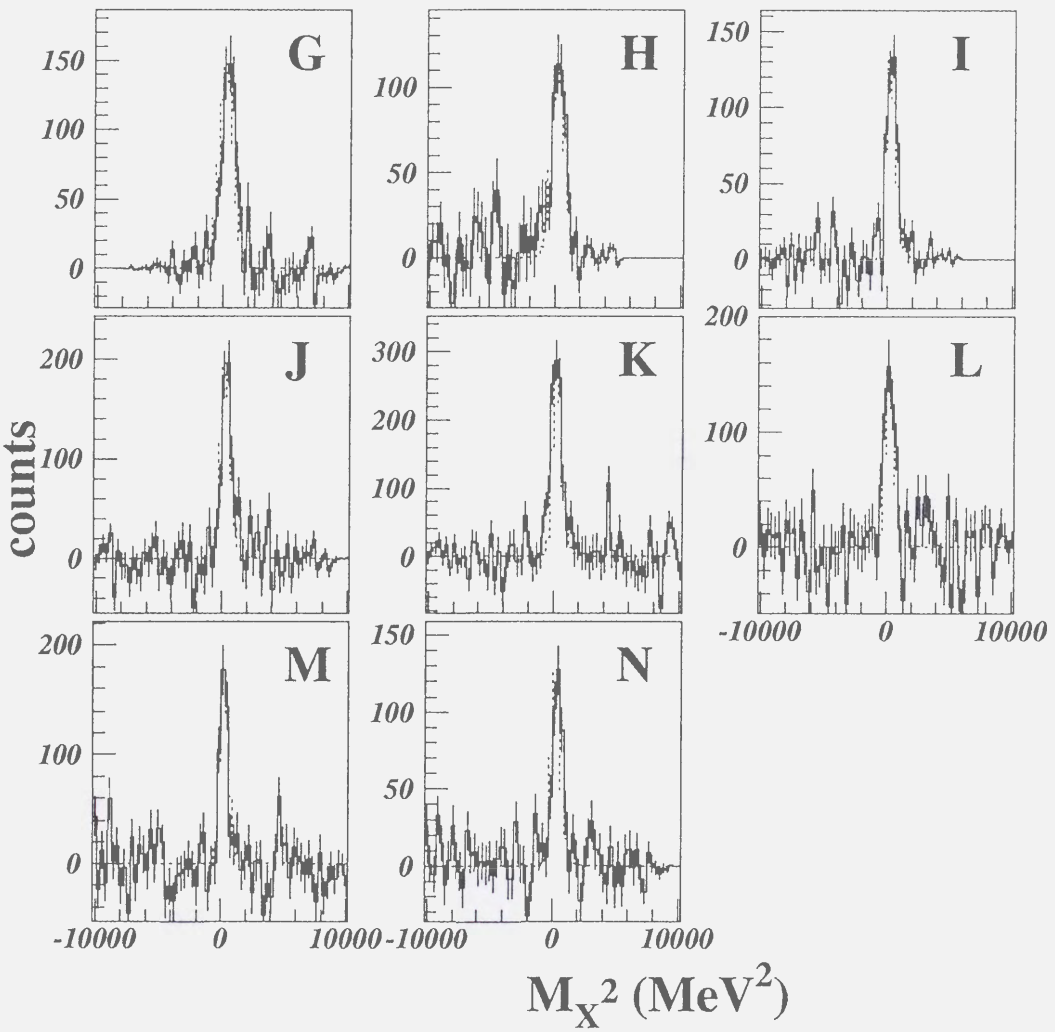

Figure 3.9: The squared missing mass ($M_X{}^2$) spectra. reconstructed from the two observed proton momenta. The background events due to the accidental coincidence and (p,2p) reaction from the nuclei of the target container foils are subtracted. The dotted lines are the results of Monte Carlo simulations.

Magnetic field setting	events in the gate
A	51.7 ± 36.7
B	-7.8 ± 24.0
C	62.5 ± 34.2
D	3.3 ± 23.0
E	13.0 ± 17.8
F	0.7 ± 24.6
G	64.5 ± 70.7
H	62.7 ± 58.2
I	-48.5 ± 66.4
J	-12.2 ± 83.6
K	63.5 ± 113.0
L	15.0 ± 98.1
M	-60.8 ± 84.1
N	57.1 ± 62.2
sum	264.6 ± 240.2

Table 3.3: Subtraction check.

mass spectra after subtracting the accidental coincidence and "empty target" events were used, and gates of $-5000 \leq M_X^2 \leq M_{X_{lower}}^2$ MeV^2 or $M_{X_{upper}}^2 \leq M_X^2 \leq 5000$ MeV^2 were applied for the above purpose, where $M_{X_{lower}}^2$ and $M_{X_{upper}}^2$ are lower and upper limits of the missing mass gate. The results are shown in Table 3.3. The events in the gates were consistent with 0 within 2σ and it shows that background events were correctly estimated.

3.11 Cross section

3.11.1 Coordinate system

Most of the theoretical calculations are performed at a coplanar geometry with infinitesimal acceptances. The experimental data include the non-coplanar events because of the finite geometrical acceptance of the detector. In the present analysis, we corrected the experimental data using a phase space calculation and obtained the $pp\gamma$ cross sections at a coplanar geometry with infinitesimal acceptances.

For the evaluation of the cross section, we consider two coordinate systems, which are the polar angle system and "horizontal-vertical" angle system (Fig. 3.10). In the following discussion, the z-axis is defined by the momentum of the beam and the detector is set on the x-z plane. An arbitrary point is expressed with three variables (r, θ, ϕ) for the polar angle system and (r, Θ, Φ) for the "horizontal-vertical" angle system. A point (x, y, z) in the Cartesian coordinate is expressed as,

$$\begin{aligned} x &= r\sin\theta\cos\phi \\ y &= r\sin\theta\sin\phi \\ z &= r\cos\theta \end{aligned} \tag{3.17}$$

for the polar angle system and

$$\begin{aligned} x &= r\cos\Phi\sin\Theta \\ y &= r\sin\Phi \\ z &= r\cos\Phi\cos\Theta \end{aligned} \tag{3.18}$$

for the "horizontal-vertical" angle system.

In the case of the coplanar geometry, the phase space of the "horizontal-vertical" angle system is the same as that of the polar angle system and we can use either coordinate system in the present analysis. Details are presented in Appendix A.3. In the present detector system, the GR and LAS, the resolution of the vertical angle or the azimuthal angle is not good. It is unavoidable that the non-coplanar event is detected by the present detector system. It is therefore preferable that the phase space of the non-coplanar event is not so much different from that of the coplanar event.

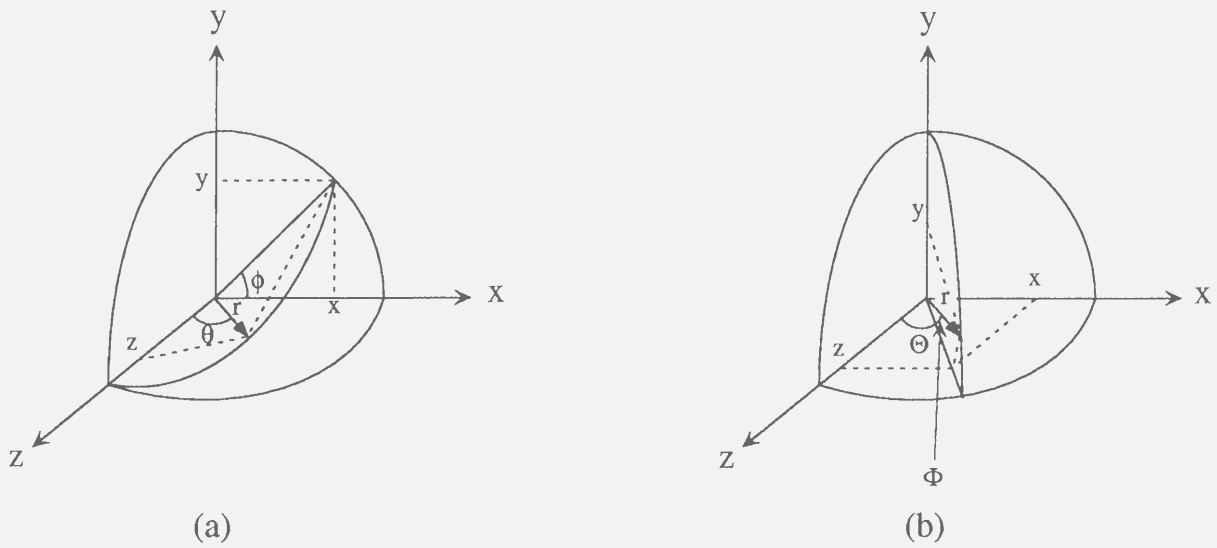

Figure 3.10: Definition of the two coordinate systems, the polar angle system (a) and "horizontal-vertical" angle system (b).

Figure 3.11 shows the $pp\gamma$ phase space as a function of the photon emission angle calculated with the polar angle system (a) and "horizontal-vertical" angle system (b). In this figure, Φ_{cop} indicates the noncoplanarity of the final protons, which is defined as a following expression [49].

$$\Phi_{cop} = \frac{1}{2}(\pi + \phi_1 - \phi_2) \tag{3.19}$$

Details for the phase space calculations are explained in Appendix A.

In the polar angle system, there are singularities at the forward and backward photon emission angles in the case of the non-coplanar geometry and the phase space vary dramatically around the singularities. In the "horizontal-vertical" angle system, there are no singularities and the variation of the phase space is small. Therefore the "horizontal-vertical" angle system was adopted in the present analysis to reduce the error due to the poor resolution of the proton vertical angle.

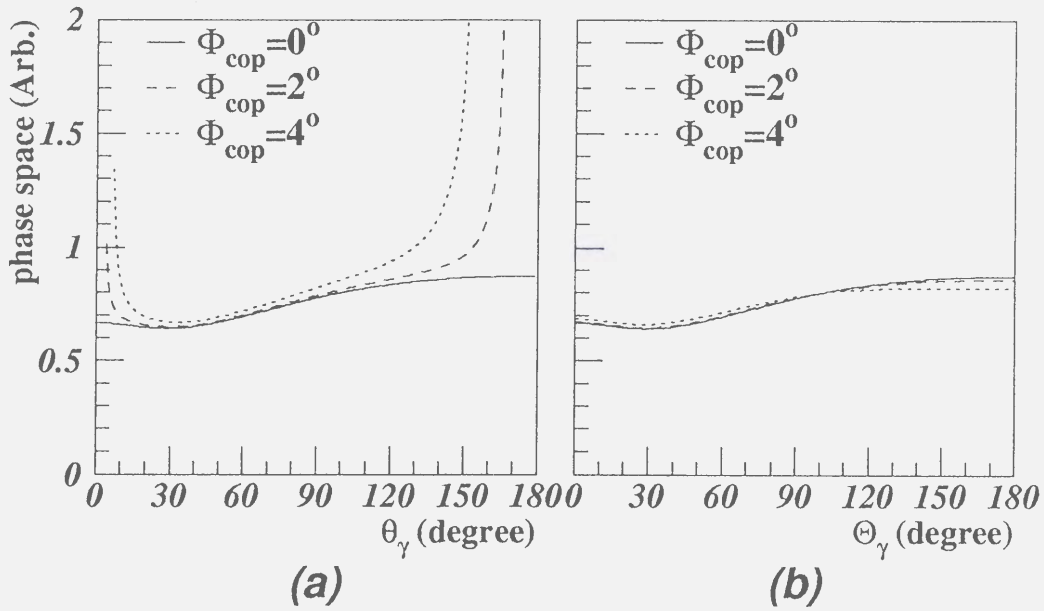

Figure 3.11: The $pp\gamma$ phase space as a function of the photon emission angle.

3.11.2 Evaluation of the cross section

The $pp\gamma$ cross sections were obtained at each magnetic field setting of the spectrometers, and then the weighted mean of all data was taken. The cross sections at the i-th magnetic field setting were evaluated with following expression,

$$\left(\frac{d^3\sigma}{d\Omega_1 d\Omega_2 d\theta_\gamma}(\theta_\gamma)\right)_i = \frac{\frac{Y^{\uparrow}_{true}(\theta_\gamma)-Y^{\uparrow}_{acc}(\theta_\gamma)-Y^{\uparrow}_{empty}(\theta_\gamma)}{\mathcal{L}^{\uparrow}p^{\uparrow}\epsilon^{\uparrow}} + \frac{Y^{\downarrow}_{true}(\theta_\gamma)-Y^{\downarrow}_{acc}(\theta_\gamma)-Y^{\downarrow}_{empty}(\theta_\gamma)}{\mathcal{L}^{\downarrow}(-p^{\downarrow})\epsilon^{\downarrow}}}{C_a(\theta_\gamma)C_0(\theta_\gamma)\left(\frac{1}{p^{\uparrow}}+\frac{1}{(-p^{\downarrow})}\right)\Delta\Omega_{GR}\Delta\Omega_{LAS}\Delta\theta_\gamma}, \quad (3.20)$$

$$\epsilon^{\uparrow(\downarrow)} = \epsilon^{\uparrow(\downarrow)}_{DAQ}\epsilon^{\uparrow(\downarrow)}_{VDC}, \quad (3.21)$$

where $Y^{\uparrow(\downarrow)}_{true}(\theta_\gamma)$, is the number of the events at the photon emission angle θ_γ in the "true" gate, $Y^{\uparrow(\downarrow)}_{acc}(\theta_\gamma)$ is the yield of the accidental coincidence, $Y^{\uparrow(\downarrow)}_{empty}(\theta_\gamma)$ is the yield of the background estimated with the "empty target" run, $C_a(\theta_\gamma)$ is the correction factor for the phase space due to the momentum acceptance of the spectrometers, $C_0(\theta_\gamma)$ is the correction factor for the finite geometrical acceptance of the spectrometer system evaluated with a phase space calculation, $p^{\uparrow(\downarrow)}$ is the beam polarization and the sign is defined as $p^{\uparrow} > 0$ and $p^{\downarrow} < 0$, $\epsilon^{\uparrow(\downarrow)}$ is the efficiency for the data acquisition system and VDC's, $\mathcal{L}^{\uparrow(\downarrow)}$ is the luminosity, $\Delta\Omega_{GR}$ and $\Delta\Omega_{LAS}$ are the solid angles of the GR and LAS, $\Delta\theta_\gamma$ is the bin size for the photon emission angle and 20° in the present analysis. Details for the $C_a(\theta_\gamma)$ and $C_0(\theta_\gamma)$ are described in Appendix B. Figure 3.12 shows the correction factor. It is less than 1% correction.

The yield of the accidental coincidence, $Y^{\uparrow(\downarrow)}_{acc}(\theta_\gamma)$, is estimated with following expression;

$$Y^{\uparrow(\downarrow)}_{acc}(\theta_\gamma) = \frac{N^{\uparrow(\downarrow)}_{acc}(\theta_\gamma)}{N_{bunch}}, \quad (3.22)$$

where $N^{\uparrow(\downarrow)}_{acc}(\theta_\gamma)$ is the number of events in the "accidental" gate and N_{bunch} is the number of the beam bunch in the "accidental" gate (Fig. 3.5). The value of the N_{bunch} is 3 or 4, which depends on the proton time of flight for each magnetic field setting. The yield of the background, $Y^{\uparrow(\downarrow)}_{empty}(\theta_\gamma)$, is normalized to the $Y^{\uparrow(\downarrow)}_{true}(\theta_\gamma)$ using the "Cave" BLP counts and the accidental coincidence events are subtracted by the same method as the liquid hydrogen target run. $C_a(\theta_\gamma)$ was obtained with phase space calculations. The details are described in Appendix B. $L^{\uparrow(\downarrow)}$ is evaluated with

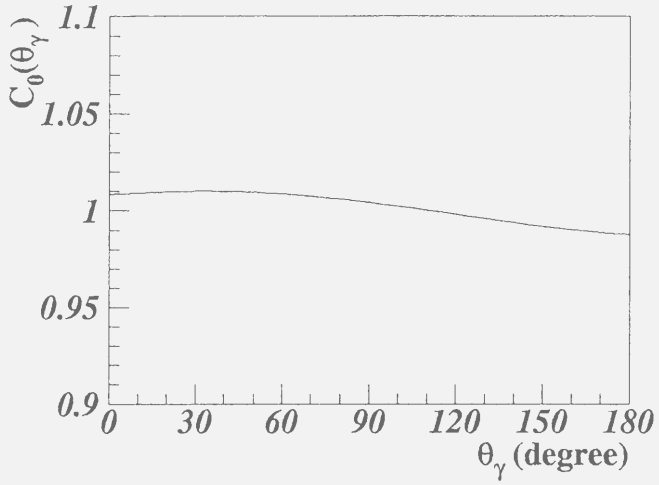

Figure 3.12: The correction factor for evaluating the cross section at a coplanar geometry with an infinitesimal geometrical acceptance. This is obtained with a phase space calculation.

the luminosity monitor using Eq. 3.12. The solid angles of the GR and LAS are estimated using

$$\Delta\Omega = \int_{-\Delta\Theta/2}^{\Delta\Theta/2} d\Theta \int_{-\Delta\Phi/2}^{\Delta\Phi/2} \cos\Phi d\Phi \tag{3.23}$$

where $\Delta\Theta$ is the horizontal angular acceptance which is defined with a software cut and $\Delta\Phi$ is the vertical angular acceptance which is limited with the slit. The $\Delta\Theta$ is 30 mrad for the GR and 120 mrad for the LAS. The $\Delta\Phi$ is 60 mrad for both of the GR and LAS. The uncertainties of the $\Delta\Theta$ are 0.73 mrad for the GR and 1.4 mrad for the LAS. These uncertainties cause the systematic errors of the solid angle, 3.5 % for the GR and 1.7 % for the LAS.

Figure 3.13 shows the cross sections obtained with the each magnetic field setting. The errors include statistical one and systematic one due to the uncertainty of the number of the $pp\gamma$ events and of the magnetic field of the spectrometer, which will be discussed later.

The $pp\gamma$ cross sections at a coplanar geometry with an infinitesimal geometrical

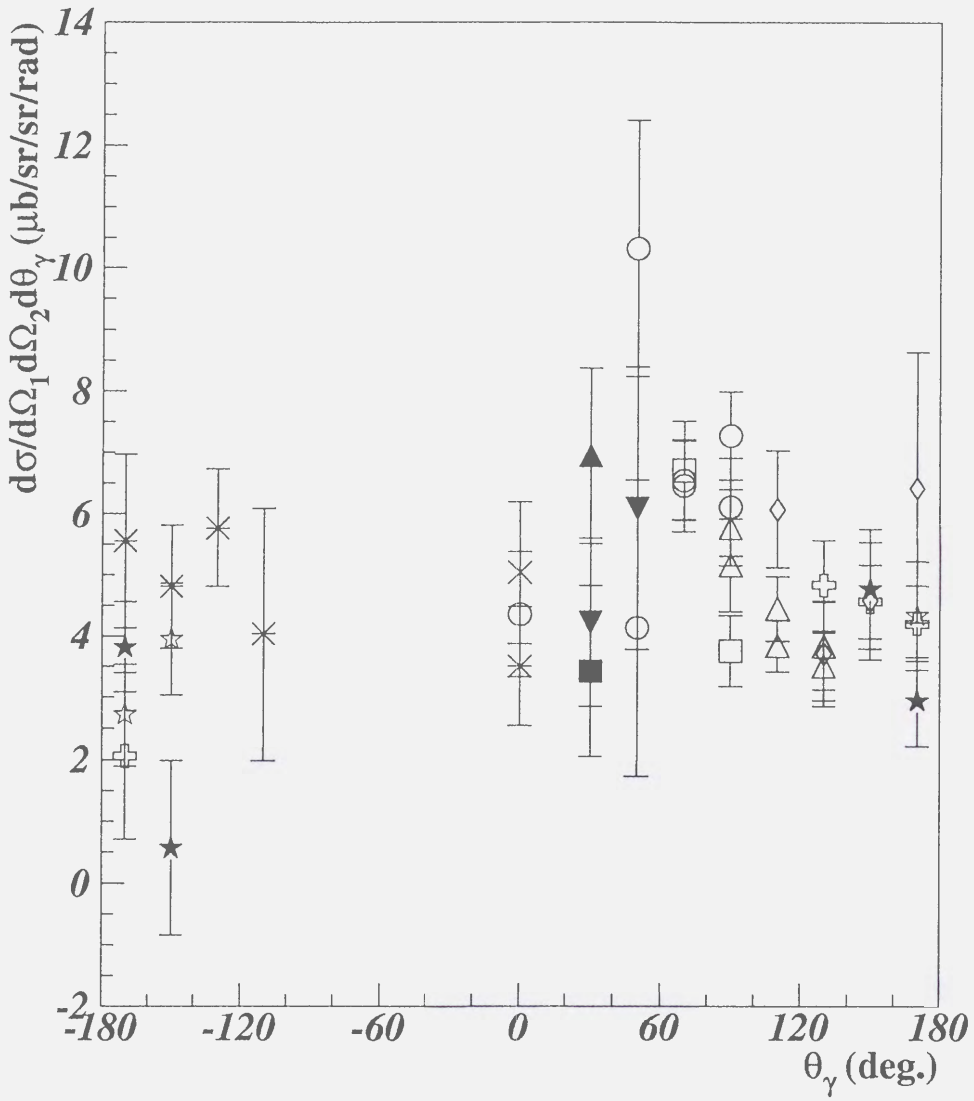

Figure 3.13: The $pp\gamma$ cross sections obtained with each magnetic field setting. The errors include statistical and systematic errors.

acceptance are evaluated with the expression as

$$\frac{d\sigma}{d\Omega_1 d\Omega_2 d\theta_\gamma}(\theta_\gamma) = \sum_i \frac{\left(\frac{d\sigma}{d\Omega_1 d\Omega_2 d\theta_\gamma}(\theta_\gamma)\right)_i / \Delta\left(\frac{d\sigma}{d\Omega_1 d\Omega_2 d\theta_\gamma}(\theta_\gamma)\right)_i^2}{1/\Delta\left(\frac{d\sigma}{d\Omega_1 d\Omega_2 d\theta_\gamma}(\theta_\gamma)\right)_i^2}, \tag{3.24}$$

where $\Delta\left(\frac{d\sigma}{d\Omega_1 d\Omega_2 d\theta_\gamma}(\theta_\gamma)\right)_i$ is an error of the $\left(\frac{d\sigma}{d\Omega_1 d\Omega_2 d\theta_\gamma}(\theta_\gamma)\right)_i$.

3.11.3 Systematic error for the cross section

We studied the sensitivity of the $pp\gamma$ cross section to systematic errors in the measured proton momentum vectors. Figure 3.14 shows the relative magnitude of the cross section estimated with Monte Carlo Simulations when various systematic errors are introduced. The errors taken into account in this figure are as follows,

- The vertical angles of the protons, which is set to be 0 degree (Sec. 3.7),
- The energy straggling and the multiple scattering in the liquid hydrogen target,
- The uncertainty of the detected proton momentum, 0.1%,

The uncertainty of the detected proton momentum is due to the drift of the magnetic field of the spectrometer, which is less than $\pm 0.1\%$. The effects of the errors of the proton vertical angles and the errors of the correction for the energy loss are included in Fig. 3.14(a). Figure 3.14(b) gives the results for $+0.1\%$ drift of the magnetic field of the spectrometers in addition to the errors included in Fig. 3.14(a). The error of the detected proton momentum affects the phase space correction factor $C_a(\theta_\gamma)$. The errors were estimated with the Monte Carlo simulations when the momenta of the detected protons were shifted by $\pm 0.1\%$ and included in the $\Delta\left(\frac{d\sigma}{d\Omega_1 d\Omega_2 d\theta_\gamma}(\theta_\gamma)\right)_i$ in the Eq. (3.24).

The systematic error due to the uncertainty of the missing mass gate width was taken into account, as described in Sec. 3.10. The uncertainty for each magnetic field setting is $2 - 17\%$, and it is smaller than the statistical error.

The systematic errors for the absolute normalization are listed in Table 3.4. The systematic error for the overall absolute normalization is obtained by taking a quadratic sum of them and is 5.9%.

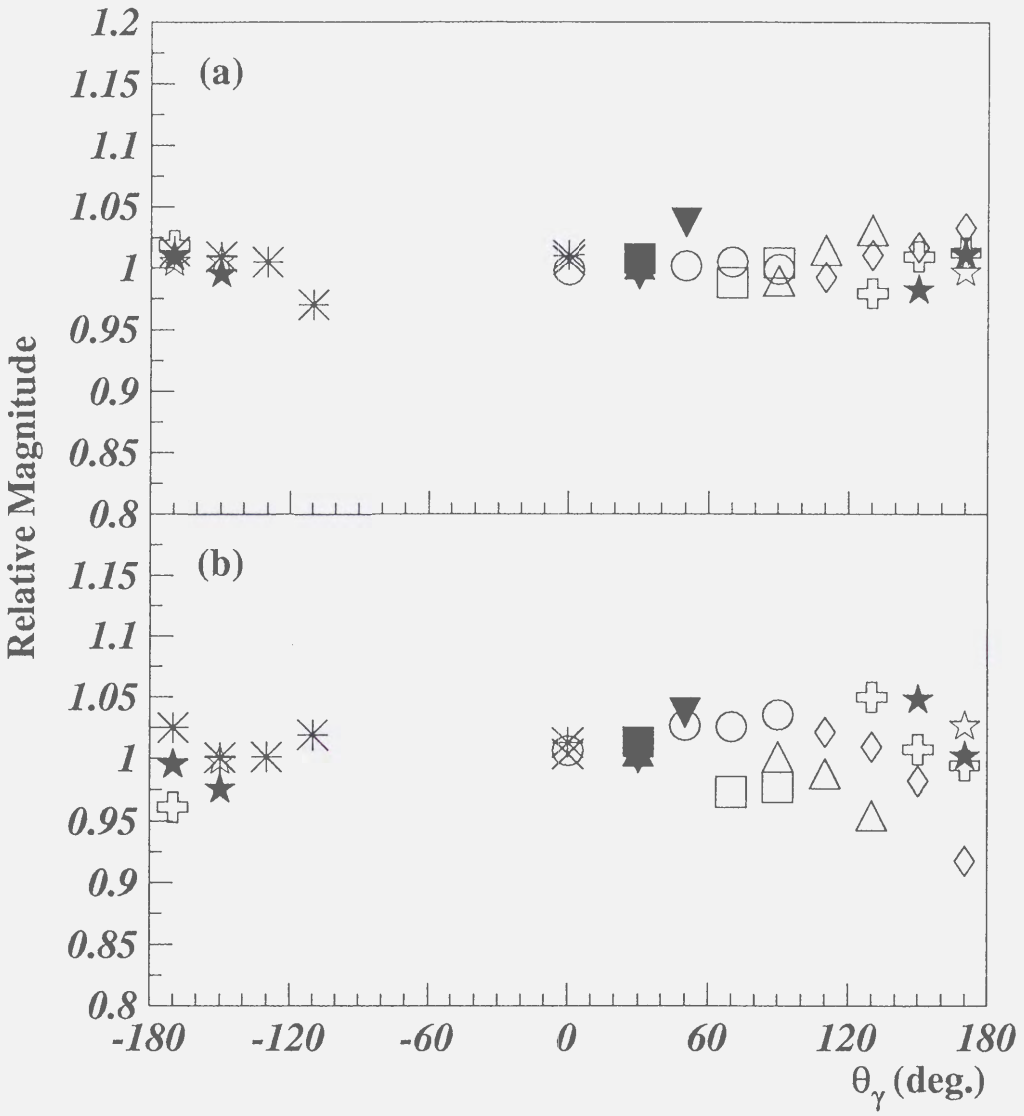

Figure 3.14: The effect due to the vertical angle errors, errors of the energy loss correction, and detected proton momentum with Monte Carlo simulations. (a): The effect of the vertical angle and the energy straggling and the multiple scattering in the liquid hydrogen target. (b): The effect when the momenta of the outgoing protons were shifted by 0.1% in addition to the effect included in (a).

content	error (%)
luminosity	4.4
GR solid angle	3.5
LAS solid angle	1.7
total	5.9

Table 3.4: Systematic errors for the absolute normalization.

The relative error of the luminosity is evaluated by a fluctuation of the ratio between the LM counts and the "Cave"-BLP counts as discussed in Sec. 3.4, and it is 0.6%.

3.12 Analyzing power

3.12.1 Evaluation of the analyzing power

We consider the case that the incoming proton goes on the z axis and the photon is emitted in the x-z plane (Fig. 3.15). In the case of the beam polarization of $p^{\uparrow} = -p^{\downarrow} = p$, the analyzing power for the $pp\gamma$ reaction is defined by

$$A_y = \frac{1}{p}\frac{d\sigma^{\uparrow} - d\sigma^{\downarrow}}{d\sigma^{\uparrow} + d\sigma^{\downarrow}}, \tag{3.25}$$

where $d\sigma^{\uparrow(\downarrow)}$ is the differential cross section for the incoming proton with spin in the $+(-)y$-direction.

In the present analysis, the photon emission angle, θ_γ is defined as an angle between the z axis and the photon momentum vector and evaluated to the $-x$ direction as shown in Fig. 3.16. The relations between the analyzing power and the yield are described as,

$$\begin{aligned} Y^{\uparrow}_{true}(\theta_\gamma) - Y^{\uparrow}_{acc}(\theta_\gamma) - Y^{\uparrow}_{empty}(\theta_\gamma) &= d\sigma_0 \mathcal{L}^{\uparrow} \Delta\Omega_{GR} \Delta\Omega_{LAS} \Delta\theta_\gamma (1 - p^{\uparrow} A_y(\theta_\gamma)), \\ Y^{\downarrow}_{true}(\theta_\gamma) - Y^{\downarrow}_{acc}(\theta_\gamma) - Y^{\downarrow}_{empty}(\theta_\gamma) &= d\sigma_0 \mathcal{L}^{\downarrow} \Delta\Omega_{GR} \Delta\Omega_{LAS} \Delta\theta_\gamma (1 - p^{\downarrow} A_y(\theta_\gamma)), \end{aligned} \tag{3.26}$$

where $d\sigma_0$ is the unpolarized cross section, and the sign of the $p^{\uparrow(\downarrow)}$ is defined as $p^{\uparrow} > 0$ and $p^{\downarrow} < 0$. The analyzing powers at the i-th magnetic field setting were evaluated

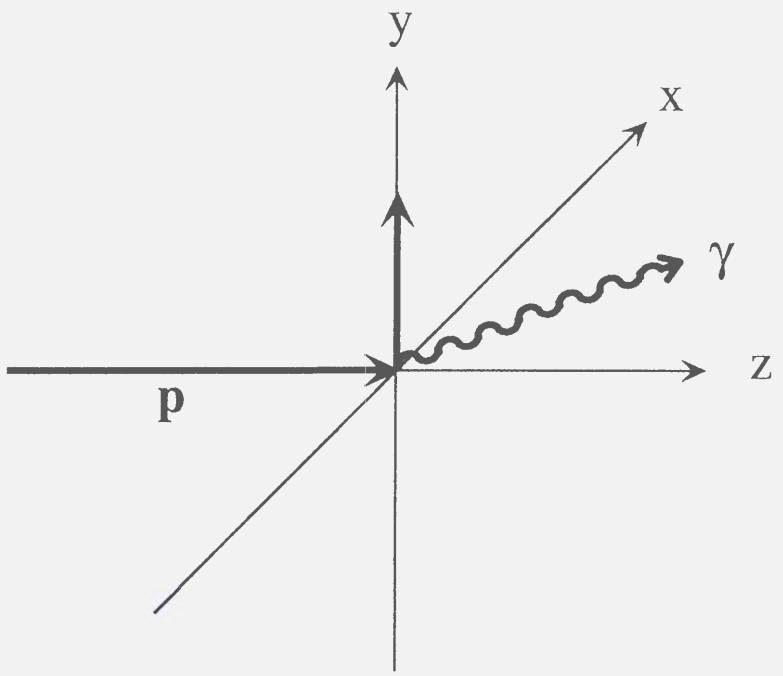

Figure 3.15: Definition of the direction of the polarization.

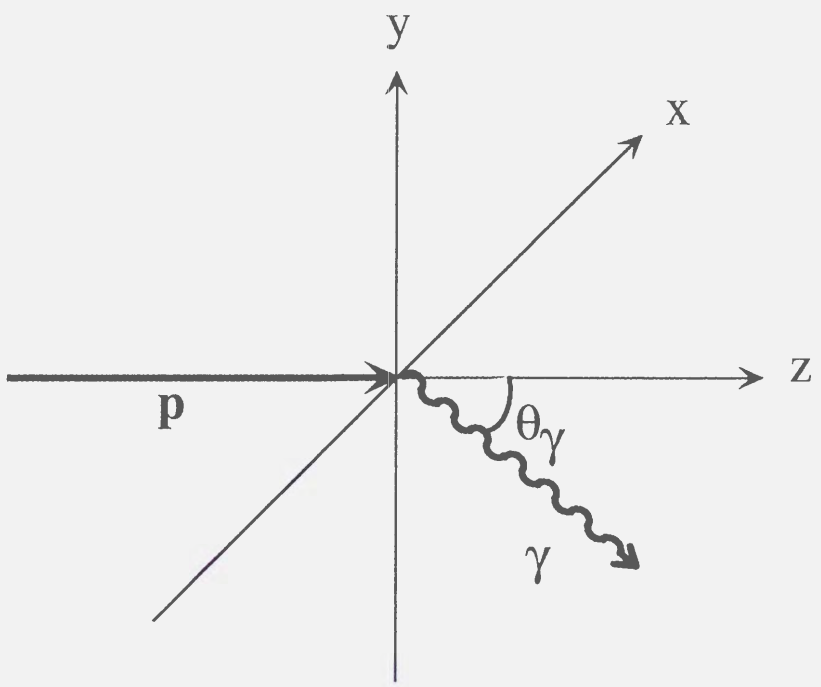

Figure 3.16: Definition of the photon emission angle in the present analysis.

from Eq. (3.26). The expression is

$$
\begin{aligned}
(A_y(\theta_\gamma))_i &= -\frac{1-\alpha(\theta_\gamma)}{(-p^\downarrow)+p^\uparrow\alpha(\theta_\gamma)}, \\
\alpha(\theta_\gamma) &= \frac{\frac{Y^\downarrow_{true}(\theta_\gamma)-Y^\downarrow_{acc}(\theta_\gamma)-Y^\downarrow_{empty}(\theta_\gamma)}{\mathcal{L}^\downarrow\epsilon^\downarrow}}{\frac{Y^\uparrow_{true}(\theta_\gamma)-Y^\uparrow_{acc}(\theta_\gamma)-Y^\uparrow_{empty}(\theta_\gamma)}{\mathcal{L}^\uparrow\epsilon^\uparrow}}.
\end{aligned}
\tag{3.27}
$$

The analyzing powers obtained with each magnetic field setting are shown in Fig. 3.17. The errors in Fig. 3.17 include the statistical and systematic ones discussed later.

The analyzing powers for the $pp\gamma$ reaction are evaluated by taking the weighted means of the all data using the following expression,

$$
A_y(\theta_\gamma) = \sum_i \frac{(A_y(\theta_\gamma))_i / \Delta\left(A_y(\theta_\gamma)\right)_i^2}{1/\Delta\left(A_y(\theta_\gamma)\right)_i^2}, \tag{3.28}
$$

where $\Delta\left(A_y(\theta_\gamma)\right)_i$ is an statistical error of $(A_y(\theta_\gamma))_i$.

3.12.2 Systematic error for the analyzing power

The systematic error due to the uncertainty of the number of the $pp\gamma$ events was taken into account. The uncertainty was derived from varying the width of the missing mass gate of $\pm 20\%$, as described in Sec. 3.10, and it was smaller than the statistical error.

One of the systematic errors for the analyzing powers is due to the uncertainty of the effective analyzing power of the "WN"-BLP. The effective analyzing power is 0.45 ± 0.01, and the error causes the systematic error for the $pp\gamma$ analyzing power of 2.2%.

3.13 Proton-proton elastic scattering

In order to verify the absolute normalization of the cross section with the present measurement, we performed the measurements of the pp elastic scattering with the CH_2 target and the liquid hydrogen target. We took the GR single measurement, the LAS single measurement, and the GR and LAS coincidence measurement.

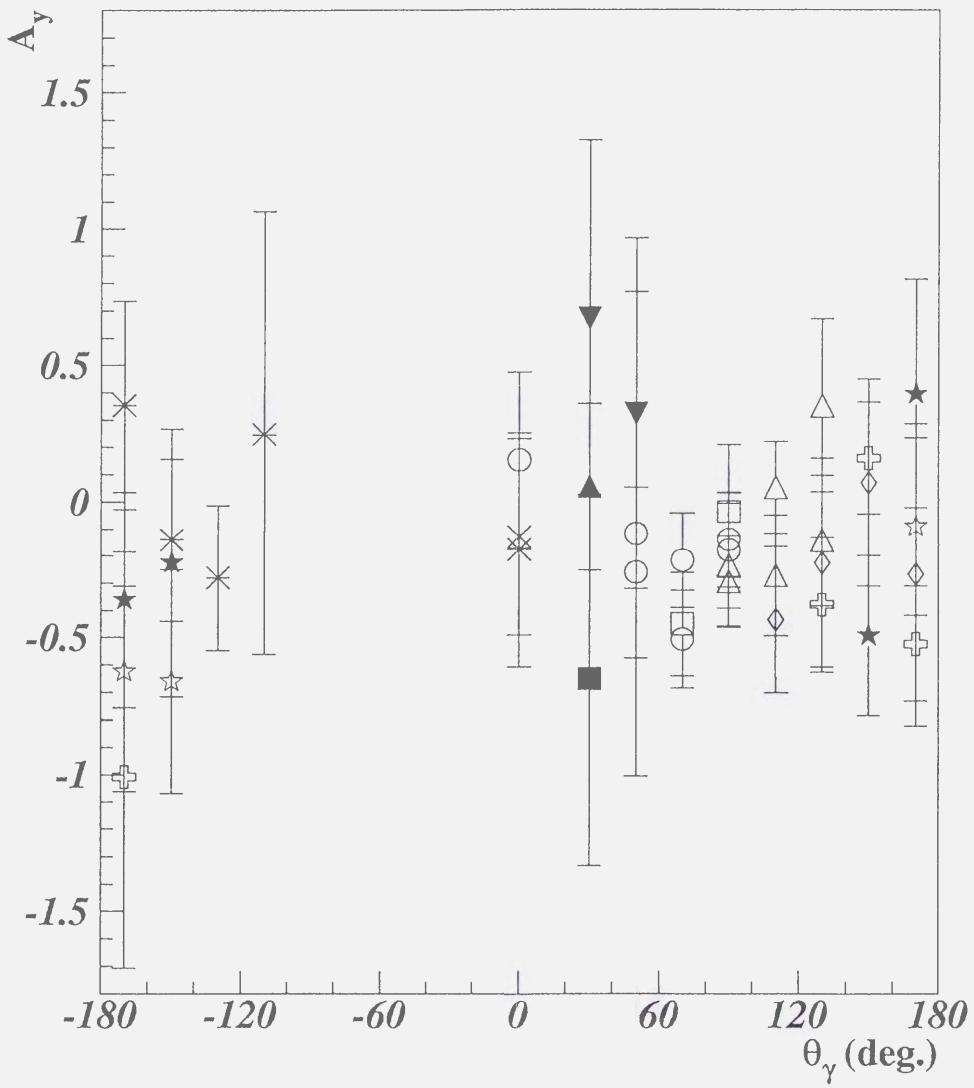

Figure 3.17: The analyzing powers for the $pp\gamma$ reaction obtained with the each magnetic field setting. The errors include statistical and systematic ones.

3.13.1 Single-arm measurement with CH_2 target

The differential cross section and analyzing power are evaluated with the following expressions

$$\frac{d\sigma}{d\Omega}(\theta) = \frac{\frac{Y^{\uparrow}_{CH_2}(\theta)-Y^{\uparrow}_{C}(\theta)}{N_t N_b^{\uparrow} p^{\uparrow}\epsilon^{\uparrow}} - \frac{Y^{\downarrow}_{CH_2}(\theta)-Y^{\downarrow}_{C}(\theta)}{N_t N_b^{\downarrow} p^{\downarrow}\epsilon^{\downarrow}}}{(\frac{1}{p^{\uparrow}} - \frac{1}{p^{\downarrow}})\Delta\Omega}, \tag{3.29}$$

$$\epsilon^{\uparrow(\downarrow)} = \epsilon^{\uparrow(\downarrow)}_{DAQ}\epsilon^{\uparrow(\downarrow)}_{VDC}, \tag{3.30}$$

$$A_y(\theta) = \frac{1-\alpha(\theta)}{-p^{\downarrow}+p^{\uparrow}\alpha(\theta)}$$

$$\alpha(\theta) = \frac{\frac{Y^{\downarrow}_{CH_2}(\theta)-Y^{\downarrow}_{C}(\theta)}{L^{\downarrow}\epsilon^{\downarrow}}}{\frac{Y^{\uparrow}_{CH_2}(\theta)-Y^{\uparrow}_{C}(\theta)}{L^{\uparrow}\epsilon^{\uparrow}}}, \tag{3.31}$$

where $Y^{\uparrow(\downarrow)}_{CH_2}(\theta)$ is the yield including the contribution of the hydrogen and the carbon in the CH_2 target, $Y^{\uparrow(\downarrow)}_{C}(\theta)$ including the contribution of the carbon only. The solid angle ,$\Delta\Omega$, is evaluated with Eq. 3.23, where a bin size of the horizontal angle, $\Delta\Theta$, is 15 mrad for the GR and 20 mrad for the LAS. The number of protons in the beam is $N_b^{\uparrow(\downarrow)}$, which is measured with the "Cave" BLP, and N_t is the number of protons in the CH_2 target. The $Y^{\uparrow(\downarrow)}_{CH_2}(\theta)$ is evaluated from the proton momentum spectrum with the gate of the horizontal angle, and the $Y^{\uparrow(\downarrow)}_{C}(\theta)$ is evaluated from the same proton momentum spectrum which includes no *pp* elastic scattering events. Figure 3.18 shows the proton momentum spectrum measured with the GR. The yield from the carbon in the CH_2 target is estimated from the hatched area in the Fig. 3.18.

3.13.2 Coincidence measurement with CH_2 target

In the coincidence measurement of the *pp* elastic scattering with the GR and LAS, the additional slit for the LAS was not set in order to define the geometrical acceptance by the GR. Figure 3.19 shows the proton momentum spectrum measured with the GR. The background from the carbon in the CH_2 target is less than 0.5% which was estimated with the same method as the GR single-arm measurement, and is not considered in this analysis.

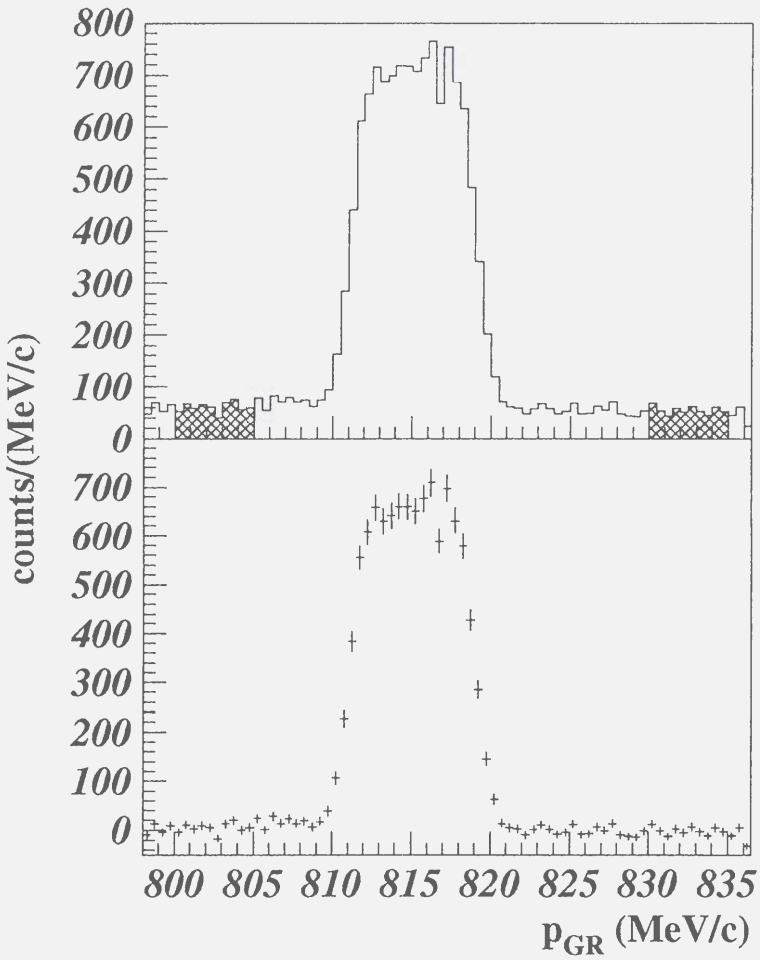

Figure 3.18: The proton momentum spectrum with the CH_2 target measured with the GR at θ_{GR} =25.6°. Upper figure : The contribution from the carbon in the CH_2 target is estimated from the hatched area. Lower figure : After subtraction of the background events due to the carbon target.

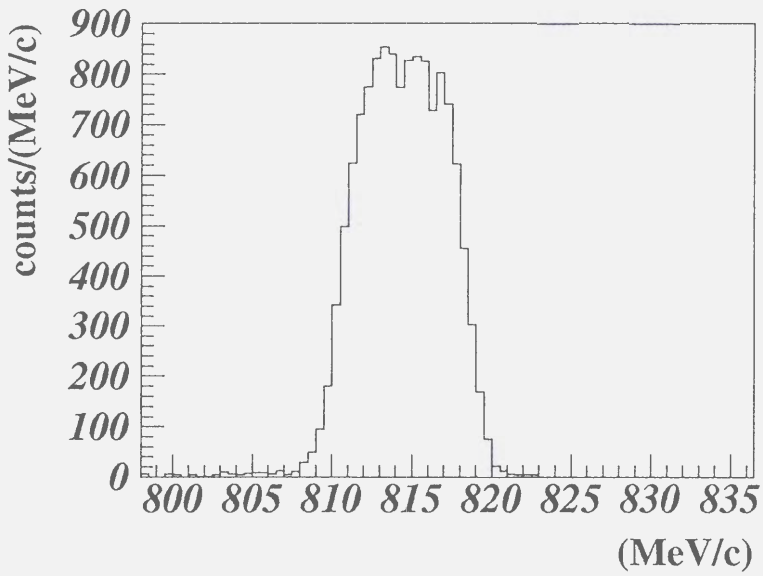

Figure 3.19: The proton momentum spectrum measured with the GR at θ_{GR} =25.6° with the CH_2 target. This was obtained with the coincidence measurement of the GR and LAS.

content	error (%)
beam current	2.4
target thickness	2.2
GR solid angle	3.5
LAS solid angle	1.7
GR total	4.8
LAS total	3.7

Table 3.5: Systematic errors for the cross section

3.13.3 Systematic error

The systematic errors for the cross section are listed in Table 3.5. The systematic errors are evaluated by taking quadratic sum of these errors, and they are 4.8% for the GR single-arm measurement and 3.7% for the LAS single-arm measurement. In the GR-LAS coincidence measurement, the solid angle was defined by the GR, and the systematic error is 4.8%.

The systematic errors for the analyzing powers are due to the uncertainty of the effective analyzing power of the "WN"-BLP. The effective analyzing power for the "WN"-BLP is 0.45 ± 0.01, and the error causes the systematic error of 2.2%.

Chapter 4

Experimental Result

4.1 Cross section

The triple differential cross sections $\frac{d\sigma}{d\Omega_1 d\Omega_2 d\theta_\gamma}$ for the $pp\gamma$ reaction are shown in Fig. 4.1. The error bars represent the quadratic sum of the statistical and systematic errors which are due to the uncertainties of the missing mass gate width, of the relative normalization, of the magnetic field of the spectrometer, and of the vertical angle of the detected protons, and the effects of the energy straggling and the multiple scattering in the liquid hydrogen target. The systematic error for the overall normalization of 5.9% is not included. The solid and dashed lines show the results of the theoretical calculations including the contribution of the Δ current and the dotted line shows the result of the calculations without the Δ current. Details are described in Chap. 5.

4.2 Analyzing power

Figure 4.2 shows the analyzing powers for the $pp\gamma$ reaction. The error bars represent the quadratic sum of the statistical and systematic errors due to the uncertainties of the missing mass gate width. The systematic error of 2.2%, which is due to the uncertainty of the effective analyzing power of the "WN"-BLP, is not included. The solid and dashed lines show the results of the theoretical calculations including the contribution of the Δ current and the dotted line shows the result of the calculations without the Δ current. Details are described in Chap. 5.

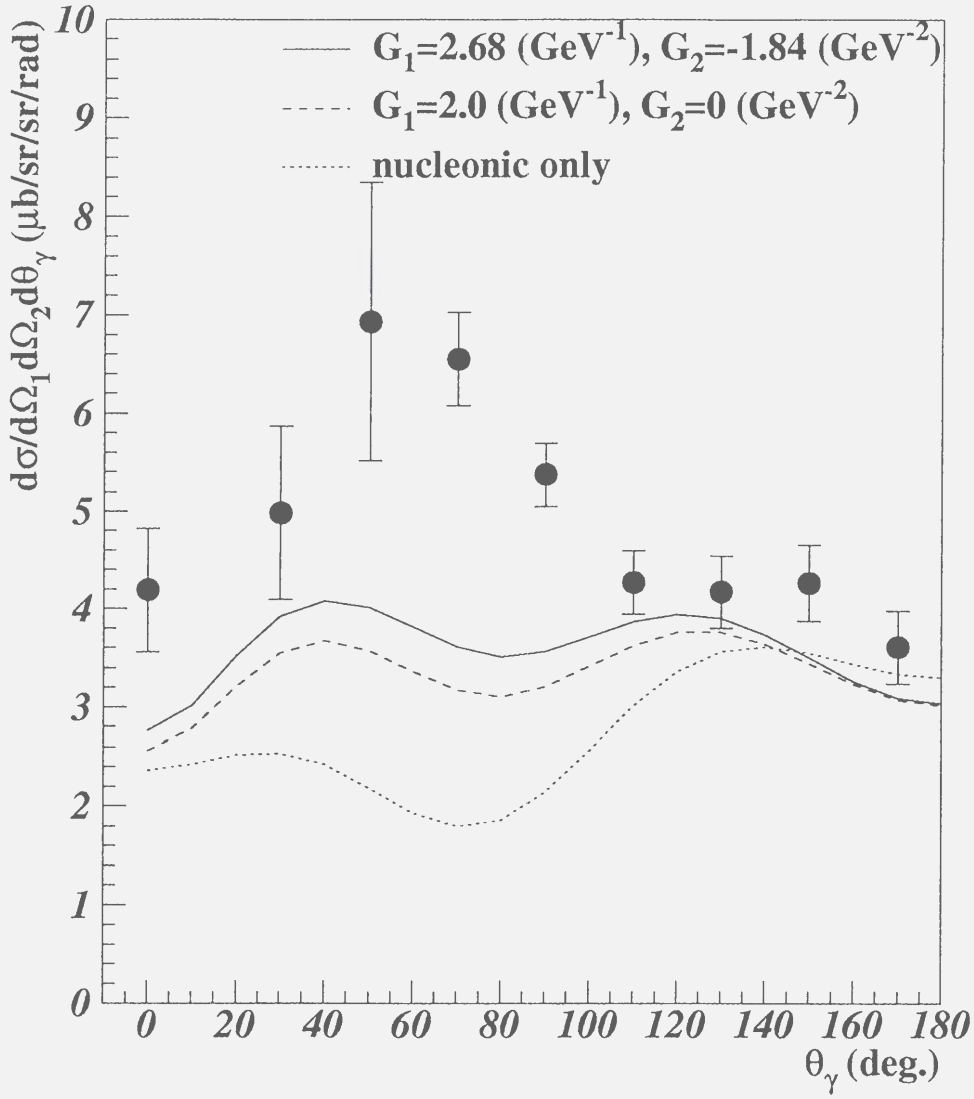

Figure 4.1: The differential cross section for the $pp\gamma$ in the laboratory system. The lines are the result of the theoretical calculations (see text).

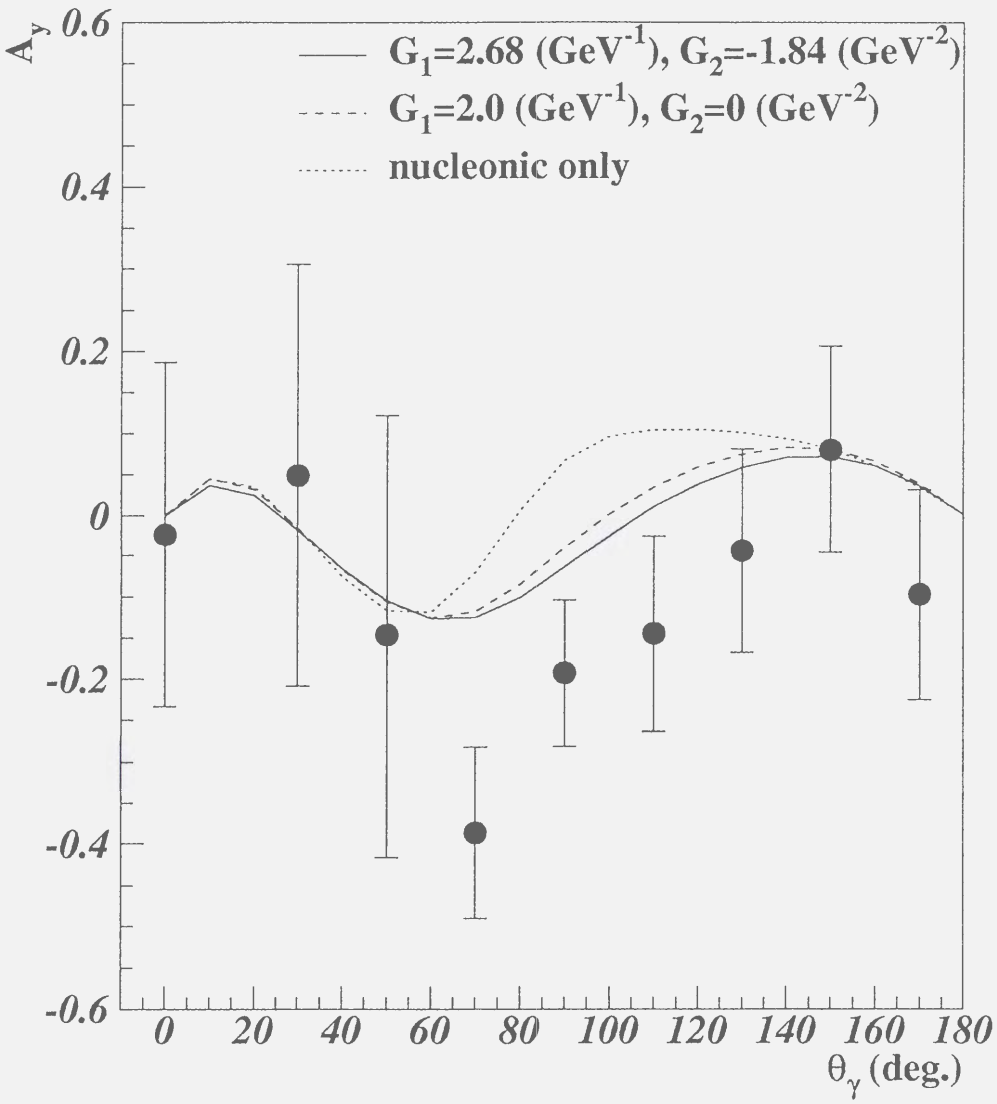

Figure 4.2: The analyzing powers for the $pp\gamma$. The lines are the result of the theoretical calculations.

4.3 Proton-proton elastic scattering

Differential cross sections and analyzing powers for the *pp* elastic scattering are shown in Fig. 4.3 and Fig. 4.4. The results of the GR single arm measurement, the LAS single arm measurement, and the coincidence measurement of the GR and LAS are presented. The error bars represent quadratic sums of statistical and systematic errors discussed in Sec. 3.13. The solid lines show the result of the *SAID* program [47].

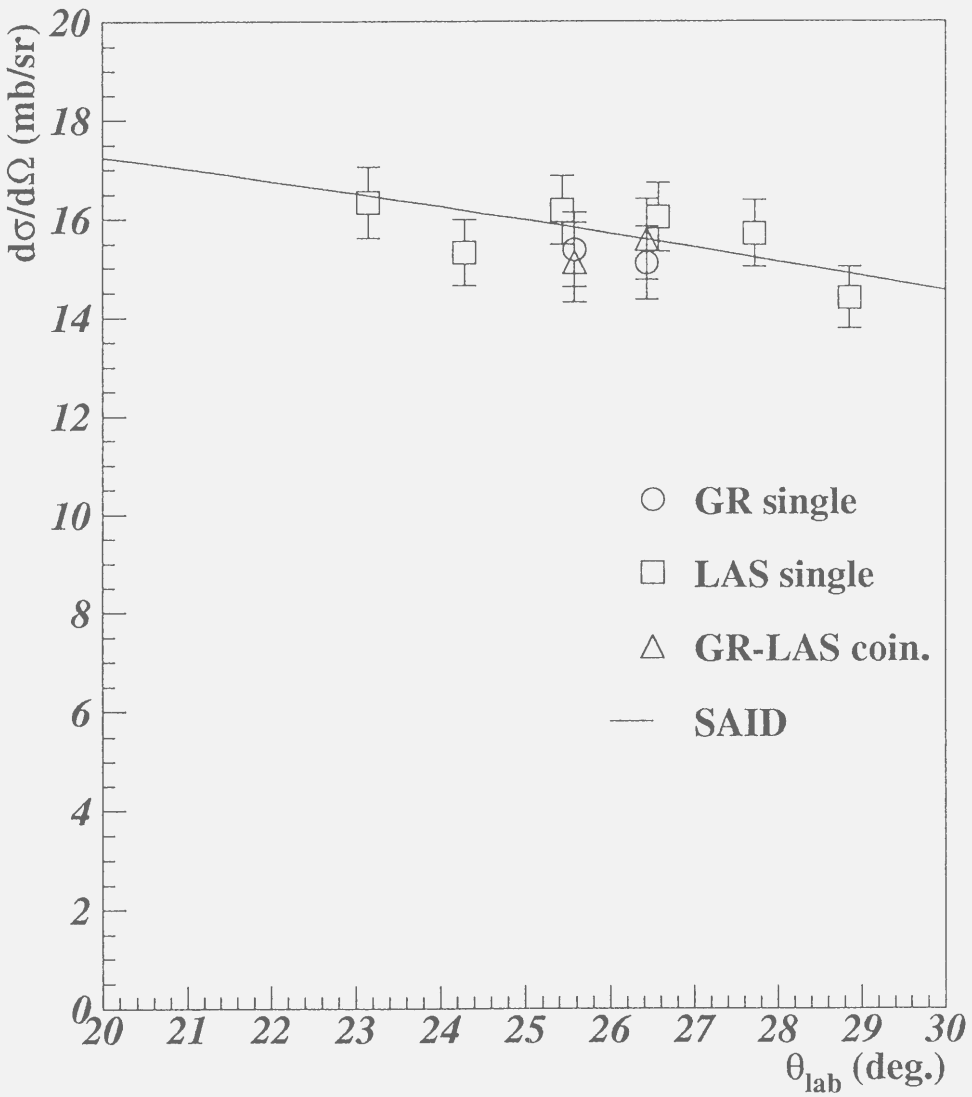

Figure 4.3: The differential cross section for the pp elastic scattering. The solid line shows the result of the *SAID* program.

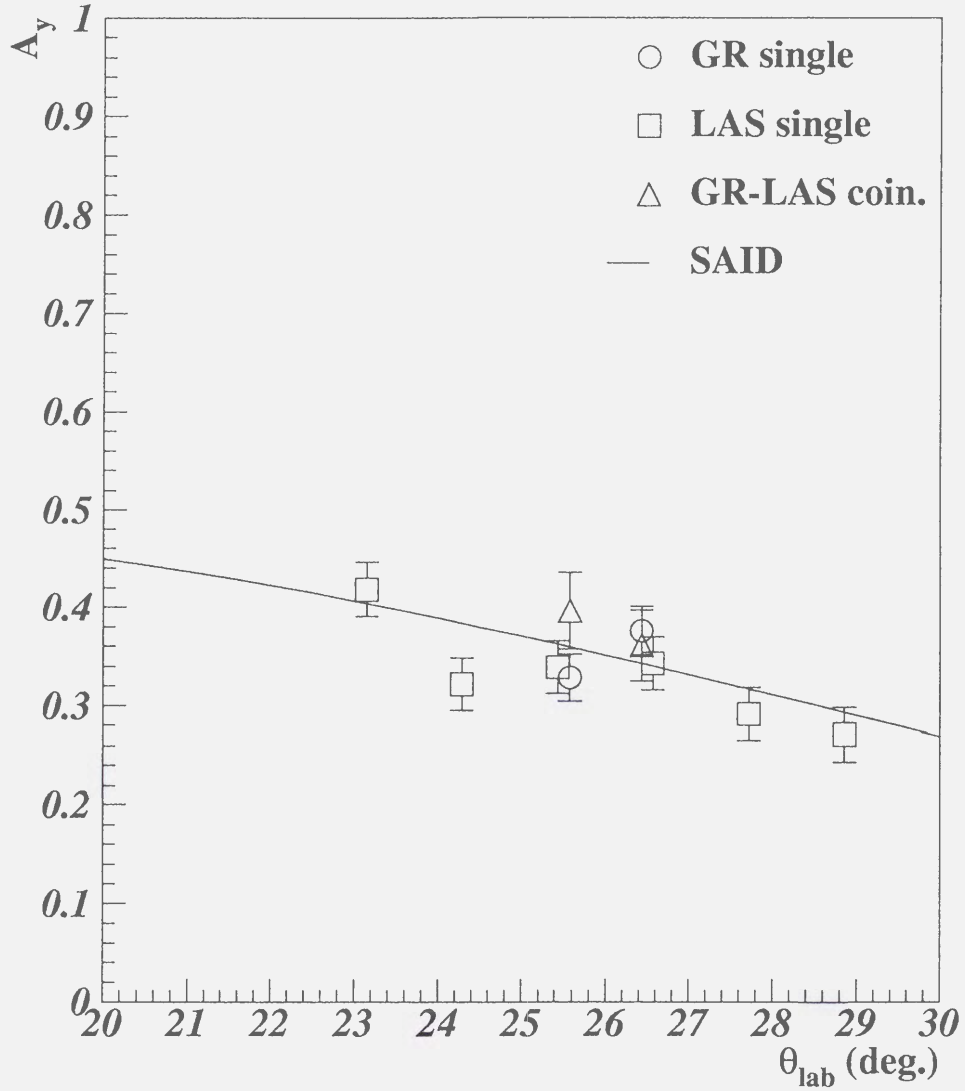

Figure 4.4: The analyzing power for the pp elastic scattering. The solid line shows the result of the *SAID* program.

Chapter 5

Discussion

5.1 Kinematical condition

In this section, we discuss kinematical variables such as the photon energy and the proton-photon invariant mass, and we choose kinematical conditions that are suitable for investigating the higher order term. The effects of the off-shell and the Δ current increase as the photon energy increases, as discussed in Appendix D. In the picture that the photon is created by the electromagnetic decay of the Δ which is generated by the proton-proton collision, the proton-photon invariant mass indicates the Δ mass. Therefore the contribution from the Δ current is thought to increase as the invariant mass reaches near the Δ mass.

Figure 5.1 shows the maximum photon energy in the center of mass system of the initial two protons and the maximum proton-photon invariant mass as a function of the incident energy. They are calculated with

$$E_{\gamma CM}^{max} = \frac{s-4m^2}{2\sqrt{s}} = \frac{mT_0}{\sqrt{2m(2m+T_0)}}, \tag{5.1}$$

$$M_{p-\gamma}^{max} = \sqrt{s}-m = \sqrt{2m(2m+T_0)}-m, \tag{5.2}$$

where T_0 is the kinetic energy of the incident proton and $\sqrt{s}$ is the total energy in the center of mass system. The photon energy and proton-photon invariant mass increase almost linearly as the incident energy increases. In the energy region above 300 MeV, the photon energy is high and beyond the validity of the classical theory. The proton-photon invariant mass is far below the Δ mass ($M_\Delta \approx 1232$ MeV, $\Gamma_\Delta \approx 120$ MeV).

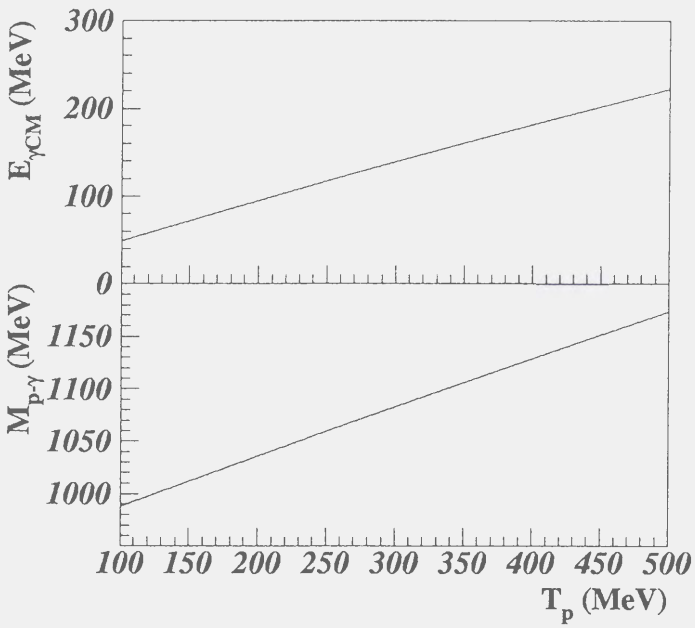

Figure 5.1: The maximum photon energy and proton-photon invariant mass as a function of the incident energy.

The proton angle dependencies of the photon energy and proton-photon invariant mass are shown in Fig. 5.2. The incident energy is 389.3 MeV and the photon emission angle is 0 degree. The two protons are scattered at a same angle. The photon energy and proton-photon invariant mass increase as the proton angle becomes small. The changes of the photon energy and invariant mass are small at $\theta_p \leq 30°$. The photon energy and invariant mass are about 180 MeV and 1120 MeV at $\theta_p = 0°$, and 150 MeV and 1090 MeV at $\theta_p = 26°$. The photon energy and proton-photon invariant mass at $\theta_p = 26°$ corresponds to that at about $T_p = 325$ MeV and $\theta_p = 0°$.

In general, the cross section is written by the following form,

$$\frac{d\sigma}{dX} = \frac{1}{F}\mathcal{J}|\mathcal{M}|^2 \tag{5.3}$$

where X shows the kinematical variables, F is a flux factor, $\mathcal{J}$ is a phase space factor and $\mathcal{M}$ is a matrix element. The physical interests are appeared in $\mathcal{M}$. In order to investigate the matrix element through the cross section, it is preferable that the change of the phase space factor $\mathcal{J}$ is small in the measured kinematical condition [19]. Figure 5.3 shows the phase space factor $\mathcal{J}$ as a function of the photon emission

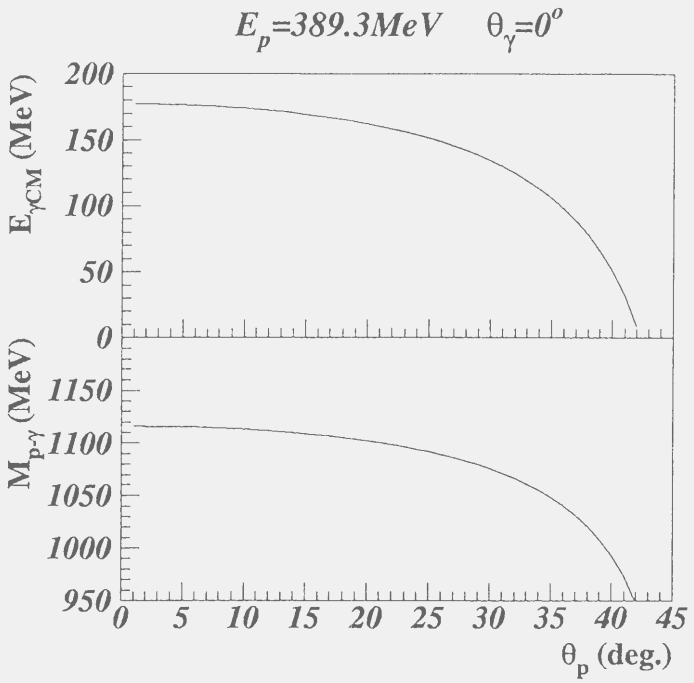

Figure 5.2: The photon energy and proton-photon invariant mass as a function of the proton angle.

angle in addition to the photon energy and proton-photon invariant mass. In the case of $\theta_1 = \theta_2 = 26°$, which is the present condition, the phase space factor $\mathcal{J}$ is almost flat and the cross section is sensitive to the matrix element. In the case of $\theta_1 = \theta_2 = 10°$, $\mathcal{J}$ varies largely, and the cross section reflects the phase space factor and is not sensitive to the matrix element. The analyzing powers are not affected by the phase space factor $\mathcal{J}$ and it has advantage to measure the analyzing powers at small proton angle.

From the above discussions, it is shown that the kinematical condition in the present measurement is suitable especially for the cross section measurement. In the next section, we compare the present data with the recent theoretical calculations.

5.2 Comparison with potential model calculation

The $pp\gamma$ differential cross sections and analyzing powers of the present work were compared to the theoretical calculation of de Jong *et al.* [20]. They include the pro-

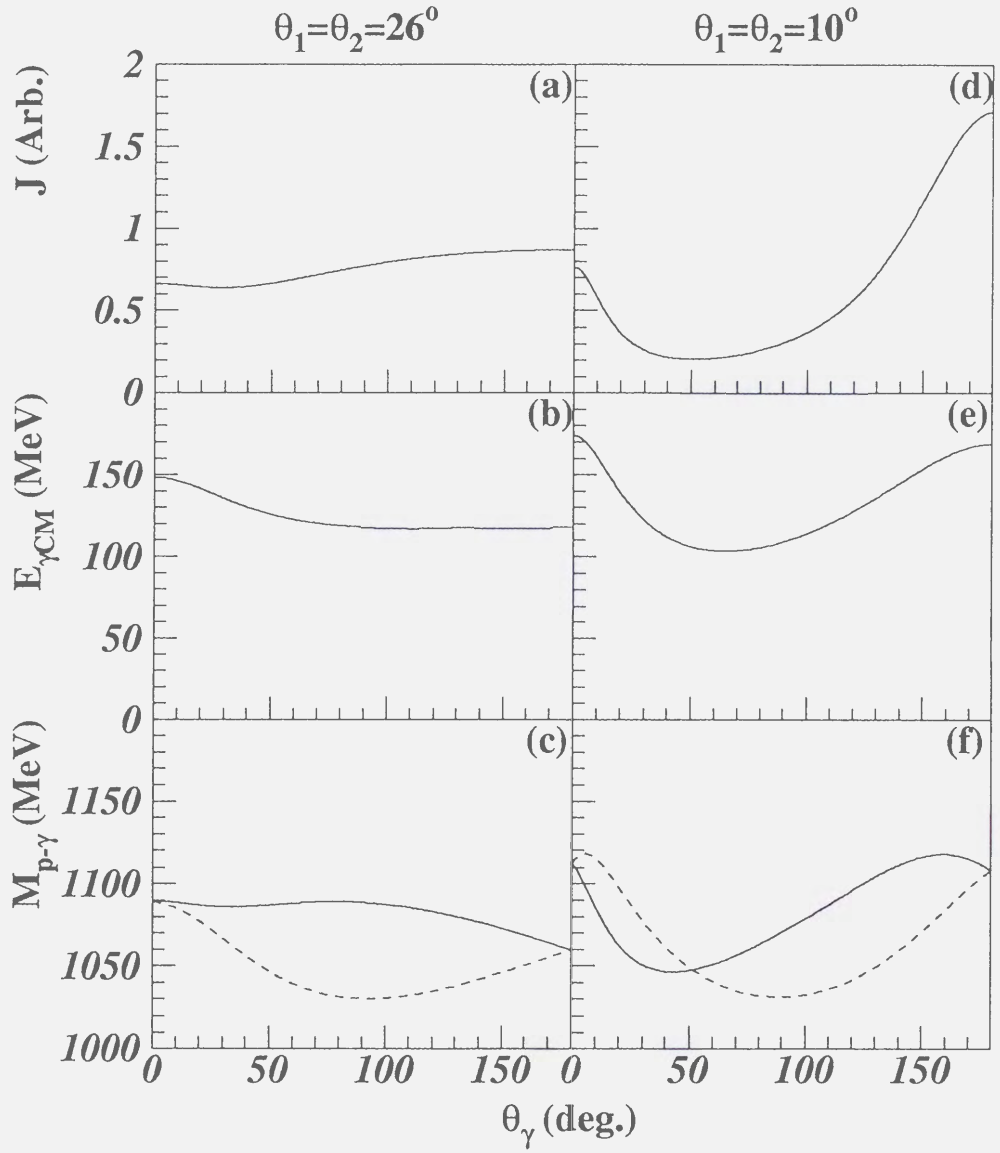

Figure 5.3: Kinematical quantities in the coplanar geometry as a function of the photon emission angle in the laboratory system. The incident energy is $T_p = 389.3$ MeV and proton scattering angles are $\theta_1 = \theta_2 = 26°$ (left) and $\theta_1 = \theta_2 = 10°$ (right). (a) and (d): the phase space factor $\mathcal{J}$ calculated with Eq. (A.9). (b) and (e): the photon energy in the center of mass system. (c) and (f): proton-γ invariant mass for the higher momentum proton (solid) and the lower momentum proton (dashed).

cesses of the NN and $N\Delta$ scattering, and single-scattering diagrams and re-scattering diagrams are considered in the calculations. The diagrams included in the calculation are shown in Fig. 5.4. They used the off-shell T-matrix element that are generated from a $NN \oplus N\Delta \oplus \pi NN$ coupled-channel model developed by Lee and Matsuyama [63, 64]. The T-matrices for the $NN \to N\Delta$ and $N\Delta \to NN$ are calculated with the transition potential $V_{NN\leftrightarrow N\Delta}$ taken from the one-pion-exchange model [65]. In the NN T-matrix, the effective NN potential, which includes the Paris potential and the Δ intermediate state calculated with the $V_{NN\leftrightarrow N\Delta}$, are used. This NN T-matrix can describe the NN phase shifts reasonably well up to about 1 GeV.

The vertex function for the $N\Delta\gamma$ vertex, $\Gamma_\mu^{N\Delta\gamma}$ is written as

$$\Gamma_\mu^{N\Delta\gamma} = K_\mu^1 + K_\mu^2 \tag{5.4}$$

with

$$\begin{aligned} K_\mu^1 &= -ieG_1(\not{k}\epsilon_\mu - \not{\epsilon}k_\mu)\gamma_5 T_z\,, \\ K_\mu^2 &= -ieG_2(\epsilon_\mu P\cdot k - \epsilon.Pk_\mu)\gamma_5 T_z\,, \end{aligned} \tag{5.5}$$

where $k_\mu = p_\mu^{in} - p_\mu^{out}$ is the photon momentum and $P = \frac{1}{2}(p_\mu^\Delta + p_\mu^N)$. T_z is the third component of the isospin transition matrix for coupling an isospin 3/2 particle to an isospin 1/2 particle. For the $\Delta \to N\gamma$, we have

$$\Gamma_\mu^{\Delta N\gamma} = -K_\mu^1 + K_\mu^2\,. \tag{5.6}$$

The coupling constants, G_1 and G_2 are determined by the fitting to the $M1$ and $E1$ multipole data on the photoproduction of pions from nucleons. The values obtained depend on the treatment of the nonresonant background contribution and have some ambiguity. Since the vertex K_μ^1 gives the dominant contribution, we can classify the various sets of coupling constants by the magnitude of G_1. The highest value of G_1 is given by Jones and Scadron [50]: $G_1 = 2.68$ (GeV^{-1}) and $G_2 = -1.84$ (GeV^{-2}). The lowest value is obtained by assuming vector-meson dominance, in which only the isospin-1 vector meson contributes on the $N\Delta\gamma$ vertex. This procedure gives $G_1 = 2.0$ (GeV^{-1}) and $G_2 = 0$ (GeV^{-2}) [51]. Details of the formalism of this model are described in Appedix E. They succeeded to reproduce the TRIUMF data [12] at an incident energy of 280 MeV without normalization factor, 2/3 [20]. At this energy, the Δ contribution is small compared to the present energy region.

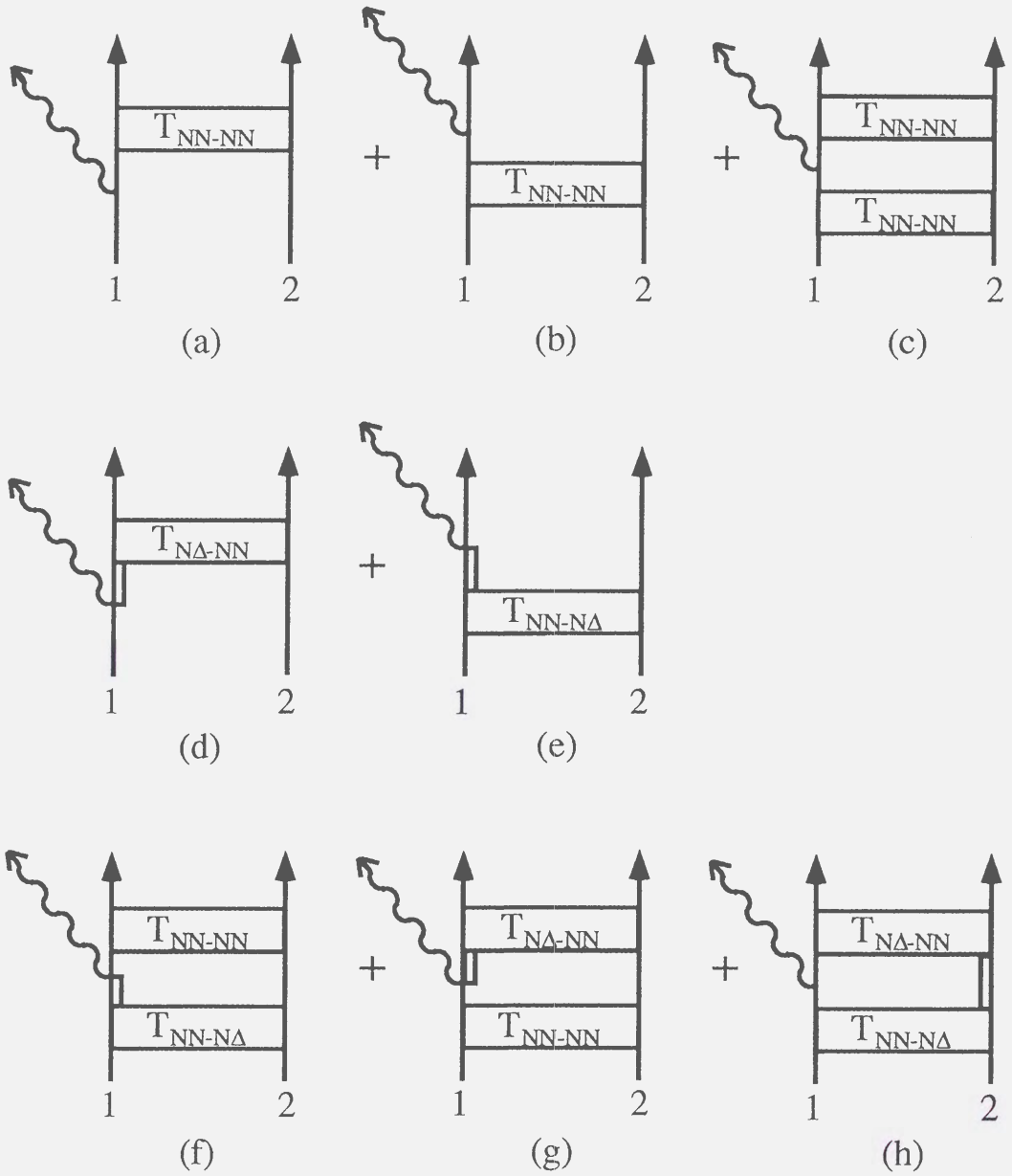

Figure 5.4: Diagrams included in the calculation. A single line denotes a nucleon and a double line a Δ intermediate state.

In Fig. 4.1, the solid line and dashed line correspond to the calculations including both the nucleonic and Δ currents. These correspond to the two choice of the $N\Delta\gamma$ coupling constants. The solid line is the result of the calculation using the highest value of G_1 ($G_1 = 2.68$ (GeV^{-1}) and $G_2 = -1.84$ (GeV^{-2})) and the dashed one is the result using the lowest value ($G_1 = 2.0$ (GeV^{-1}), $G_2 = 0$ (GeV^{-2})) discussed in Ref. [20]. The dotted line is the result of the calculation including only the nucleonic current contribution. These calculations predict that the Δ effect is seen at forward photon emission angles and the differential cross section increases by a factor two at around $\theta_\gamma = 70°$. In the present kinematical condition, the invariant mass of the proton-photon system does not reach the resonance region and the contribution from the Δ current is due to strong interference of a small Δ contribution with much larger nucleon current contribution. The present cross section data favors the calculations including the Δ current, but especially at around $\theta_\gamma = 70°$, where the effect of the Δ current seems to be large, the present result is about 70% larger than the theoretical prediction including the contribution of the Δ current. On the other hand, the present result agrees with the theoretical predictions at the backward angles. The contribution of the Δ current depends on the $N\Delta\gamma$ coupling constants, and the coupling constants have some ambiguity. There are two calculations which is obtained with the highest and lowest values of G_1 in order to study the influence of the ambiguity of the coupling constant. The difference between the cross sections using the two sets of coupling constants is estimated to be less than 20% at the present kinematical conditions [31]. Therefore the ambiguity of the $N\Delta\gamma$ coupling constant can not explain the discrepancy between the present data and the theoretical prediction.

Figure 4.2 shows the analyzing power data. The lines are the same as Fig. 4.1. The contribution from the Δ current is predicted to be small in the analyzing power, and it is difficult to distinguish the difference of the calculations due to the large statistical errors. However, at around $\theta_\gamma = 70°$, where there are discrepancies between the cross section data and the theoretical calculations including the Δ current, there are differences between the data and the theoretical calculations.

In the cross section and the analyzing power data, there are discrepancies between the data and theoretical calculations at around $\theta_\gamma = 70°$. These discrepancies suggest

that there are some other reaction mechanisms which contributes to the $pp\gamma$ reaction. In the calculations discussed here, the effects of the meson-exchange currents and negative-energy states are not included. Martinus *et al.* calculate the $pp\gamma$ cross section including meson-exchange currents, Δ current and negative energy states at our kinematical conditions [24, 52, 53]. In their calculations, the relativistic one-boson exchange model of Fleischer and Tjon [54] is used for the NN interaction. Figure 5.5 shows the result of the calculations with the nucleonic current (dashed), the nucleonic and the meson-exchange currents (dotted), the nucleonic and the Δ current (dot-dashed), and the nucleonic and the meson-exchange and the Δ currents (solid). These calculations predict that the effect of the meson-exchange currents is smaller than that of the Δ current. These predictions for the $pp\gamma$ cross section are slightly smaller than those by de Jong *et al.*. There are two reasons why the predictions for the cross section by Martinus *et al.* are smaller than those by de Jong *et al.*. One is that the different T-matrices are used, and the other is the effect of the negative-energy states. In any case, the effect of the negative-energy states does not seem to be large enough to explain the present data. As discussed above, the discrepancy between the present data and the theoretical predictions can not be explained by the reaction mechanisms which have been taken into account so far, and further theoretical investigations are necessary to explain the discrepancies.

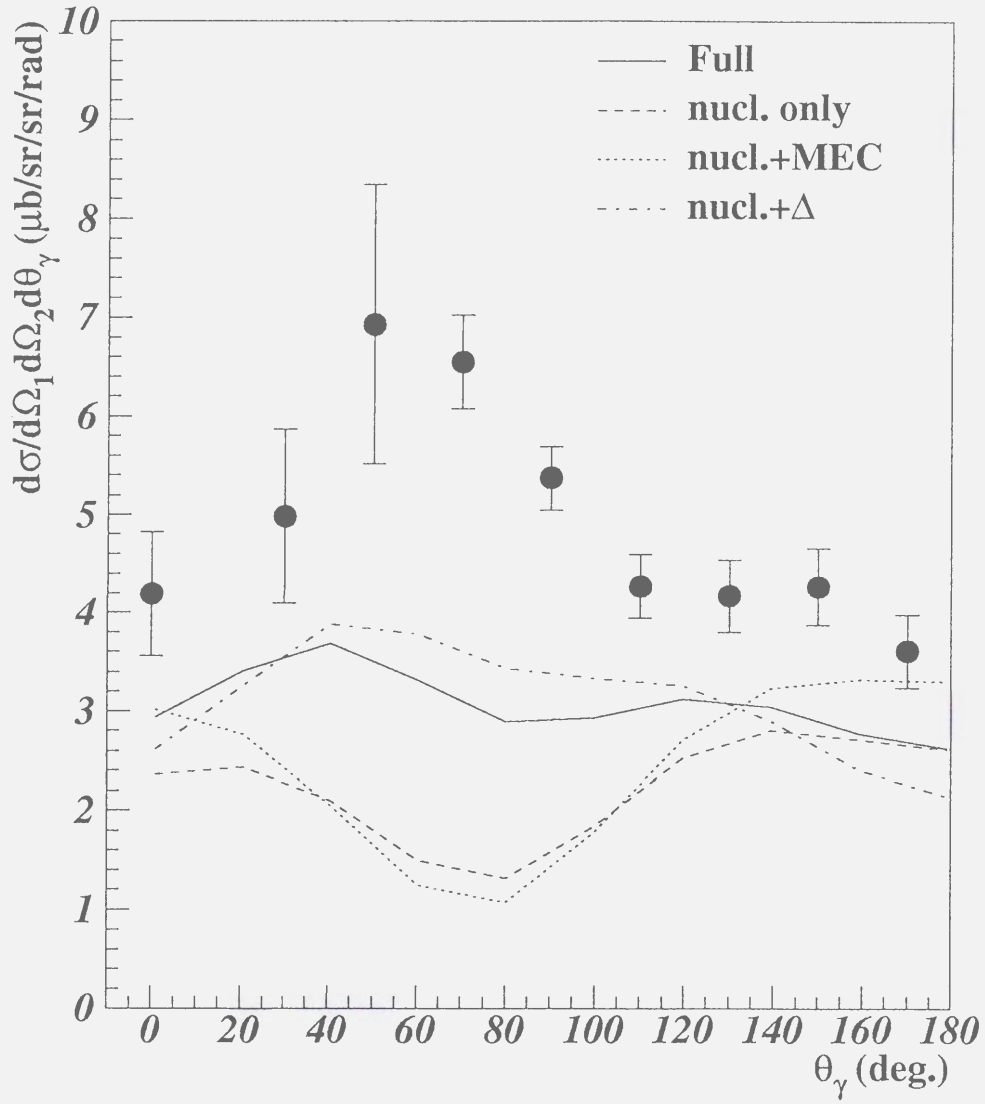

Figure 5.5: The differential cross section for the $pp\gamma$ calculated with the nucleonic current (dashed), the nucleonic and the meson-exchange currents (dotted), the nucleonic and the Δ current (dot-dashed), and the nucleonic and the meson-exchange and the Δ currents (solid). The effect of the negative-energy states were included in all calculations.

Chapter 6

Conclusion

The differential cross sections and analyzing powers for the $pp \rightarrow pp\gamma$ at 389 MeV incident energy have been measured. The two outgoing protons were detected with the two-arm magnetic spectrometer both at the scattering angles of 26.0°. The present data are the first results in the 400 MeV incident energy region, which is far above pion production threshold, and in the kinematical region where it is predicted that contribution from the Δ current is significant. Using the magnetic spectrometer and the liquid hydrogen target, we have succeeded in measuring the $pp \rightarrow pp\gamma$ events with small background.

The cross sections were deduced with an absolute normalization error of about 6%. The cross section data of the pp elastic scattering with a CH_2 target agree well with the values obtained by the *SAID* program.

The $pp\gamma$ differential cross sections and analyzing powers were compared with the potential model calculations with and without contribution from the Δ current. The obtained $pp\gamma$ cross sections are much larger than the theoretical calculations without the Δ current contribution at around $\theta_\gamma = 70°$, where the effect of the Δ current is expected to be large. The contribution from the Δ current improves the agreement with the present cross section data. However, the theoretical calculations even including the Δ current underestimate the present cross section data at around $\theta_\gamma = 70°$. At backward photon angle where the effect of the Δ current is expected to be small, the present data are consistent with the theoretical calculations. The effects of the meson-exchange currents and negative-energy states can not explain the discrepancy, and a further theoretical study is desired in order to find the origin of this discrepancy.

The analyzing powers of the $pp\gamma$ reaction were compared with the same theoretical calculations. The difference of the theoretical calculations with and without contribution from the Δ current is small, and it is difficult to distinguish the calculations due to the large statistical errors. At around $\theta_\gamma = 70°$, however, there are differences between the data and the theoretical calculations

In the cross section and the analyzing power data, there are discrepancies between the data and theoretical calculations at around $\theta_\gamma = 70°$. The discrepancies between the present data and the theoretical predictions can not be explained by the reaction mechanisms such as the meson-exchange currents and the negative-energy states, which have been taken into account so far, and further theoretical investigations are necessary to explain the discrepancies.

Acknowledgement

First of all, I would like to express my appreciation to all the collaborators of the present experiment (RCNP E73,E103) for their effort to accomplish the experiment; Dr. H. Akiyoshi, Dr. T. Hotta, Prof. K. Imai, Mr. M. Kato, Dr. M. Kawabata, Mr. Y. Maeda, Dr. N. Matsuoka, Mr. T. Matsuzuka, Prof. Y. Mizuno, Dr. T. Murakami, Dr. J. Murata, Mr. I. Nakagawa, Prof. M. Nomachi, Prof. T. Noro, Dr. Y. Sugaya, Dr. K. Takahisa, Mr. K. Takanashi, Prof. T. Tamae, Prof. K. Tamura, Prof. H. Toki, Prof. H. Tsubota, Mr. Y. Yokota, Mr. H. P. Yoshida, Mr. M. Yoshimura, and Dr. Y. Yuasa. Prof. M. Nomachi is the spokesperson of the experiment. I have had useful discussions with him during all the stages of this work. Prof. K. Imai is my supervisor of the graduate study. He gave me a good opportunity to take part in this experiment and encouraged me through this study.

I wish to acknowledge Prof. K. Sagara for our use of their liquid hydrogen target system. I am grateful to Mr. A. Tamii for the operation of the DAQ system. He constructed the DAQ system at RCNP, and he helped us when we were in trouble about the electric circuit and the DAQ system. I also thank Dr. H. Akimune for a useful guidance in the operation of the beam halo monitor. I wish to thank Mr. H. Togawa for the support of the computer system at RCNP.

The present experiment was supported by the staffs at the RCNP. I would like to thank for their continuous support during the preparation and the experiment. I am deeply grateful to Prof. K. Hatanaka, Prof. T. Saito, and the SAS members for the operation of the accelerator. I also express my special thanks to Prof. H. Ejiri, who is the director of the RCNP, for his continuous encouragement throughout the experiment.

I wish to thank Prof. K. Nakayama. He performed the theoretical calculations for

the present data and gave me lectures on the theory. I am grateful to Prof. O. Scholten for fruitful discussion and for providing the theoretical calculations.

I would like to express my special thanks to Prof. H. Sakaguchi, Dr. M. Nakamura, Dr. K. Takimoto, Mr. M. Yosoi, and other members of the NE group in Kyoto University for their countless encouragement, discussion, and collaboration.

Finally, I express my great thanks to my wife, Miyako Yasuda. She supported and took care of me. I wish to thank my parents, Keishu and Mitsuko Yasuda, and my grandmother, Tsuta Morikawa, for their continuous encouragement and support

Appendix A

Phase space calculation

The differential cross section can be expressed as

$$d\sigma = \frac{1}{F}|\mathcal{M}|^2 d\mathcal{Q} \tag{A.1}$$

where

$$\begin{aligned} F &= |\vec{\beta}_{beam} - \vec{\beta}_{target}| 2E_{beam} 2E_{target} \\ &= 4\sqrt{(\vec{p}_{beam} \cdot \vec{p}_{target})^2 - m_{beam}^2 m_{target}^2} \end{aligned} \tag{A.2}$$

is the flux factor [55]. The phase space factor is denoted by $d\mathcal{Q}$ and the invariant matrix element is expressed as $|\mathcal{M}|^2$. The phase space factor which counts the density of final states and takes energy and momentum conservation into account is for a three particle final state given by

$$d\mathcal{Q} = (2\pi)^4 \delta^4(p_{beam} + p_{target} - p_1 - p_2 - p_\gamma) \times \frac{d^3\vec{p_1}}{(2\pi)^3 2E_1} \frac{d^3\vec{p_2}}{(2\pi)^3 2E_2} \frac{d^3\vec{p_\gamma}}{(2\pi)^3 2E_\gamma}, \tag{A.3}$$

where script p denotes an energy-momentum 4-vector and $\vec{p}$ the momentum 3-vector [55]. Due to the 4-dimensional delta function only 5 kinematical variables remain. These are chosen to be the angles of the particles in the present analysis and the phase space factor can be rewritten as

$$d\mathcal{Q} = d\Omega_1 d\Omega_2 d\theta_\gamma \times \mathcal{J} \tag{A.4}$$

where Ω_1 and Ω_2 are solid angles of the two protons, θ_γ is a photon emission angle, and $\mathcal{J}$ is the Jacobian.

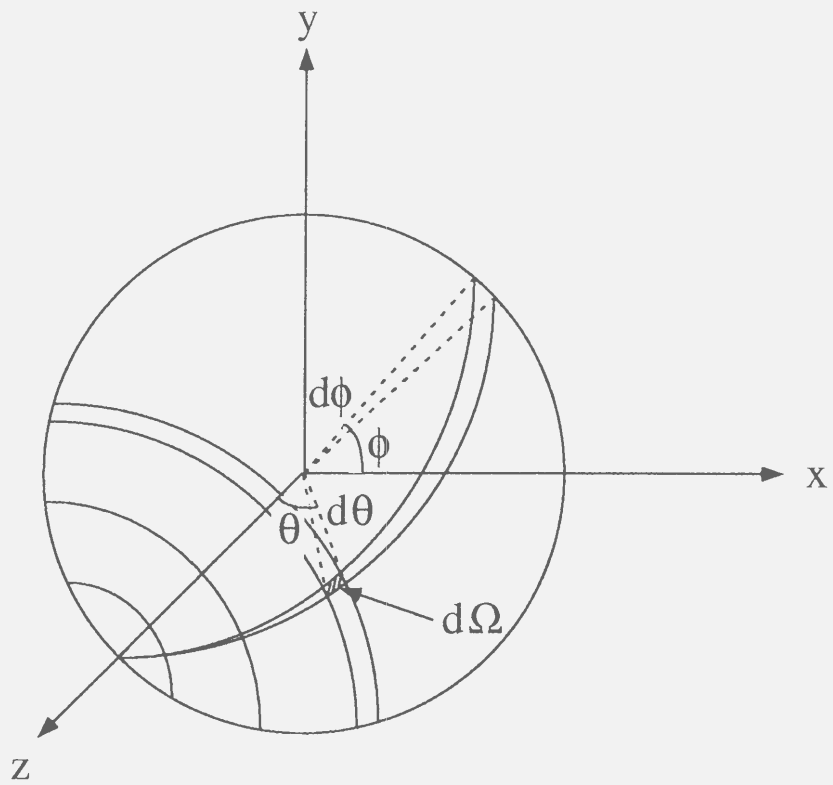

Figure A.1: dΩ in the polar angle system.

A.1 Jacobian for the polar angle system

In the polar angle system, $d\Omega$ is written as

$$d\Omega = \sin\theta d\theta d\phi\,, \tag{A.5}$$

as shown in Fig. A.1. The Jacobian $\mathcal{J}$ is

$$\mathcal{J} = \frac{1}{8(2\pi)^5}\int \delta^4(p_{beam} + p_{target} - p_1 - p_2 - p_\gamma)\frac{|\vec{p_1}|^2 d|\vec{p_1}||\vec{p_2}|^2 d|\vec{p_2}||\vec{p_\gamma}|^2 d|\vec{p_\gamma}|\sin\theta_\gamma d\phi_\gamma}{E_1 E_2 E_\gamma}\,. \tag{A.6}$$

Taking as independent final state observables θ_1, θ_2, ϕ_1, ϕ_2 and θ_γ, then the momenta and angles $|\vec{p_1}|$, $|\vec{p_2}|$, $|\vec{p_\gamma}|$ and ϕ_γ can be calculated from the energy-momentum conservation.

The four-fold phase space integral in the Jacobian Eq. A.6 can be performed

analytically once the kinematics is solved. The result is

$$\begin{aligned}
\mathcal{J} &= \frac{1}{8(2\pi)^5}\frac{|\vec{p_1}|^2|\vec{p_2}|^2|\vec{p_\gamma}|}{E_1E_2E_\gamma|R|}, \\
R &= \beta_1(\sin\theta_\gamma\cos\theta_2 - \cos\theta_\gamma\sin\theta_2\cos\phi_{2\gamma}) \\
&+ \beta_2(\cos\theta_\gamma\sin\theta_1\cos\phi_{\gamma 1} - \sin\theta_\gamma\cos\theta_1) \\
&+ \beta_\gamma(\cos\theta_1\sin\theta_2\cos\phi_{2\gamma} - \sin\theta_1\cos\theta_2\cos\phi_{\gamma 1}),
\end{aligned} \tag{A.7}$$

where $\phi_{ij} = \phi_i - \phi_j$ and $\beta_i = |\vec{p_i}|/E_i$.

A.2 Jacobian for the "horizontal-vertical" angle system

In the "horizontal-vertical" angle system, $d\Omega$ is written as

$$d\Omega = \cos\Phi d\Phi d\Theta\,, \tag{A.8}$$

as shown in Fig. A.2. The Jacobian $\mathcal{J}$ is

$$\mathcal{J} = \frac{1}{8(2\pi)^5}\int \delta^4(p_{beam} + p_{target} - p_1 - p_2 - p_\gamma)\frac{|\vec{p_1}|^2 d|\vec{p_1}||\vec{p_2}|^2 d|\vec{p_2}||\vec{p_\gamma}|^2 d|\vec{p_\gamma}|\cos\Phi_\gamma d\Phi_\gamma}{E_{p_1}E_{p_2}E_{p_\gamma}}. \tag{A.9}$$

Taking as independent final state observables Θ_1, Θ_2, Φ_1, Φ_2 and Θ_γ, then the momenta and angles $|\vec{p_1}|$, $|\vec{p_2}|$, $|\vec{p_\gamma}|$ and Φ_γ can be calculated from the energy-momentum conservation.

The four-fold phase space integral in the Jacobian Eq. A.9 can be performed analytically once the kinematics is solved. The result is

$$\begin{aligned}
\mathcal{J} &= \frac{1}{8(2\pi)^5}\frac{|\vec{p_1}|^2|\vec{p_2}|^2|\vec{p_\gamma}|}{E_1E_2E_\gamma|R|}, \\
R &= \frac{\beta_1}{\cos\Phi_\gamma}\cos\Phi_2\sin\Theta_{\gamma 2} + \frac{\beta_2}{\cos\Phi_\gamma}\cos\Phi_1\sin\Theta_{1\gamma} + \frac{\beta_\gamma}{\cos\Phi_\gamma}(\cos\Phi_1\cos\Phi_2\cos\Phi_\gamma\sin\Theta_{21} \\
&- \cos\Phi_1\sin\Phi_2\sin\Phi_\gamma\sin\Theta_{1\gamma} - \sin\Phi_1\cos\Phi_2\sin\Phi_\gamma\sin\Theta_{\gamma 2})
\end{aligned} \tag{A.10}$$

where $\Theta_{ij} = \Theta_i - \Theta_j$ and $\beta_i = |\vec{p_i}|/E_i$.

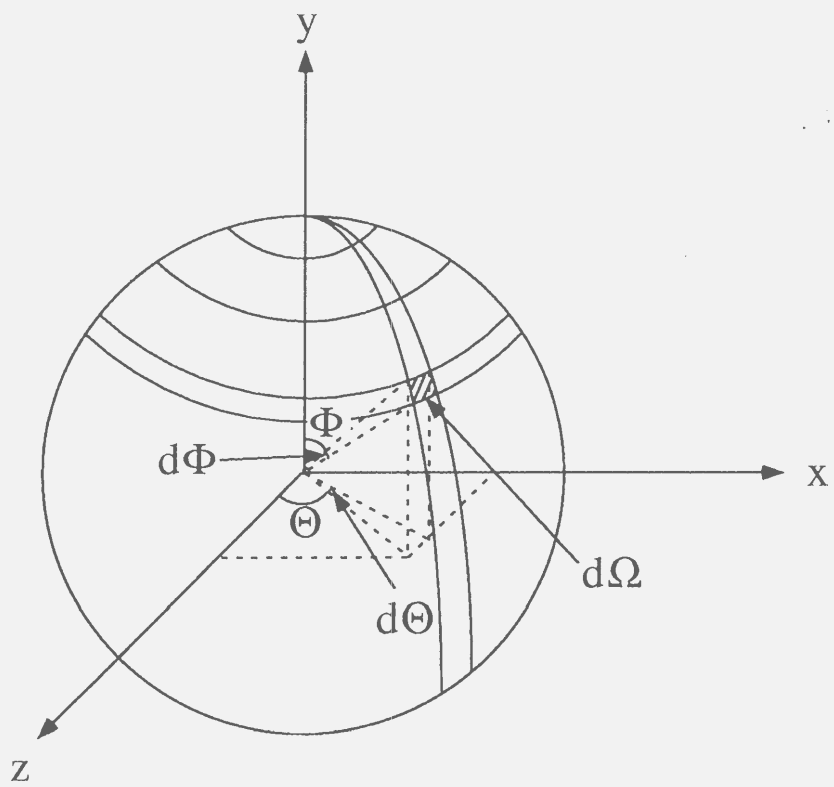

Figure A.2: $d\Omega$ in the "horizontal-vertical" angle system.

A.3 Jacobian for the coplanar geometry case

In the coplanar geometry case, the Jacobians for the polar angle system and the "horizontal-vertical" angle system are identical.

In the polar angle system, we assume $\phi_2 = \phi_\gamma = 0$ and $\phi_1 = \pi$. The R in the polar angle system, R_p, is expressed as,

$$R_p = \beta_1 \sin(\theta_\gamma - \theta_2) - \beta_2 \sin(\theta_\gamma + \theta_1) + \beta_\gamma \sin(\theta_1 + \theta_2) \tag{A.11}$$

In the "horizontal-vertical" angle system, the above condition corresponds to $\Phi_1 = \Phi_2 = \Phi_\gamma = 0$, $\Theta_1 = -\theta_1$, $\Theta_2 = \theta_2$, and $\Theta_\gamma = \theta_\gamma$. The R in the "horizontal-vertical" angle system, R_h, is expressed as,

$$\begin{aligned} R_h &= \beta_1 \sin\Theta_{\gamma 2} + \beta_2 \sin\Theta_{1\gamma} + \beta_\gamma \sin\Theta_{21} \\ &= \beta_1 \sin(\theta_\gamma - \theta_2) - \beta_2 \sin(\theta_\gamma + \theta_1) + \beta_\gamma \sin(\theta_1 + \theta_2) \\ &= R_p \end{aligned} \tag{A.12}$$

As a result, the differential cross section evaluated in the "horizontal-vertical" angle system is the same as that in the polar angle system in the coplanar geometry case.

Appendix B

Phase space correction for the cross section

Due to the limited momentum acceptance of the spectrometer system, the $pp\gamma$ phase space is limited and correction is needed for evaluating the cross sections from the $pp\gamma$ yield. Moreover, since the geometrical acceptances of the spectrometers are finite, the cross sections obtained by the present experiment are the averaging values in the acceptances. Theoretical calculations are, however, performed at the infinitesimal geometry. Correction for the effect of the geometrical acceptances is needed in order to compare the present data with the theoretical calculations. In this appendix, a correction method for the above two effects is presented.

In the $pp \to pp\gamma$ reaction, there are three particles in the final state. Therefore there are nine kinematical variables in the final state (3×3 particles). Four degrees of freedom of them are reduced with the energy-momentum conservation raw. Therefore there are five degrees of the freedom in the kinematical variables. In the following discussion, the five free kinematical variables are denoted by X and other four variables are denoted by Y. The beam is assumed to be unpolarized for simplification.

As seen in Appendix A, the differential cross section can be expressed as

$$d\sigma = \frac{1}{F}|\mathcal{M}|^2 d\mathcal{Q}\,, \tag{B.1}$$

where F is the flux factor, $\mathcal{M}$ is the invariant matrix element and $d\mathcal{Q}$ is the phase space factor. The phase space factor, $d\mathcal{Q}$, is expressed as,

$$d\mathcal{Q} \;=\; (2\pi)^4\delta^4(p_{beam} + p_{target} - p_1 - p_2 - p_\gamma) \times \frac{d^3\vec{p_1}}{(2\pi)^3 2E_1}\frac{d^3\vec{p_2}}{(2\pi)^3 2E_2}\frac{d^3\vec{p_\gamma}}{(2\pi)^3 2E_\gamma}\,,$$

(B.2)

In the present analysis, the angles of the particles are chosen as the five free kinematical variables, X, and the phase space factor is expressed as

$$\begin{aligned} d\mathcal{Q} &= \mathcal{J}(X)dX\,, \\ dX &= d\Omega_1 d\Omega_2 d\theta_\gamma\,, \end{aligned} \tag{B.3}$$

where Ω_1 and Ω_2 are solid angles of the two protons, θ_γ is a photon emission angle, and $\mathcal{J}(X)$ is the Jacobian. In the "horizontal-vertical" angle system, the Jacobian is expressed as,

$$\begin{aligned} \mathcal{J}(X) &= \frac{1}{8(2\pi)^5}\int \delta^4(p_{beam}+p_{target}-p_1-p_2-p_\gamma)\frac{|\vec{p_1}|^2 d|\vec{p_1}||\vec{p_2}|^2 d|\vec{p_2}||\vec{p_\gamma}|^2 d|\vec{p_\gamma}|\cos\Phi_\gamma d\Phi_\gamma}{E_{p_1}E_{p_2}E_{p_\gamma}} \\ &= \int f(X,Y)dY\,, \end{aligned} \tag{B.4}$$

where

$$\begin{aligned} dY &= d|\vec{p_1}|d|\vec{p_2}|d|\vec{p_\gamma}|d\Phi_\gamma\,, \\ f(X,Y) &= \frac{1}{8(2\pi)^5}\int \delta^4(p_{beam}+p_{target}-p_1-p_2-p_\gamma)\frac{|\vec{p_1}|^2|\vec{p_2}|^2|\vec{p_\gamma}|^2\cos\Phi_\gamma}{E_{p_1}E_{p_2}E_{p_\gamma}}\,. \end{aligned} \tag{B.5}$$

The differential cross section can be rewritten as,

$$d\sigma = \frac{1}{F}|\mathcal{M}(X)|^2\mathcal{J}(X)dX\,. \tag{B.6}$$

From Eqs. B.6 and B.4, the differential cross section is expressed as

$$d\sigma = \left[\int dY \frac{1}{F}|\mathcal{M}(X)|^2 f(X,Y)\right]dX\,. \tag{B.7}$$

The measured cross section is expressed as

$$\left(\frac{d\sigma}{dX}\right)_{exp} = \frac{\mathcal{Y}}{\mathcal{L}\Delta X}\,, \tag{B.8}$$

where $\mathcal{Y}$ is the yield and $\mathcal{L}$ is the luminosity. The relation between Eqs. B.7 and B.8 can be expressed as

$$\left(\frac{d\sigma}{dX}\right)_{exp} \Delta X = \iint dX dY \frac{1}{F} |\mathcal{M}(X)|^2 f(X,Y)\epsilon(X,Y)\,, \tag{B.9}$$

$$\Delta X = \int dX\,, \tag{B.10}$$

where $\epsilon(X,Y)$ expresses the detector acceptance and is defined as

$$\begin{aligned} \epsilon(X,Y) &= 1 \quad \text{(X and Y are in the acceptance)}\,, \\ \epsilon(X,Y) &= 0 \quad \text{(X or Y are out of the acceptance)}\,. \end{aligned} \tag{B.11}$$

Here, the invariant matrix element $\mathcal{M}(X)$ is assumed to be constant in the detector acceptance. The measured cross section can expressed as

$$\begin{aligned} \left(\frac{d\sigma}{dX}\right)_{exp} \Delta X &\simeq \frac{1}{F}|\mathcal{M}(X_0)|^2 \iint dX dY f(X,Y)\epsilon(X,Y) \\ &= \frac{1}{F}|\mathcal{M}(X_0)|^2 \frac{\iint dX dY f(X,Y)\epsilon(X,Y)}{\iint dX dY f(X,Y)} \iint dX dY f(X,Y) \\ &= \frac{1}{F}|\mathcal{M}(X_0)|^2 C_a \int dX \mathcal{J}(X) \qquad \text{(B.12)} \\ C_a &= \frac{\iint dX dY f(X,Y)\epsilon(X,Y)}{\iint dX dY f(X,Y)} \qquad \text{(B.13)} \end{aligned}$$

$$\begin{aligned} \left(\frac{d\sigma}{dX}\right)_{exp} &= \frac{1}{F}|\mathcal{M}(X_0)|^2 C_a \frac{\int dX \mathcal{J}(X)}{\int dX} \\ &= \frac{1}{F}|\mathcal{M}(X_0)|^2 \mathcal{J}(X_0) C_a C_0 \qquad \text{(B.14)} \\ C_0 &= \frac{1}{\mathcal{J}(X_0)} \frac{\int dX \mathcal{J}(X)}{\int dX} \qquad \text{(B.15)} \end{aligned}$$

Finally, the differential cross section for the infinitesimal geometrical acceptance is expressed as

$$\begin{aligned} \frac{d\sigma}{dX}(X_0) &= \frac{1}{F}|\mathcal{M}(X_0)|^2 \mathcal{J}(X_0) \qquad \text{(B.16)} \\ &= \frac{1}{C_a C_0}\left(\frac{d\sigma}{dX}\right)_{exp}. \qquad \text{(B.17)} \end{aligned}$$

where C_a is the correction factor for the limited momentum acceptance and C_0 for the finite geometrical acceptance of the detector.

Appendix C

Classical theory for the bremsstrahlung

In this appendix, the classical theory for the NN bremsstrahlung for the soft photon limit ($\hbar\omega \to 0$) is discussed. This is valid in the case of relatively low photon energy and difficult to apply to the present data. However, it is useful for understanding of the NN bremsstrahlung to investigate with the classical theory. The important feature of the difference between the $pp\gamma$ and $pn\gamma$ is explained with the classical theory.

We start the expression of the strength for the radiation of a charged particle (ze), which is described in Chapter 15 of Ref. [56],

$$\frac{d^2I}{d\omega d\Omega} = \frac{z^2e^2}{4\pi^2c}\left|\int \frac{d}{dt}\left[\frac{\vec{n}\times\left(\vec{n}\times\vec{\beta}\right)}{1-\vec{n}\cdot\vec{\beta}}\right] e^{i\omega\left(t-\frac{\vec{n}\cdot\vec{r}(t)}{c}\right)}dt\right|^2 \tag{C.1}$$

where integration is taken between the collision time and the spectrum depends on the details of the collision. In the limit of $\omega \to 0$,the spectrum depends only on the initial and final momentum of the charged particle and expressed as,

$$\begin{aligned}\frac{d^2I}{d\omega d\Omega} &= \frac{z^2e^2}{4\pi^2c}\left|\frac{\vec{n}\times\left(\vec{n}\times\vec{\beta}'\right)}{1-\vec{n}\cdot\vec{\beta}'} - \frac{\vec{n}\times\left(\vec{n}\times\vec{\beta}\right)}{1-\vec{n}\cdot\vec{\beta}}\right|^2 \\ &= \frac{z^2e^2}{4\pi^2c}\left|\vec{n}\times\left(\vec{n}\times\left(\frac{\vec{\beta}'}{1-\vec{n}\cdot\vec{\beta}'} - \frac{\vec{\beta}}{1-\vec{n}\cdot\vec{\beta}}\right)\right)\right|^2\end{aligned}$$

$$= \frac{z^2e^2}{4\pi^2c}\left|\vec{\epsilon}\cdot\left(\frac{\vec{\beta}'}{1-\vec{n}\cdot\vec{\beta}'}-\frac{\vec{\beta}}{1-\vec{n}\cdot\vec{\beta}}\right)\right|^2 . \tag{C.2}$$

We obtain the differential number of photons spectrum by dividing Eq. (C.2) by $\hbar^2\omega$,

$$\begin{aligned}\frac{d^2N}{d(\hbar\omega)d\Omega} &= \frac{z^2e^2}{4\pi^2\hbar c\hbar\omega}\left|\vec{\epsilon}\cdot\left(\frac{\vec{\beta}'}{1-\vec{n}\cdot\vec{\beta}'}-\frac{\vec{\beta}}{1-\vec{n}\cdot\vec{\beta}}\right)\right|^2 \\ &= \frac{\alpha z^2}{4\pi^2\hbar\omega}\left|\vec{\epsilon}\cdot\left(\frac{\vec{\beta}'}{1-\vec{n}\cdot\vec{\beta}'}-\frac{\vec{\beta}}{1-\vec{n}\cdot\vec{\beta}}\right)\right|^2 , \end{aligned} \tag{C.3}$$

where α is the fine-structure constant. Invariant form of the Eq. (C.3) is expressed as

$$\begin{aligned}\frac{d^3N}{(d^3k/k_0)} &= \frac{k_0d^2N}{k^2dkd\Omega_\gamma} = \frac{\left(\frac{\hbar\omega}{c}\right)d^2N}{\left(\frac{\hbar\omega}{c}\right)^2 d\left(\frac{\hbar\omega}{c}\right)d\Omega_\gamma} \\ &= \frac{c^2}{\hbar\omega}\frac{d^2N}{d(\hbar\omega)d\Omega_\gamma} \\ &= \frac{\alpha z^2}{4\pi^2\hbar\omega}\frac{c^2}{\hbar\omega}\left|\vec{\epsilon}\cdot\left(\frac{\vec{\beta}'}{1-\vec{n}\cdot\vec{\beta}'}-\frac{\vec{\beta}}{1-\vec{n}\cdot\vec{\beta}}\right)\right|^2 . \end{aligned} \tag{C.4}$$

We introduce the 4-vector of the particle and photon,

$$\begin{aligned} q^\mu &= (\hbar/c)(\omega,\omega\vec{n}) , \\ p^\mu &= Mc(\gamma,\gamma\vec{\beta}) . \end{aligned} \tag{C.5}$$

Then Eq. (C.4) is expressed as

$$\frac{d^3N}{(d^3q/q_0)} = \frac{z^2\alpha}{4\pi^2}\left|\frac{\epsilon\cdot p'}{q\cdot p'}-\frac{\epsilon\cdot p}{q\cdot p}\right|^2 . \tag{C.6}$$

Eq. (C.6) shows that the magnitude of the radiation is roughly α times smaller than that of the scattering.

This corresponds to the leading $\mathcal{O}(1/\omega)$ term of the Low's theorem (see Appendix D).

In the case of the NN bremsstrahlung, $N_1 + N_2 \rightarrow N_1' + N_2' + \gamma$, the invariant number of photons spectrum is expressed as

$$\frac{d^3N}{d^3q/q_0} = \frac{\alpha}{4\pi^2}\left|z_1\frac{\epsilon\cdot p_1'}{q\cdot p_1'} - z_1\frac{\epsilon\cdot p_1}{q\cdot p_1} + z_2\frac{\epsilon\cdot p_2'}{q\cdot p_2'} - z_2\frac{\epsilon\cdot p_2}{q\cdot p_2}\right|^2 \tag{C.7}$$

$$= \frac{\alpha}{4\pi^2 q_0^2}\left|z_1\frac{\vec{\epsilon}\cdot\vec{\beta}_1'}{(1-\vec{n}\cdot\vec{\beta}_1')} - z_1\frac{\vec{\epsilon}\cdot\vec{\beta}_1}{(1-\vec{n}\cdot\vec{\beta}_1)} + z_2\frac{\vec{\epsilon}\cdot\vec{\beta}_2'}{(1-\vec{n}\cdot\vec{\beta}_2')} - z_2\frac{\vec{\epsilon}\cdot\vec{\beta}_2}{(1-\vec{n}\cdot\vec{\beta}_2)}\right|^2, \tag{C.8}$$

where $\vec{\beta}$ indicates the velocity of the nucleon and *vecn* the direction of the photon. Figure C.1 shows the invariant number of photons spectrum calculated with Eq. (C.8) at incident energy of $E_p = 200$ MeV and two nucleons angle of $\theta_1 = \theta_2 = 26°$. This shows that the magnitude of $pn\gamma$ is about one order larger than that of $pp\gamma$. The reason for the difference of the magnitude is explained as follows. In the center of mass system, the relationships of $\vec{\beta}_1 = -\vec{\beta}_2 = \vec{\beta}$, and $\vec{\beta}_1' = -\vec{\beta}_2' = \vec{\beta}'$ are realized. In the case of the non-relativistic limit ($\beta \ll 1$), Eq. (C.8) is expressed as

$$\frac{d^3N}{d^3k/k_0} \simeq \frac{\alpha}{4\pi^2 q_0^2}|\vec{\epsilon}\cdot\vec{\beta}'(z_1 - z_2) - \vec{\epsilon}\cdot\vec{\beta}(z_1 - z_2) + (\vec{\epsilon}\cdot\vec{\beta}')(\vec{n}\cdot\vec{\beta}')(z_1 + z_2) - (\vec{\epsilon}\cdot\vec{\beta})(\vec{n}\cdot\vec{\beta})(z_1 + z_2) + \cdots|^2. \tag{C.9}$$

In the case of the $pp\gamma$ reaction, the leading term of Eq. (C.9) vanishes due to $z_1 = z_2 = 1$, whereas the leading term exists in the $pn\gamma$ case. This is the reason that the cross section of the $pp\gamma$ reaction is much smaller than that of the $pn\gamma$ reaction. The amplitude discussed in this section is independent of the details of the scattering, and this result is valid in general.

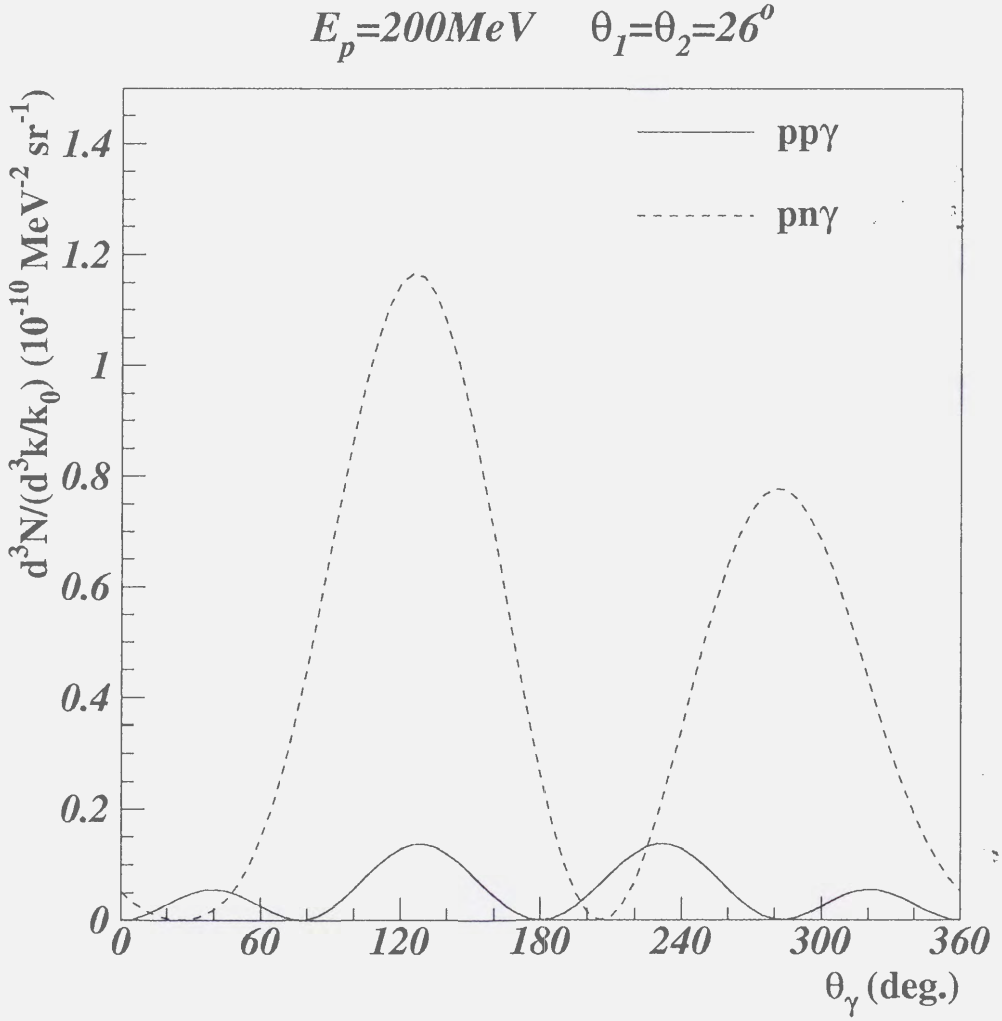

Figure C.1: Invariant number of photons spectrum calculated with Eq. (C.8). The solid line indicates the $pp\gamma$ case and the dashed line the $pn\gamma$ case.

Appendix D

Low energy theorem for pp-bremsstrahlung

A low energy theorem gives a model independent prediction for most processes in which a photon is involved. A general form for the matrix element of the $pp\gamma$ process is obtained by the expansion of the NN T-matrix with the photon energy ω,

$$\mathcal{M} = A/\omega + B + C\omega + \cdots \tag{D.1}$$

where the coefficients A and B are calculated model independently. In this appendix, we will derive the low energy theorem for bremsstrahlung of two spin-$\frac{1}{2}$ particles. This is the original work of Low [57] and application for the NN bremsstrahlung is performed by some theorists [58, 59, 60, 61]. At first we will consider the contribution of the particle 1 and of the radiation from the external line (Fig. D.1). The initial particles have 4-momenta p_1, p_2 and the final particles have p_1', p_2'. The photon has a 4-momentum q. The NN T-matrix depends on three Lorentz invariants, and here we choose them to be the invariant mass of the particle 1 before the scattering (M_i^2), after scattering (M_f^2), and a third parameter $\nu = p_\nu \cdot p_2 + p_\nu' \cdot p_2'$ where p_ν denotes the momentum of the particle 1 before scattering and p_ν' the momentum of the particle 1 after scattering. In the case of the post-emission described as (a) in Fig. D.1, p_ν and p_ν' are described as $p_\nu = p_1$ and $p_\nu' = p_1' + q$, whereas in the case of the pre-emission described as (b), $p_\nu = p_1 - q$ and $p_\nu' = p_1'$. We define $\nu_0 = p_1 \cdot p_2 + p_1' \cdot p_2'$, and ν is expressed as

$$\begin{aligned} \nu &= \nu_0 + q \cdot p_2' \quad \text{for post-emission}, \\ \nu &= \nu_0 - q \cdot p_2 \quad \text{for pre-emission}. \end{aligned}$$

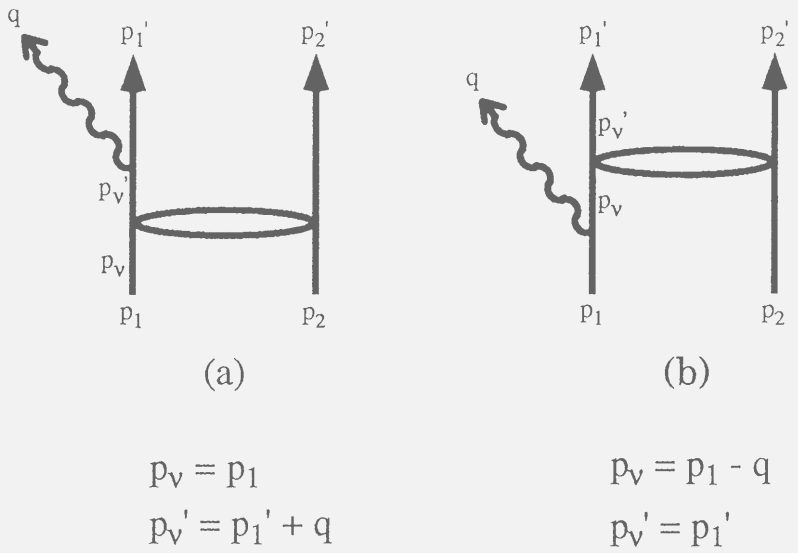

Figure D.1: Diagrams taken into account in this appendix.

In the case of the post- and pre-emission, M_i^2 and M_f^2 are expressed as

$$\begin{aligned} M_i^2 &= p_1^2 = m^2\,, \\ M_f^2 &= (p_1' + q)^2 = m^2 + 2p_1' \cdot q\,, \end{aligned}$$

and

$$\begin{aligned} M_i^2 &= (p_1 - q)^2 = m^2 - 2p_1 \cdot q\,, \\ M_f^2 &= {p_1'}^2 = m^2\,, \end{aligned}$$

where m is the nucleon mass.

The matrix element for the emission from external lines is expressed as

$$\begin{aligned} \mathcal{M}_\mu^{ext} &= \bar{u}(p_1')\Big[e\left(\gamma_\mu + \frac{i\kappa}{2m}\sigma_{\mu\nu}q^\nu\right) i\frac{\not{p}_1' + \not{q} + m}{(p_1' + q)^2 - m^2} T(m^2 + 2p_1' \cdot q, m^2, \nu_0 + q \cdot p_2') \\ &\quad + T(m^2, m^2 - 2p_1 \cdot q, \nu_0 - q \cdot p_2) i\frac{\not{p}_1 - \not{q} + m}{(p_1 - q)^2 - m^2} e\left(\gamma_\mu + \frac{i\kappa}{2m}\sigma_{\mu\nu}q^\nu\right)\Big] u(p_1) \end{aligned} \tag{D.2}$$

We follow the conventions of Aitchison and Hey [62]. The first term in Eq. (D.2) corresponds to the post-emission and the second term corresponds to the pre-emission. The T-matrix can be expanded around the on-shell value.

$$\begin{aligned} T(m^2+2p_1'\cdot q, m^2, \nu_0+q\cdot p_2') &= T(m^2,m^2,\nu_0)+2p_1'\cdot q\frac{\partial T}{\partial M_f^2}(m^2,m^2,\nu_0) \\ &\quad + q\cdot p_2'\frac{\partial T}{\partial \nu}(m^2,m^2,\nu_0) \\ &\equiv T_0 + 2p_1'\cdot qT_1 + q\cdot p_2'T_3 \end{aligned} \tag{D.3}$$

$$\begin{aligned} T(m^2, m^2-2p_1\cdot q, \nu_0-q\cdot p_2) &= T(m^2,m^2,\nu_0)-2p_1\cdot q\frac{\partial T}{\partial M_i^2}(m^2,m^2,\nu_0) \\ &\quad - q\cdot p_2\frac{\partial T}{\partial \nu}(m^2,m^2,\nu_0) \\ &\equiv T_0 - 2p_1\cdot qT_2 - q\cdot p_2T_3 \end{aligned} \tag{D.4}$$

The $\sigma_{\mu\nu}$-term is evaluated with the on-shell propagator, and up to terms of second order in the photon momentum the current is given by

$$\begin{aligned} \mathcal{M}_\mu^{ext} &= ie\bar{u}(p_1')\left[\left(\gamma_\mu+\frac{i\kappa}{2m}\sigma_{\mu\nu}q^\nu\right)\frac{\not{p}_1'+m}{2p_1'\cdot q}T_0 - T_0\frac{\not{p}_1+m}{2p_1\cdot q}\left(\gamma_\mu+\frac{i\kappa}{2m}\sigma_{\mu\nu}q^\nu\right)\right]u(p_1) \\ &\quad + ie\bar{u}(p_1')\left[\gamma_\mu\frac{\not{q}}{2p_1'\cdot q}T_0 - T_0\frac{\not{q}}{2p_1\cdot q}\gamma_\mu\right]u(p_1) \\ &\quad + ie\bar{u}(p_1')\left[\gamma_\mu(\not{p}_1'+m)T_1 + T_2(\not{p}_1+m)\gamma_\mu\right]u(p_1) \\ &\quad + ie\bar{u}(p_1')\left[\gamma_\mu(\not{p}_1'+m)\frac{q\cdot p_2'}{2p_1'\cdot q}T_3 + T_3\frac{q\cdot p_2}{2p_1\cdot q}(\not{p}_1+m)\gamma_\mu\right]u(p_1) \\ &\quad + \mathcal{O}(q) \end{aligned} \tag{D.5}$$

Since the over-all current is conserved, we have

$$q^\mu\mathcal{M}_\mu = 0\,, \tag{D.6}$$

where $\mathcal{M}_\mu = \mathcal{M}_\mu^{ext}+\mathcal{M}_\mu^{int}$. We can obtain $\mathcal{M}_\mu^{int}$ using Eq. (D.6). In order to calculate $\mathcal{M}_\mu^{int}$, $q^\mu\mathcal{M}_\mu^{ext}$ is calculated. The term with $\sigma_{\mu\nu}q^\nu$ and $\not{q}$ are zero, since the photon is real ($q^2=0$). The term including T_0, $\mathcal{M}_{\mu,0}$ gives also zero,

$$
\begin{aligned}
q^\mu \mathcal{M}_{\mu,0} &= ieq^\mu \bar{u}(p_1') \left[\gamma_\mu \frac{\not{p}_1' + m}{2p_1' \cdot q} T_0 - T_0 \frac{\not{p}_1 + m}{2p_1 \cdot q} \right] u(p_1) \\
&\quad + ieq^\mu \bar{u}(p_1') \left[\frac{2p_1' \cdot q}{2p_1' \cdot q} T_0 - T_0 \frac{2p_1 \cdot q}{2p_1 \cdot q} \right] u(p_1) = 0 \,, \qquad \text{(D.7)}
\end{aligned}
$$

where we used that $(\not{p} + m)\gamma_\mu u(p) = 2p_\mu u(p)$ and equivalently for $\bar{u}(p')$. The term with T_1 and T_2, which are derivatives in the off-shell direction gives

$$
\begin{aligned}
q^\mu \mathcal{M}_{\mu,12} &= ieq^\mu \bar{u}(p_1') \left[\gamma_\mu (\not{p}_1' + m) T_1 + T_2 (\not{p}_1 + m) \gamma_\mu \right] u(p_1) \\
&= 2ie1^\mu \bar{u}(p_1') \left[p_{1\mu}' T_1 + p_{1\mu} T_2 \right] u(p_1) \qquad \text{(D.8)}
\end{aligned}
$$

which is non-zero in general. The term $\mathcal{M}_{\mu,3}$ with the derivative in the on-shell direction, T_3, is given by

$$
\begin{aligned}
q^\mu \mathcal{M}_{\mu,3} &= ieq^\mu \bar{u}(p_1') \left[\gamma_\mu (\not{p}_1' + m) \frac{q \cdot p_2'}{2p_1' \cdot q} T_3 + T_3 \frac{q \cdot p_2}{2p_1 \cdot q} (\not{p}_1' + m) \gamma_\mu \right] u(p_1) \\
&= ie\bar{u}(p_1') \left[(q \cdot p_1') \frac{q \cdot p_2'}{p_1' \cdot q} T_3 + T_3 \frac{q \cdot p_2}{p_1 \cdot q} (q \cdot p_1) \right] u(p_1) \\
&= ieq^\mu \bar{u}(p_1') \left[p_{2\mu}' T_3 + T_3 p_{2\mu} \right] u(p_1) \,. \qquad \text{(D.9)}
\end{aligned}
$$

In order to conserve the current, $\mathcal{M}_\mu^{int}$ is expressed as

$$
\mathcal{M}_\mu^{int} = -ie\bar{u}(p_1') \left[2p_{1\mu}' T_1 + 2p_{1\mu} T_2 + p_{2\mu}' T_3 + T_3 p_{2\mu} \right] u(p_1) \,. \qquad \text{(D.10)}
$$

These terms can be interpreted as contribution from an internal radiation. The matrix element is expressed as

$$
\begin{aligned}
\mathcal{M}_\mu &= \mathcal{M}_\mu^{int} + \mathcal{M}_\mu^{ext} \\
&= ie\bar{u}(p_1') \left[\left(\gamma_\mu + \frac{i\kappa}{2m} \sigma_{\mu\nu} q^\nu \right) \frac{\not{p}_1' + m}{2p_1' \cdot q} T_0 - T_0 \frac{\not{p}_1 + m}{2p_1 \cdot q} \left(\gamma_\mu + \frac{i\kappa}{2m} \sigma_{\mu\nu} q^\nu \right) \right] u(p_1) \\
&\quad + ie\bar{u}(p_1') \left[\gamma_\mu \frac{\not{q}}{2p_1' \cdot q} T_0 - T_0 \frac{\not{q}}{2p_1 \cdot q} \gamma_\mu \right] u(p_1) \\
&\quad + ie\bar{u}(p_1') \left[\left(p_{1\mu}' \frac{q \cdot p_2'}{2p_1' \cdot q} - p_{2\mu}' \right) T_3 + T_3 \left(\frac{q \cdot p_2}{2p_1 \cdot q} p_{1\mu} - p_{2\mu} \right) \right] u(p_1) \\
&\quad + \mathcal{O}(q) \,. \qquad \text{(D.11)}
\end{aligned}
$$

In order to rewrite in terms of the particle 1 only, we introduce a following differential operator,

$$D_\mu(p_1) = \left(\frac{q\cdot p_2}{p_1\cdot q}p_{1\mu} - p_{2\mu}\right)\frac{\partial}{\partial\nu} = \frac{p_{1\mu}}{p_1\cdot q}q^\nu\frac{\partial}{\partial p_1^\nu} - \frac{\partial}{\partial p_1^\mu}\,. \tag{D.12}$$

With this operator the conserved current for the bremsstrahlung is written as

$$\begin{aligned}
\mathcal{M}_\mu &= ie\bar{u}(p_1')\left[\left(\gamma_\mu + \frac{i\kappa}{2m}\sigma_{\mu\nu}q^\nu\right)\frac{\not{p}_1'+m}{2p_1'\cdot q}T_0 - T_0\frac{\not{p}_1+m}{2p_1\cdot q}\left(\gamma_\mu + \frac{i\kappa}{2m}\sigma_{\mu\nu}q^\nu\right)\right]u(p_1) \\
&\quad + ie\bar{u}(p_1')\left[\gamma_\mu\frac{\not{q}}{2p_1'\cdot q}T_0 - T_0\frac{\not{q}}{2p_1\cdot q}\gamma_\mu\right]u(p_1) \\
&\quad + ie\bar{u}(p_1')\left[\overrightarrow{D_\mu}(p_1')T + T\overleftarrow{D_\mu}(p_1)\right]u(p_1) \\
&\quad + \mathcal{O}(q)\,.
\end{aligned} \tag{D.13}$$

The relation, $(\not{p}+m)\gamma_\mu u(p) = 2p_\mu u(p)$, is used for the first term and then,

$$\begin{aligned}
\mathcal{M}_\mu &= ie\bar{u}(p_1')\left[\frac{p_{1\mu}'}{p_1'\cdot q}T_0 - T_0\frac{p_{1\mu}}{p_1\cdot q}\right]u(p_1) \\
&\quad + ie\bar{u}(p_1')\left[\frac{i\kappa}{2m}\sigma_{\mu\nu}q^\nu\frac{\not{p}_1'+m}{2p_1'\cdot q}T_0 - T_0\frac{\not{p}_1+m}{2p_1\cdot q}\frac{i\kappa}{2m}\sigma_{\mu\nu}q^\nu\right]u(p_1) \\
&\quad + ie\bar{u}(p_1')\left[\gamma_\mu\frac{\not{q}}{2p_1'\cdot q}T_0 - T_0\frac{\not{q}}{2p_1\cdot q}\gamma_\mu\right]u(p_1) \\
&\quad + ie\bar{u}(p_1')\left[\overrightarrow{D_\mu}(p_1')T + T\overleftarrow{D_\mu}(p_1)\right]u(p_1) \\
&\quad + \mathcal{O}(q)\,.
\end{aligned} \tag{D.14}$$

The first term in Eq. (D.14) is $\mathcal{O}(1/q)$ and corresponds to the matrix element obtained with the classical theory in the soft photon limit, Eq. (C.6). This term includes the T-matrix at the on-shell point only. The other terms are $\mathcal{O}(q^0)$ and include only on-shell T-matrix. The interesting effects such as the off-shell effects in the T-matrix and non-nucleonic degrees of freedom appear in the higher-order terms.

From the above discussion, it is shown that it is needed to measure the radiation from the higher-order terms in order to investigate the off-shell effect and contribution from the non-nucleonic degrees of freedom such as the Δ current. As seen in

Appendix C, the $pp\gamma$ reaction has the advantage of smaller contribution from the $\mathcal{O}(1/q)$ term than the $pn\gamma$ case. The $pp\gamma$ process is more sensitive to the higher order term and has advantage to the investigations of the off-shell effect and the non-nucleonic degrees of freedom. The $pn\gamma$ reaction is considered to be the origin of the high energy photon emission from the nucleus-nucleus collision due to the large cross section. The effect of the higher order term increases as the photon energy increases due to the energy dependence of the matrix element. In order to investigate the higher order effect such as the off-shell effect and the Δ current contribution, measurements of the $pp\gamma$ reaction at relatively high photon energy are needed. In the present discussion, only the on-shell effect of the NN interaction is considered, and we have no information about the off-shell effect nor contribution from the Δ current.

In Eq. (D.14), contribution from only the particle 1 is considered. Contribution from the particle 2 is calculated in the same procedure as the particle 1 and the overall current is obtained by summing up the contribution from the two particles.

Appendix E

Potential model calculation

In this appendix, we explain the potential model calculation for the $pp\gamma$ reaction performed by de Jong *et al.* [20]. They include the processes of the NN and $N\Delta$ scattering, and single-scattering diagrams and re-scattering diagrams are considered in the calculations. They used the off-shell T-matrix element that are generated from a $NN \oplus N\Delta \oplus \pi NN$ coupled-channel model developed by Lee and Matsuyama [63, 64]. The T-matrices for the $NN \to N\Delta$ and $N\Delta \to NN$ are calculated with the transition potential $V_{NN\leftrightarrow N\Delta}$ taken from the one-pion-exchange model [65]. In the NN T-matrix, the effective NN potential, which includes the Paris potential and the Δ intermediate state calculated with the $V_{NN\leftrightarrow N\Delta}$, are used. This NN T-matrix can describe the NN phase shifts reasonably well up to about 1 GeV.

At the electromagnetic vertex, the matrix element for the $N \to N\gamma$ is expressed as

$$\langle p', k\lambda | V_{em} | p \rangle = e\bar{u}(p') \left(-i\not{\epsilon} + \frac{\mu - 1}{4m} (\not{k}\not{\epsilon} - \not{\epsilon}\not{k}) \right) u(p) \,, \tag{E.1}$$

where λ denotes a photon state with polarization ϵ_μ, m is a nucleon mass, e is a charge, and μ is the anomalous magnetic moment. The matrix elements of the $N \to \Delta\gamma$ and $\Delta \to \gamma N$ vertex interactions are , respectively

$$\langle p_\Delta, k\lambda | V_{em} | p \rangle = \bar{\psi}^\mu(p_\Delta) \Gamma_\mu^{\Delta N\gamma} u(p) \,, \tag{E.2}$$

and

$$\langle p, k\lambda | V_{em} | p_\Delta \rangle = \bar{u}(p) \Gamma_\mu^{N\Delta\gamma} \psi^\mu(p_\Delta) \,, \tag{E.3}$$

where $\psi(p_\Delta)$ is the Rarita-Schwinger spinor with normalization $\bar{\psi}^\mu(p)\psi_\mu(p) = -1$. The vertex function $\Gamma_\mu^{N\Delta\gamma}$ is written as

$$\Gamma_\mu^{N\Delta\gamma} = K_\mu^1 + K_\mu^2 \tag{E.4}$$

with

$$\begin{aligned} K_\mu^1 &= -ieG_1(\not{k}\epsilon_\mu - \not{\epsilon}k_\mu)\gamma_5 T_z\,, \\ K_\mu^2 &= -ieG_2(\epsilon_\mu P\cdot k - \epsilon.Pk_\mu)\gamma_5 T_z\,, \end{aligned} \tag{E.5}$$

where $k_\mu = p_\mu^{in} - p_\mu^{out}$ is the photon momentum and $P = \frac{1}{2}(p_\mu^\Delta + p_\mu^N)$. T_z is the third component of the isospin transition matrix for coupling an isospin 3/2 particle to an isospin 1/2 particle. For the $\Delta \to N\gamma$, we have

$$\Gamma_\mu^{\Delta N\gamma} = -K_\mu^1 + K_\mu^2\,. \tag{E.6}$$

The coupling constants, G_1 and G_2 are determined by the fitting to the $M1$ and $E1$ multipole data on the photoproduction of pions from nucleons. The values depend on the treatment of the nonresonant background contributions. The various sets of the coupling constants can be classified by the magnitude of G_1, since the vertex K_μ^1 gives the dominant contribution. In the present analysis, we take $G_1 = 2.68$ (GeV^{-1}) and $G_2 = -1.84$ (GeV^{-2}) for the highest coupling constant, and $G_1 = 2.0$ (GeV^{-1}), $G_2 = 0$ (GeV^{-2}) for the lowest coupling constant.

The $pp\gamma$ amplitude is expressed as

$$\langle pp\gamma|\mathcal{M}|pp\rangle = \langle pp\gamma|\mathcal{M}^{single}|pp\rangle + \langle pp\gamma|\mathcal{M}^{resc}|pp\rangle \tag{E.7}$$

where the single-scattering term is

$$\begin{aligned} \langle pp\gamma|\mathcal{M}^{single}|pp\rangle &= \sum_{\alpha=N,\Delta} \langle pp\gamma|V_{em}|\alpha\rangle G_\alpha(E)\langle\alpha|T_{N\alpha,NN}(E)|pp\rangle \\ &+ \sum_{\alpha=N,\Delta} \langle pp|T_{NN,N\alpha}(E-E_\gamma)|\alpha\rangle G_\alpha(E-E_\gamma)\langle\gamma\alpha|V_{em}|pp\rangle\,, \end{aligned} \tag{E.8}$$

where E_γ is the photon energy and G_α indicates the propagator of the N and Δ. The rescattering term is

$$\begin{aligned} &\langle pp\gamma|\mathcal{M}^{resc}|pp\rangle = \\ &\sum_{\alpha,\beta,\delta=N,\Delta} \langle pp|T_{NN,\delta\beta}(E-E_\gamma)|\alpha\beta\rangle G_{\alpha\beta}(E-E_\gamma)\langle\gamma\delta|V_{em}|\alpha\rangle G_{\alpha\beta}(E)\langle\delta\beta|T_{\alpha\beta,NN}(E)|pp\rangle\,. \end{aligned} \tag{E.9}$$

The amplitude including T-matrix is transformed to a covariant form [25]. The propagator G, however, includes the positive energy only, and no contributions from the negative energy states are considered in this calculation.

Bibliography

[1] M. Lacombe *et al.*, Phys. Rev. **C 21** 861 (1980).

[2] R. Machleidt, K. Holinde and Ch. Elster, Phys. Rep. **149** 1 (1987).

[3] F. Gross, J. W. Van Orden and K. Holinde, Phys. Rev. **C 41** R1909 (1990).

[4] V. G. J. Stokes, R. A. M. Klomp, C. P. F. Terheggen and J. J. de Swart, Phys. Rev. **C 49** 2950 (1994).

[5] B. Frois *et al.* Phys. Lett. **53B** 341 (1974).

[6] M. Suter, W. Wölfli, G. Bonani, Ch. Stoller and R. Müller, Phys. Lett. **58B** 36 (1975).

[7] J. V. Jovanovich, C. A. Smith, and L. G. Greeniaus Phys. Rev. Lett. **37** 631 (1976).

[8] J. Sanada, K. Kondo, and S. Seki Nucl. Phys. **A203** 388 (1973).

[9] L. S. Celenza, M. K. Liou, M. I. Sobel, and B. F. Gibson Phys. Rev. **C 8** 83 (1973).

[10] J. V. Jovanovich, in *Proceedings of the Second International Conference on Nucleon-nucleon Interactions (Vancouver, 1977),* edited by H. W. Fearing, D. F. Measday and A. Strathdee, AIP Conf. Proc. No. 41 (AIP, New York, 1978), p.451 and references therein.

[11] J. G. Rogers *et al.*, Phys. Rev. **C 22** 2512 (1980).

[12] K. Michaelian *et al.*, Phys. Rev. **D 41** 2689 (1990).

[13] B. V. Przewoski *et al.*, Phys. Rev. C **45** 2001 (1992).

[14] R. Bilger *et al.*, Phys. Lett. **B 429** 195 (1998).

[15] J. Zlomanczuk *et al.*, Nucl. Phys. **A 631** 622c (1998).

[16] M. Yuasa, Doctor thesis, Osaka University, 1998

[17] H. O. Meyer *et al.*, Nucl. Phys. **A 539** 633 (1992).

[18] N. Kalantar-Nayestanaki, Proceedings of XVth International Conference on Few-Body Problems in Physics, Groningen, The Netherlands, July 1997.

[19] J. A. Eden and M. F. Gari, Phys. Lett. **B 347** 187 (1995); Phys. Rev. C **53** 1102 (1996).

[20] F. de Jong, K. Nakayama V. Herrmann, and O. Scholten, Phys. Lett. **B 333** 1 (1994); F. de Jong, K. Nakayama and T.-S. Lee, Phys. Rev. C **51** 2334 (1995).

[21] F. de Jong and K. Nakayama, Phys. Lett. **B 385** 33 (1996).

[22] M. Jetter and H. W. Fearing, Phys. Rev. C **51** 1666 (1995).

[23] G. H. Martinus, O. Scholten and J. A. Tjon, Phys. Rev. C **56** 2945 (1997).

[24] G. H. Martinus, O. Scholten and J. A. Tjon, Phys. Rev. C **58** 686 (1998).

[25] V. Herrmann and K. Nakayama Phys. Rev. C **46** 2199 (1992).

[26] V. R. Brown,P. L. Anthony, and J. Franklin Phys. Rev. C **44** 1296 (1991).

[27] M. K. Liou and M. I. Sobel Anna. Phys. **72** 323 (1972).

[28] H. W. Fearing, Phys. Rev. Lett. **81**, 758 (1998).

[29] S. Kondratyuk, G. Martinus, and O. Scholten, Phys. Lett. **B 418** 20 (1998).

[30] D. L. Pursey, A. M. Shirokov, and T. A. Weber, nucl-th/9712021 (1997).

[31] K. Nakayama, private communication.

[32] B. M. K. Nefkens, O. R. Sander, D. I. Sober and H. W. Fearing, Phys. Rev. C **19** 877 (1979).

[33] V. Herrmann and K. Nakayama, Phys. Rev. **C 45** 1450 (1992).

[34] V. Herrmann, K. Nakayama, O. Scholten and H. Arellano, Nucl. Phys. **A 582** 568 (1995).

[35] M. Yosoi, private communication

[36] K. Sagara *et al.*, RCNP Annual Report 1995. p. 158

[37] http://www.natinst.com/labview

[38] M. Kato, Master thesis, Osaka University, 1998

[39] M. Nomachi *et al.*, RCNP Annual Report 1997. p 279

[40] M. Fujiwara *et al.*, Nucl. Instrum. Methods Phys. Res., **A 422** 484 (1999).

[41] T. Noro it et al., RCNP Annual Report

[42] N. Matsuoka *et al.*, RCNP Annual Report 1990, p. 235

[43] A. Tamii *et al.*, IEEE Trans. on Nucl. Sci. **43**, 2488 (1996) ; RCNP Annual Report 1997, p. 277

[44] M. Nomachi *et al.*, Nucl. Phys. **A 629** 213c (1998).

[45] S. Stanislaus *et al.*, Phys. Rev. **C 41** R1913 (1990).

[46] J. G. Hardie *et al.*, Phys. Rev. **C 56** 20 (1997).

[47] R. A. Arndt, I. I. Strakovsky and R. L. Workman Phys. Rev. **C 50** 2731 (1994); http://said.phys.vt.edu

[48] T. Taki, private communication.

[49] D. Drechsel and L. C. Maximon Ann. Phys. **49** 403 (1968).

[50] H. F. Jones and M. D. Scadron, Ann. Phys. **81**, 1 (1973).

[51] B. ter Harr and R. Malfliet, Phys. Rep. **149**, 207 (1987).

[52] G. H. Martinus, Doctor thesis, Rijksuniversiteit Grooningen, 1998.

[53] O. Scholten, private communication.

[54] J. Fleischer and J. Tjon, Nucl. Phys. **A 84**, 375 (1974); Phys. Rev. **D 15**, 2537 (1977); **D 21**, 87 (1980).

[55] O. Scholten, in Proceedings of Taps Workshop III, Bosen, 1995.

[56] J. D. Jackson, "Classical Electrodynamics", (New York, 1975).

[57] F. E. Low, Phys. Rev. **110**, 974 (1958).

[58] E. M. Nyman, Phys. Rev. **170**, 1628 (1969).

[59] S. L. Adler and Y. Dothan Phys. Rev. **151**, 1267 (1966).

[60] H. W. Fearing, Phys. Rev. **C 6**, 1136 (1972).

[61] H. W. Fearing, in *Proceedings of the Second International Conference on Nucleon-nucleon Interactions (Vancouver, 1977),* edited by H. W. Fearing, D. F. Measday and A. Strathdee, AIP Conf. Proc. No. 41 (AIP, New York, 1978), p.506

[62] I. J. R. Aitchison and A. J. G. Hey, "Gauge theories in particle physics", (Bristol, 1989)

[63] T. -S. H. Lee Phys. Rev. Lett **50** 1571 (1983); Phys. Rev. **C 29** 195 (1984).

[64] T. -S. H. Lee and A. Matsuyama Phys. Rev. **C 36** 1459 (1987).

[65] G. -H. Niephaus, M. Gari, and B. Sommer Phys. Rev. **C 20** 1096 (1979).